

RADIO INTERFERENCE MODELING AND PREDICTION FOR SATELLITE OPERATION APPLICATIONS

Tien M. Nguyen, et al.

**Department of Electrical Engineering and Computer Science
The Catholic University of America
Washington, DC 20064**

25 Aug 2015

Final Report

APPROVED FOR PUBLIC RELEASE; DISTRIBUTION IS UNLIMITED.



**AIR FORCE RESEARCH LABORATORY
Space Vehicles Directorate
3550 Aberdeen Ave SE
AIR FORCE MATERIEL COMMAND
KIRTLAND AIR FORCE BASE, NM 87117-5776**

DTIC COPY NOTICE AND SIGNATURE PAGE

Using Government drawings, specifications, or other data included in this document for any purpose other than Government procurement does not in any way obligate the U.S. Government. The fact that the Government formulated or supplied the drawings, specifications, or other data does not license the holder or any other person or corporation; or convey any rights or permission to manufacture, use, or sell any patented invention that may relate to them.

This report is the result of contracted fundamental research deemed exempt from public affairs security and policy review in accordance with SAF/AQR memorandum dated 10 Dec 08 and AFRL/CA policy clarification memorandum dated 16 Jan 09. This report is available to the general public, including foreign nationals. Copies may be obtained from the Defense Technical Information Center (DTIC) (<http://www.dtic.mil>).

AFRL-RV-PS-TR-2015-0116 HAS BEEN REVIEWED AND IS APPROVED FOR
PUBLICATION IN ACCORDANCE WITH ASSIGNED DISTRIBUTION STATEMENT.

//SIGNED//
STEVEN A. LANE
Program Manager

//SIGNED//
PAUL HAUSGEN, Ph.D.
Technical Advisor, Space Based Advanced Sensing
and Protection

//SIGNED//
JOHN BEAUCHEMIN
Chief Engineer, Spacecraft Technology Division
Space Vehicles Directorate

This report is published in the interest of scientific and technical information exchange, and its publication does not constitute the Government's approval or disapproval of its ideas or findings.

REPORT DOCUMENTATION PAGE				Form Approved OMB No. 0704-0188	
Public reporting burden for this collection of information is estimated to average 1 hour per response, including the time for reviewing instructions, searching existing data sources, gathering and maintaining the data needed, and completing and reviewing this collection of information. Send comments regarding this burden estimate or any other aspect of this collection of information, including suggestions for reducing this burden to Department of Defense, Washington Headquarters Services, Directorate for Information Operations and Reports (0704-0188), 1215 Jefferson Davis Highway, Suite 1204, Arlington, VA 22202-4302. Respondents should be aware that notwithstanding any other provision of law, no person shall be subject to any penalty for failing to comply with a collection of information if it does not display a currently valid OMB control number. PLEASE DO NOT RETURN YOUR FORM TO THE ABOVE ADDRESS.					
1. REPORT DATE (DD-MM-YYYY) 25-08-2015		2. REPORT TYPE Final Report		3. DATES COVERED (From - To) 23 Sep 2014 to 24 Aug 2015	
4. TITLE AND SUBTITLE Radio Interference Modeling and Prediction for Satellite Operation Applications				5a. CONTRACT NUMBER FA9453-14-1-0259	
				5b. GRANT NUMBER	
				5c. PROGRAM ELEMENT NUMBER 62601F	
6. AUTHOR(S) Tien M. Nguyen, Hien Tran, Zhonghai Wang, Amanda Coons, ZiJian Mo, Genshe Chen, Charles C. Nguyen, Gang Wang				5d. PROJECT NUMBER 8809	
				5e. TASK NUMBER PPM00019115	
				5f. WORK UNIT NUMBER EF122748	
7. PERFORMING ORGANIZATION NAME(S) AND ADDRESS(ES) Department of Electrical Engineering and Computer Science The Catholic University of America Washington, DC 20064				8. PERFORMING ORGANIZATION REPORT NUMBER	
9. SPONSORING / MONITORING AGENCY NAME(S) AND ADDRESS(ES) Air Force Research Laboratory Space Vehicles Directorate 3550 Aberdeen Ave SE Kirtland AFB, NM 87117-5776				10. SPONSOR/MONITOR'S ACRONYM(S) AFRL/RVSV	
				11. SPONSOR/MONITOR'S REPORT NUMBER(S) AFRL-RV-PS-TR-2015-0116	
12. DISTRIBUTION / AVAILABILITY STATEMENT Approved for public release; distribution is unlimited.					
13. SUPPLEMENTARY NOTES					
14. ABSTRACT This report describes an innovative radio frequency interference evaluation and prediction framework. This report presents associated modeling and prediction tools to: (1) detect the presence of radio frequency interference using receiver's synchronizer, (2) estimate the radio frequency interference characteristics, (3) evaluate effectiveness of the existing unified S-band command waveforms employed by civil, commercial and military satellite operations ground stations, and (4) predict the impacts of radio frequency interference on unified S-band command systems. The proposed framework and radio frequency interference prediction tools allow a communication designer to estimate the optimum transmitted signal power to maintain a required satellite operations quality-of-service in the presence of both friendly and unfriendly radio frequency interference sources.					
15. SUBJECT TERMS space communication; satellite communication, satellite operations, radio frequency interference					
16. SECURITY CLASSIFICATION OF:			17. LIMITATION OF ABSTRACT	18. NUMBER OF PAGES	19a. NAME OF RESPONSIBLE PERSON
a. REPORT	b. ABSTRACT	c. THIS PAGE			19b. TELEPHONE NUMBER (include area code)
Unclassified	Unclassified	Unclassified	Unlimited	138	Steven A. Lane

(This page intentionally left blank)

TABLE OF CONTENTS

LIST OF FIGURES	iii
LIST OF TABLES	vi
1 SUMMARY	1
2 INTRODUCTION	1
2.1 Description of Problems for RFI Detection and Prediction	3
2.2 Impacts of RFI on Synchronization Loops Performance	6
2.3 Scope of Effort	8
2.4 Organization of Report	9
3 METHODS, ASSUMPTIONS, AND PROCEDURES	10
3.1 Assessment of Existing RFI Tools and RFI Tool Selection	10
3.2 Framework for RFI Tool Development and RFI Assessment	12
3.2.1 Framework for RFI Detection and Prediction Tool Development	12
3.2.2 Framework for RFI Detection and Prediction	13
3.2.3 Framework for RFI Assessment	15
3.3 RFI Analytical and Simulation Model Development	16
3.3.1 Analytical Models for Unified S-band Waveforms	16
3.3.2 Analytical Models for RFI Signals	23
3.3.3 Simulation Models for the Second-Order Phase Locked Loop	24
3.3.4 Existing Carrier Acquisition Approaches	29
3.3.5 Analytical Models for Assessing PLL Acquisition Performance in the Presence of RFI	37
3.3.6 Analytical Models for Assessing PLL Lock Detector	42
3.3.7 Analytical Models for Assessing PLL Tracking Performance	45
3.3.8 RFI Detection Models	50
3.3.9 USB Signal Estimation Models	53
3.3.10 RFI Signal Estimation and Prediction Models	66
3.3.11 USB Link Budget Models for Assessing SATOPS Performance	95
4 RESULTS AND DISCUSSION	100
4.1 RFI Detection and Prediction Model Integration	100
4.2 IFT SATCOM Tool Integration	101
4.3 Verification and Validation of RFI Detection and Prediction Tools	106
5 CONCLUSIONS	114

6	RECOMMENDATIONS.....	116
	REFERENCES	118
	LIST OF SYMBOLS, ABBREVIATIONS, AND ACRONYMS	119

LIST OF FIGURES

Figure 1. A Typical Satellite Control Network.....	2
Figure 2. Typical Friendly RFI Scenarios.....	4
Figure 3. Definition of Interference Bandwidth and Corresponding CCI and ACI Scenarios	5
Figure 4. Notional Subcarrier Tracking Jitter Performance of PCM/PSM/PM without RFI	7
Figure 5. Notional Subcarrier Tracking Jitter Performance of PCM/PSM/PM with RFI	7
Figure 6. RFI Detection-Prediction Tool Development Framework	13
Figure 7. RFI Detection-Prediction Models Development Framework.....	14
Figure 8. BER Performance Model for Predicting the Impacts of RFI on SATOPS Performance	15
Figure 9. RFI Assessment Framework.....	16
Figure 10. PCM/PSK/PM Modulator-Transmitter Model	17
Figure 11. PCM/Bi-Phase Modulator-Transmitter Model.....	17
Figure 12. NRZ Data Format for PCM/PSK/PM-Sinewave Subcarrier	19
Figure 13. Power Spectral Density for PCM/PSK/PM-Sinewave Subcarrier Waveform	19
Figure 14. Receiver-Demodulator for PCM/PSK/PM-Sinewave Subcarrier Waveform	20
Figure 15. Bi-Phase Data Format Used By PCM/PM-Bi-Phase Waveform	21
Figure 16. Power Spectral Density of PCM/PM/Bi-Phase Waveform	21
Figure 17. Receiver-Demodulator for PCM/PM/Bi-Phase Waveform.....	22
Figure 18. Advanced Second-Order PLL Employed by NASA Spacecraft and Satellites.....	26
Figure 19. Recursive Implementation of $F(z)$, $B(z)$, $K(z)$ and $V(z)$ Using Bilinear Transformation	26
Figure 20. Typical Second-Order PLL Employed by Civil and Commercial Satellites.....	29
Figure 21. Carrier Acquisition Approaches for USB SATOPS Systems	30
Figure 22. Carrier Frequency Acquisition Using Frequency Sweep Technique	32
Figure 23. Minimum Sweep Rate and Probability of Lock as a Function of Receive Power	33
Figure 24. Phase Acquisition Process of a PLL.....	35
Figure 25. Typical Maximum Likelihood (ML) Phase Estimator	36
Figure 26. Typical PLL Lock Detector Employed By Civil, Commercial and Military SATOPS Satellites.....	43

Figure 27. Proposed Framework and Algorithm for RFI Detection	53
Figure 28. Linearized Model of Advanced NASA PLL Shown in Figure 18 for Tracking Mode	56
Figure 29. Mathematical Framework and Algorithm to Incorporate PLL Tracking Error into USB Signal Estimation Model.....	56
Figure 30. Simulation Model for Incorporating Carrier Tracking Error into NASA Advanced Second-Order PLL	57
Figure 31. Simulation Model for Incorporating Carrier Tracking Error into Typical Type-I Imperfect Integrator Second-Order PLL.....	60
Figure 32. Tracking Phase Error as a Function of Time.....	64
Figure 33. Difference of Tracking Error as a function of Time.....	64
Figure 34. Phase Plane Plot for a Typical PLL Using Type-I Imperfect Integrator for $ISR = -15$ dB.....	65
Figure 35. Phase Plane Plot for a Typical PLL Using Type-I Imperfect Integrator for $ISR = 25$ dB.....	65
Figure 36. Block Diagram of the USB Carrier Signal Component Estimator.....	66
Figure 37. Block Diagram for Extracting the CW RFI Signal from the Received Signal, $R(t)$...	68
Figure 38. Block Diagram for CW RFI Estimation, Prediction and Detection Model.....	69
Figure 39. Block Diagram for CW RFI Signal Power Estimation	70
Figure 40. Block Diagram for CW RFI Frequency Estimation	75
Figure 41. Block Diagram for CW RFI Phase Estimation and RFI Detection	77
Figure 42. Receiver Operating Curve for the CW RFI Signal Detector Shown in Figure 41	78
Figure 43. Block Diagram for Extracting the WB RFI Signal from the Received Signal, $R_{WB}(t)$	79
Figure 44. Block Diagram for the WB RFI Estimation, Prediction and Detection Model.....	81
Figure 45. Block Diagram for the WB RFI Power Estimation.....	82
Figure 46. Block Diagram for the WB RFI Signal Frequency Estimator.....	85
Figure 47. Block Diagram for WB RFI Phase Estimation and RFI Detection	88
Figure 48. Block Diagram for WB RFI Data Stream and Rata Rate Estimation.....	90
Figure 49. Block Diagram for WB RFI Synchronizer.....	92
Figure 50. Block Diagram for WB RFI PSD and Data.....	93
Figure 51. RFI Modeling and Prediction Tool Integration	102

Figure 52. IFT SatComm Tool Integrated With RFI Prediction Results	103
Figure 53. BER Performance With CW RFI or WB RFI and Imperfect Carrier Tracking Loop	104
Figure 54. Tracking Error Results Under No RFI and CW RFI or WB RFI Scenario	104
Figure 55. Acquisition Time Result Under CW RFI	105
Figure 56. Acquisition Time Result Under WB RFI	106
Figure 57. Plots of Total Carrier Acquisition Times Versus Loop SNR Without RFI and With CW RFI	107
Figure 58. Plots of Total Carrier Acquisition Times as Functions of Loop SNR Without RFI and With WB RFI at ISR = -10 dB	108
Figure 59. Plots of Total Carrier Acquisition Times as Functions of Loop SNR Without RFI and With CW RFI	109
Figure 60. Plots of Total Carrier Acquisition Times as Functions of Loop SNR Without RFI and With WB RFI at ISR = -40 dB	110
Figure 61. Plots of PLL Tracking Jitter in the Absence of RFI and Presence of CW and WB RFI Signals as Functions of Loop SNR With $\Delta f_{\text{RFI}} = 5$ Hz	111
Figure 62. Plots of PLL Tracking Jitter in the Absence of RFI and Presence of CW and WB RFI Signals as Functions of Loop SNR With $\Delta f_{\text{RFI}} = 10$ Hz	112
Figure 63. Plots of BER due to RFI for Both CW RFI and WB RFI Signals as Functions of Loop SNR With $f_{\text{RFI}} = 5$ Hz	113
Figure 64. Plots of BER due to RFI for Both CW RFI and WB RFI Signals as Functions of Loop SNR With $f_{\text{RFI}} = 10$ Hz	113

LIST OF TABLES

Table 1. Other Aerospace RFI Tools	12
Table 2. Typical Parameters for USB Waveform Acquisition and Tracking Modes	22
Table 3. Carrier Modulation Mode (CMM) for SATOPS USB Acquisition.....	29
Table 4. Typical Type-I Imperfect Integrator Employed By NASA PLL.....	63
Table 5. Rain Attenuation Loss in dB Calculated for 2GHz and 3 GHz	98
Table 6. Signal Losses Due to Scintillation for 15° and 10° Elevation Angle at 2.06 GHz.....	98
Table 7. Signal Losses Due to Scintillation for 15° and 10° Elevation Angle at 1.8 GHz.....	98

ACKNOWLEDGMENTS

This material is based on research sponsored by Air Force Research Laboratory under agreement number FA9453-14-1-0259. The U.S. Government is authorized to reproduce and distribute reprints for Governmental purposes notwithstanding any copyright notation thereon.

DISCLAIMER

The views and conclusions contained herein are those of the authors and should not be interpreted as necessarily representing the official policies or endorsements, either expressed or implied, of Air Force Research Laboratory or the U.S. Government.

(This page intentionally left blank)

Approved for public release; distribution is unlimited.

1 SUMMARY

This report describes innovative radio frequency interference (RFI) evaluation and prediction frameworks that incorporate effects of RFI on the satellite receiver synchronizers. This report also presents associated RFI modeling and prediction tools to: (i) detect the presence of RFI using the receiver's synchronizer, (ii) estimate RFI characteristics, (iii) evaluate effectiveness of the existing unified S-band (USB) command waveforms employed by civil, commercial and military satellite operations ground stations, and (iv) predict the impacts of RFI on USB command systems. The approach presented here would allow a communications designer to characterize both friendly and unfriendly RFI sources, and evaluate the impacts of RFI on civil, commercial, and military USB satellite operations systems. In addition, the proposed frameworks and RFI prediction models would allow a designer to estimate the optimum transmitted signal power required to maintain a USB satellite operational quality-of-service (QoS) in the presence of both friendly and unfriendly RFI sources.

2 INTRODUCTION

SATOPS, which is defined as a satellite operation service provided by a satellite control network (SCN), includes tracking, telemetry, and command (TT&C) services. Figure 1 illustrates a typical civil, commercial, and military satellite control network. It contains the following components:

- Ground Tracking Station (GTS): Usually located at a remote place with a clear view of sky;
- Satellite Control Center (SCC): Provides support for the operation, control, and maintenance of satellites - SCC executes TT&C operations;
- Network Control Center (NCC): Provides support for the scheduling, satellite network configuration, and operation of SCC, GTS, and satellites; and
- Ground Communications Network (GCN): Supports data transfers among SCC, GTS, and the NCC.

SATOPS is usually operating in L-band (1 – 2 GHz) or S-band (2 – 4 GHz) frequencies, where there are many potential sources of radio frequency interference (RFI) to TT&C data links. We have conducted a survey of RFI analysis tools and found that there are many RFI analysis tools

available to analyze the impacts of RFI on SATOPS systems. However, most of RFI tools do not consider the time-factor (TF) when calculating bit or carrier signal-to-noise ratio (SNR) degradation due to interference. Some RFI tools incorporate the TF by incorporating the SATOPS schedules along with interference protection criteria (IPC¹) to identify the blockage due to RFI. These tools assume that RFI increases a receiver's noise floor. None of these tools consider the effects of RFI on the receiver's synchronization loops.

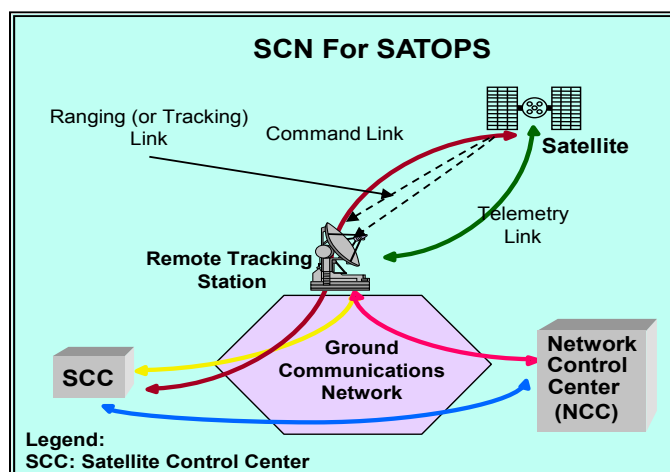


Figure 1. A Typical Satellite Control Network

This report describes an approach that will incorporate: (i) the receiver synchronization loops, including carrier and subcarrier tracking, and symbol timing loops, and thereby evaluating the interfering TF at the synchronization loop-level, (ii) statistical technique to estimate the type of interference and predict its impact on the synchronization loops, and (iii) statistical techniques to optimize the SNR of the transmitted TT&C signal to overcome the synchronization errors caused by RFI sources. The focus is on the SATOPS using USB waveforms².

Potential radio frequency (RF) sources that can cause interference to existing civil, commercial, or military USB SATOPS systems can be classified into two categories:

¹ IPC is Interference Protection Criteria recommended by National Telecommunication and Information Administration (NTIA) and International Telecommunication Union (ITU).

² USB waveforms are used by civil and commercial SATOPS systems operating in Unified S-Band frequencies. Recently, U.S. Air Force has been making progress to migrate its SATOPS operations to USB.

- Category I - friendly RFI sources: The sources are from friendly, unintentional interference from satellite data links from neighboring orbiting satellites. This category also includes friendly SATOPS tracking stations within the field-of-view (FOV) of the victim's SATCOM links. Friendly RFI sources can cause co-channel interference (CCI) or adjacent channel interference (ACI), depending on the transmitting carrier frequencies. Potential friendly RFI sources that are common for civil and commercial personal communication systems include 3G wireless, 4G wireless, WiFi and WIMAX.
- Category II - unfriendly RFI sources: These are caused by intentional jammers, including:
 - Classical jammer: A high power jamming signal transmitted with the intention to shut down the entire USB SATOPS system operation or to significantly reduce the efficiency of USB SATOPS data link throughput; and,
 - Smart jammer: Purposed to monitor the USB SATOPS data links and inject weak jamming signals in the channel with the intention to degrade the USB SATOPS quality-of-service (QoS).

2.1 Description of Problems for RFI Detection and Prediction

Figure 2 illustrates typical friendly RFI scenarios for uplink and downlink, respectively. The figure shows that potential RFI occurs when the victim receiver (on-board a satellite in the case of an uplink or at the ground station in the case of a downlink) simultaneously collect power from a desired signal source and other undesired interferers. Existing RFI analysis tools evaluate the extent to which the victim receiver collects sufficient power from one or more interfering links to degrade the performance below an acceptable interference protection criteria (IPC) level, at which blockage occurs. The problems addressed in our work deal with the detection and prediction of the RFI signals coming from both friendly and unfriendly sources.

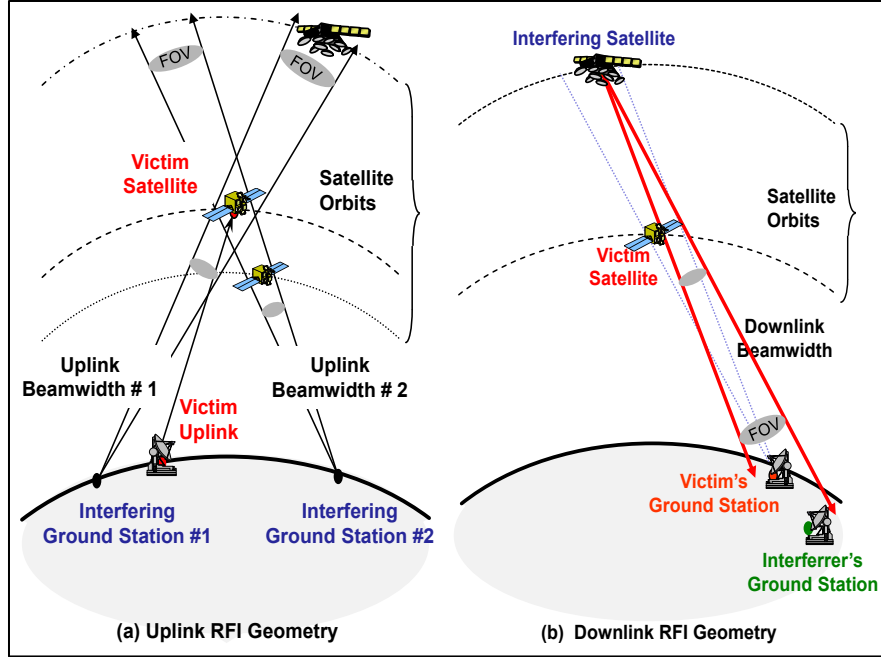


Figure 2. Typical Friendly RFI Scenarios

Our research developed a new RFI detection algorithm that would monitor the SATOPS receiver's synchronizer performance. The RFI detection algorithm assumes that the interfering link must be operating and satisfy the following considerations:

- i. Geometry Consideration: Victim receiver must be within the beamwidth (or field-of-view) of an interferer's transmitting antenna and, at the same time, the interferer must be within the beamwidth of the victim receiver's antenna.
- ii. Frequency Consideration: Any interfering link must have part or its entire signal power spectrum within the victim receiver's "interference bandwidth" (see Figure 3). Therefore, the frequency separation between the victim and interfering receivers, and the spectral spreading of the interfering signal, determines the contribution to the interference power. Likewise, the victim receiver's "interference bandwidth" is determined based on the power spectral density (PSD) of the victim signal. The spectral spreading of the interfering signal depends on its PSD, which in turn depends on its waveform, i.e., data rate, coding and modulation scheme.

- iii. Interfering Power Consideration: From the total interference power point-of-view, the RFI effects from all the interfering links (friendly or unfriendly) must exceed the IPC to declare that a potential RFI event is to occur. The IPC is usually derived from the victim's receiver operating threshold or obtained from national or international regulatory bodies, such as NTIA (National Telecommunications and Information Administration), FCC (Federal Communications Commission) or ITU (International Telecommunication Union). Figure 3 describes the interference bandwidth and the corresponding CCI and ACI scenarios.
- iv. Interfering Time Consideration: The effects from all the interfering links must be sufficient from the time duration (i.e., time-factor (TF)) point-of-view to cause an unacceptable degradation in victim receiver performance in order to declare an RFI event has been detected. The TF will also be incorporated into the receiver's synchronization loop to ensure that the detected event is truly caused by an RFI source.

The RFI detection tool development and analysis framework described in this report will incorporate the above four considerations for the interference links.

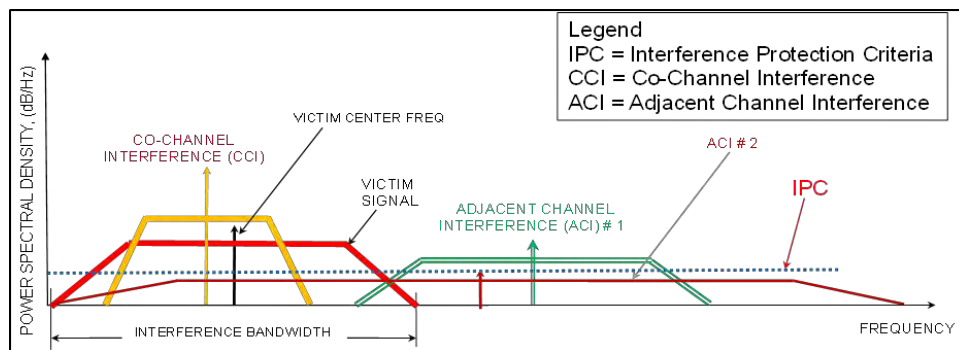


Figure 3. Definition of Interference Bandwidth and Corresponding CCI and ACI Scenarios

To predict RFI occurrence, the RFI analysis framework must also incorporate the four considerations for the interference links. The total power coming from the interfering links must exceed the IPC and stay within victim's carrier tracking loop and symbol synchronizer loop bandwidth long enough to force the synchronization loops out-of-lock. If the loops can re-acquire and track the desired signal quickly, the operator may not declare an RFI occurrence.

The interfering TF consideration is a complex issue. It deals with the carrier tracking loop and the symbol synchronizer performance (also referred to as timing synchronization loop, timing synchronizer, or timing recovery loop). In addition to the four considerations for the detection problem, the following considerations must be incorporated in the RFI framework for the prediction problem:

- Carrier Tracking Performance Consideration: The interference signals have to exceed the carrier threshold power level and stay within the carrier tracking loop bandwidth for a certain time duration before the carrier loop drops lock and the carrier loop is unable to re-acquire the carrier within a specified time window.
 - Sub-Carrier Tracking Performance Consideration: The interference signals have to exceed the subcarrier threshold power level and stay within the subcarrier tracking loop bandwidth for a certain time duration before the subcarrier loop drops lock and the subcarrier loop is unable to re-acquire the subcarrier within a specified time window.
 - Symbol Timing Synchronization Performance Consideration: The interference signals have to exceed the threshold symbol signal-to-noise ratio (SNR) level and stay within the symbol synchronizer's loop bandwidth for a certain time duration before the symbol synchronizer drops lock and is not able to re-acquire the timing within a specified time window.
1. Hop / De-Hop / Spread / De-Spread Consideration: For a victim receiver using a waveform employing spread-spectrum or frequency-hopping techniques, the interfering signals must stay within the spreading or hopping bandwidth long enough to cause the de-spread or de-hop synchronizer to drop lock.

2.2 Impacts of RFI on Synchronization Loops Performance

This section elaborates on the synchronization loop performance considerations described previously. Figure 4 and Figure 5 show a notional second-order Costas loop subcarrier tracking the jitter performance of a unified S-band (USB) waveform, namely PCM / PSK / PM (Pulse Code Modulation / Phase Shift Keying / Phase Modulation), in the absence of and presence of RFI. Figure 4 shows that, in the absence of RFI, the subcarrier tracking jitter does not have a break-point. It reaches a steady-state value around 1.2 degrees. On the other hand, Figure 5

shows that the tracking jitter grows as RFI power increases. At a specific interference power that exceeds the subcarrier power threshold level that corresponds to a threshold subcarrier tracking jitter, e.g., 15 degrees, the tracking jitter grows logarithmically. When this happens, the subcarrier tracking loop declares that an RFI event has occurred and the loop would be switched from tracking mode to acquisition mode. The RFI framework must be developed to incorporate this event.

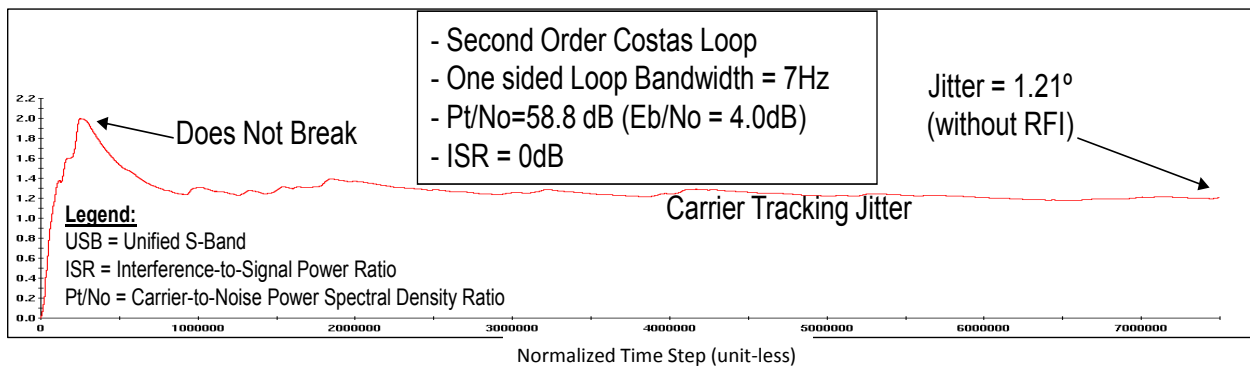


Figure 4. Notional Subcarrier Tracking Jitter Performance of PCM/PSM/PM without RFI

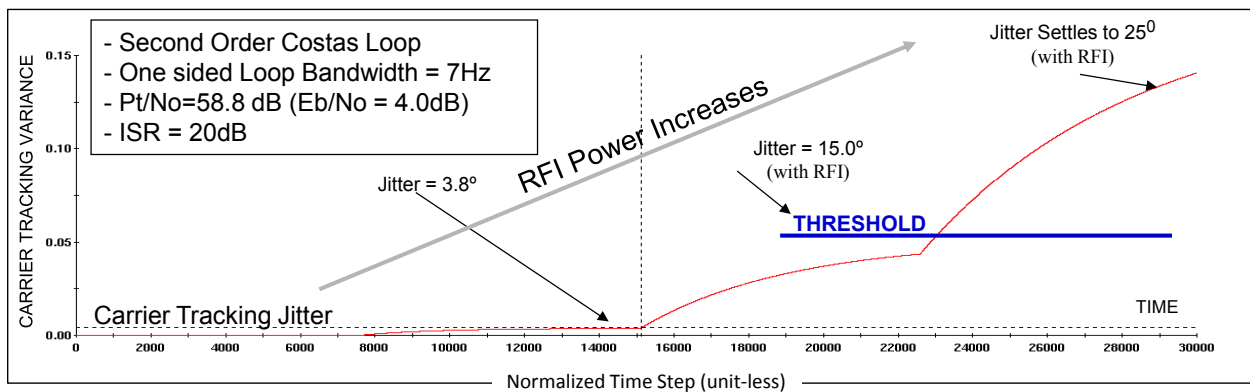


Figure 5. Notional Subcarrier Tracking Jitter Performance of PCM/PSM/PM with RFI

2.3 Scope of Effort

The objective for this research effort was three-fold:

1. Investigate radio frequency interference and the effects that it has on wireless communication systems, both private and commercial, both terrestrial and for satellite communications;
2. Develop RFI tools that can detect sources of interference, predict the effects of multiple sources at different frequencies, and allow evaluation of the impact to operational systems; and
3. As a first-order exercise of the tools, consider satellite operation (SATOPS) systems employed by civil and commercial unified S-band waveforms.

Our work focused on USB waveforms employed by private and commercial service providers to support military and commercial SATOPS applications. To achieve this objective, the following tasks were performed and completed during the period-of-performance for this effort:

- i. Task #1: The Catholic University of America (CUA) conducted an assessment of existing RFI tools related to SATCOM and SATOPS and then selected an RFI tool that could accurately address geometry considerations, frequency considerations, and power considerations. North Carolina State University (NCSU), CUA's subcontractor, provided support for this task.
- ii. Task #2: CUA developed a framework for RFI tool development applicable to both satellite communications and satellite operations.
- iii. Task #3: CUA developed analytical and simulation models to accurately address interfering time duration for satellite operation applications. The focus of this task was on the civil and commercial SATOPS USB waveforms.
- iv. Task #4: CUA integrated the analytical and simulation models developed in Task 3 with the RFI tool selected in Task 1. A beta version of the RFI tool for USB waveforms was completed.
- v. Task #5: CUA integrated the model developed in Task 4 into existing Intelligent Fusion Technology (IFT, a sub-contractor) SATCOM tools to display the RFI prediction and detection results. IFT provided integration and Matlab simulation support for this task.

- vi. Task #6: CUA investigated verification and validation approaches for the RFI detection and prediction tools, and provided recommendations for experimentally validating the modeling and assessment tools.

2.4 Organization of Report

This report is organized as follow:

- Section 3.1 provides a summary of the results found in Task #1. Key results from the survey of existing RFI analysis tools are presented.
- Section 3.2 describes the framework for the RFI tools developed in Task #2. This section presents the proposed innovative framework for developing analytical and simulation tools to: (a) predict the characteristics of RFI sources, and (b) evaluate impacts of RFI to USB SATOPS systems. The framework is applicable to both satellite communications and satellite operations.
- Section 3.3 presents the analytical and simulation models developed in Task #3. These models can accurately predict the interfering time duration for the SATOPS applications. As mentioned earlier, the focus of this section is on the civil and commercial SATOPS USB waveforms.
- Section 4.1 discusses the integration results obtained in Task #4. This section describes how the analytical and simulation models presented in Section 3.3 were integrated with the RFI tool selected in Section 3.1.
- Section 4.2 describes the integration results obtained in Task #5. This section discusses how the model was ported into existing IFT (Intelligent Fusion Technology, Inc) SATCOM tools to display the RFI detection and prediction results.
- Section 4.3 presents the investigation results found in Task #6. This section presents the numerical results obtained from the analytical and simulation models presented in Section 3.3, and discusses the verification and validation approaches of these models for the RFI detection and prediction tools presented in Section 4.1.
- Section 5 and Section 6 summarize the work and discusses future studies. In addition, this section also provides recommendations for experimentally validating the modeling and assessment tools.

3 METHODS, ASSUMPTIONS, AND PROCEDURES

3.1 Assessment of Existing RFI Tools and RFI Tool Selection

A thorough survey was conducted of existing RFI analysis tools available in the public domain. As listed below, many RFI analysis software tools are available to analyze the impacts of RFI on digital communication systems. As pointed out earlier, most of these RFI analysis tools do not consider the time-factor (TF) when calculating the bit or carrier signal to noise degradation due to interference. These tools assume that the RFI power simply increases the receiver's noise floor and adds to the amount of interference power collected by a victim's receiver. However, some RFI analysis tools did consider the TF by incorporating the SATCOM and SATOPS schedules along with the Interference Protection Criteria (IPC) (recommended by NTIA and/or ITU) to identify the blockage (i.e., outage) due to RFI, but these tools also assumed that the RFI power causes an increase in the receiver noise floor. ***None of these tools considered the effects of the RFI on the synchronization loops, including de-spreading loop, de-hop loop, carrier tracking, and timing loop, and incorporating the TF at the synchronization loop-level.*** Below is a list of the existing RFI tools and their associated capabilities.

- JPL Enhanced Spectral Analysis Tool for RFI Analysis and Spectrum Management: Provides predictors of signal / interference / filters / spikes, power spectrum plots, calculations for spectral power, telecommunication link budget tables and interference analysis tables, configuration menu for the analysis table that contains options on antenna, amplifier, and receiver for ground terminal characterization.
- NTIA Spectrum / Orbit Utilization Program for Interference Analysis of Geostationary Communication Satellites: This tool calculates interference and computes the communication impacts of that interference, including: (i) the feeder link carrier-to-interference ratio (C/I) is calculated at each satellite, and (ii) at each earth station the downlink C/I is calculated, taking into account interference from all other satellites in the geostationary orbit.
- AGI's Systems Tool Kit (STK) for RFI Analysis: STK models satellite dynamics and RF propagation, communication link budget, avoidance, interference and jamming in dynamic "real-world" scenarios.

- JPL Interference Analysis Program: The tool is used to select the radio frequencies that would be used for uplink and downlink communications with the objective of avoiding or minimizing the possibility of RFI between existing and planned missions.
- Lincom LinCsim (acquired by Titan on January 31, 2000; Titan was later acquired by L-3 Communications on June 3, 2005): Analytical simulation package provides modeling of RFI effects on bit error rate performance including detailed models for the space shuttle and Tracking and Data Relay Satellite System (TDRSS) links.
- The Aerospace Corporation Web-based Tool for Analyzing Effects of RFI on Satellite Communication Systems: The tool can calculate the: (i) interfering frequency factor (the fraction of the wave that is within the victim's beamwidth) on a victim satellite, (ii) interfering satellite attributes including altitude, inclination, earth center inertial longitude and orbit phase for multiple constellations with multiple satellites, and (iii) mean and variance of RFI durations and outputs the times at which RFI occurs and which satellite and ground stations are involved.
- The Aerospace Corporation RFI Tool for Analyzing IMT-2000 Interference With DOD Satellites: The tool uses Satellite Orbit Analysis Program (SOAP) to generate temporal latitude/ longitude profiles for orbiting satellites and calculate interference power density using: (i) different contributions from base stations in rural areas and cities, (ii) ITU propagation path loss and base station antenna model, (iii) NTIA traffic models for IMT-2000 (derived from ITU models), (iv) parameterized percentage of IMT-2000 land coverage, region classification, and traffic environment mixes for cities and rural areas, (v) communications link calculation models for CDMA-2000 and W-CDMA, and (vi) actual geometry to be considered in computing base station effective isotropic radiated power (EIRP), space loss, and atmospheric loss.

In addition to the RFI analysis tools described above, we are also aware of other RFI tools that were developed by the Aerospace Corporation in the mid-2000's for both commercial and military applications. Table 1 summarizes these RFI tools. The RFI approaches used by these tools were similar to the above tools and did not include the time-factor using synchronization loops. This effort leveraged the Aerospace Corporation Web-based Tool described above for incorporating the RFI detection and prediction framework and models to assess the impacts of

RFI on SATOPS USB systems. The newly developed RFI analysis tool incorporates the effects of the carrier synchronizer loop in assessing the impacts of RFI on SATOPS USB systems.

Table 1. Other Aerospace RFI Tools

SW Tool	Analysis Performed	Task/Program
SPW (Signal Processing Workstation)	GMSK/QPSK with pulsed RFI	ICO/Teledesic
	ACI for combinations of QPSK, 8PSK and 16QAM	Gapfiller
	GMSK with a variety of jammers	AEHF
	QPSK with single-tone jammer	GBS
	Baseband filtering of SGLS to reduce out-of-band emissions, and SGLS interference to PCS	AFSCN
FORTTRAN and C Programs	Uplink interference in USB	SGLS Migration to USB Study

3.2 Framework for RFI Tool Development and RFI Assessment

This section describes the framework for: (i) RFI tool development, (ii) RFI detection and prediction, and (iii) RFI assessment, respectively.

3.2.1 Framework for RFI Detection and Prediction Tool Development

Figure 6 illustrates a framework for the development of required analytical and simulation tools for detecting and predicting RFI sources. The framework is color-coded to show the models and tools developed under this effort and the status of the tool development. Each block in Figure 6 represents a model, which can be an analytical model or a simulation model, required for the detection and prediction of RFI sources. The analytical and simulation models were developed and integrated according to the proposed framework, and implemented in Matlab to provide an RFI detection and prediction tool for assessing the impacts of RFI on SATOPS systems. The blocks labeled “Completed” means that a model was developed and implemented in Matlab. The lighter blue boxes indicate models of interest for this phase of the study. The darker blue boxes indicate that the models would be developed when time permitted, and the darkest blue boxes indicate the models are to be developed in the next phase of this

effort. As illustrated in Figure 6, the focus of this study was on two USB command waveforms, namely, PCM/PSK/PM (pulse code modulation, phase shift keying, phase modulation) and PCM/PM/Bi-Phase (pulse code modulation, phase modulation, bi-phase) [1,2]. Section 3.3 describes the models labeled “Completed”.

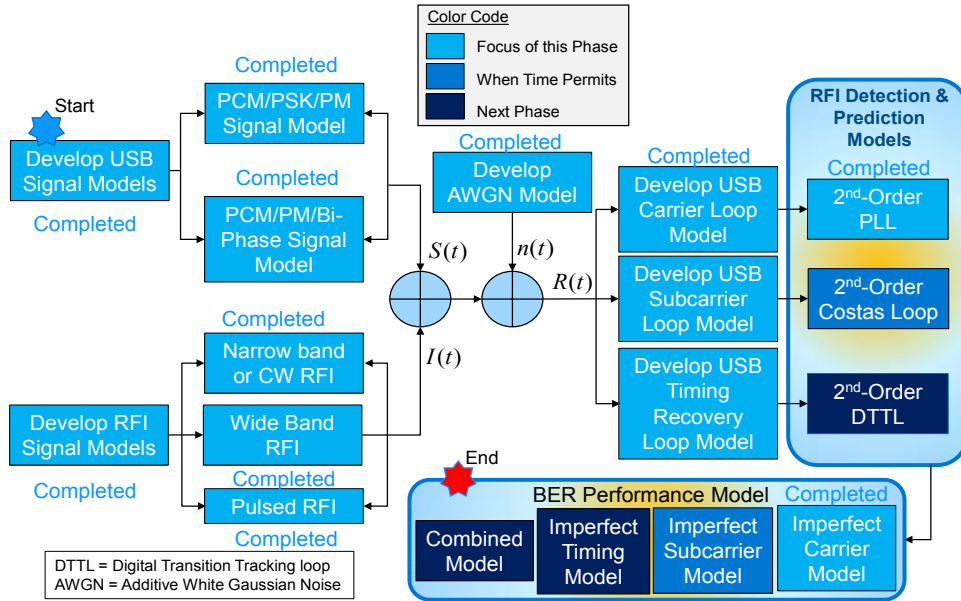


Figure 6. RFI Detection-Prediction Tool Development Framework

3.2.2 Framework for RFI Detection and Prediction

As mentioned, the focus of this effort was modeling of RFI detection and estimation for the carrier synchronization loop. Figure 7 illustrates a framework for the development of RFI detection and prediction models. The framework describes the analytical and simulation models required for the detection and prediction of the RFI sources using existing USB carrier tracking loops. As indicated in this figure, the carrier synchronizer loop is a second-order phase locked loop (PLL). The framework also describes an algorithm to integrate these analytical and simulation models for detecting and characterizing RFI sources that can be used for mitigating the interference effects on the bit error rate (BER) performance of the USB SATOPS systems.

Section 3.3 provides a detailed description of the required analytical and simulation models labeled as “Completed”.

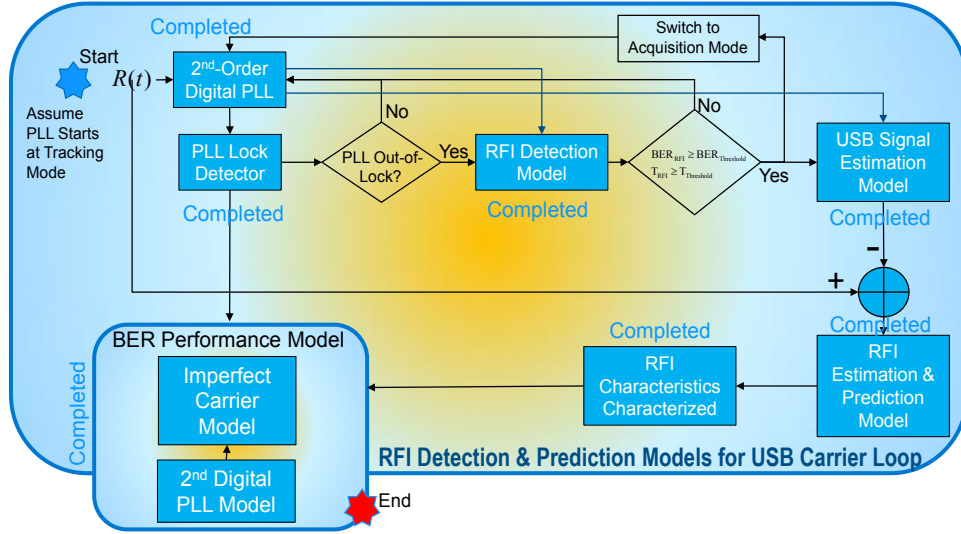


Figure 7. RFI Detection-Prediction Models Development Framework

The block entitled “BER Performance Model”, shown in Figure 7, is used to predict the BER performance degradation due to the presence of RFI and is further expanded and illustrated in Figure 8. This model was used for predicting the bit SNR performance degradation due to RFI for the specified quality-of-service (QoS) in terms of the BER. The predicted SNR degradation included the effects of the imperfect carrier tracking due to additive white Gaussian noise (AWGN) and RFI, and the receiver noise floor raised by the RFI power.

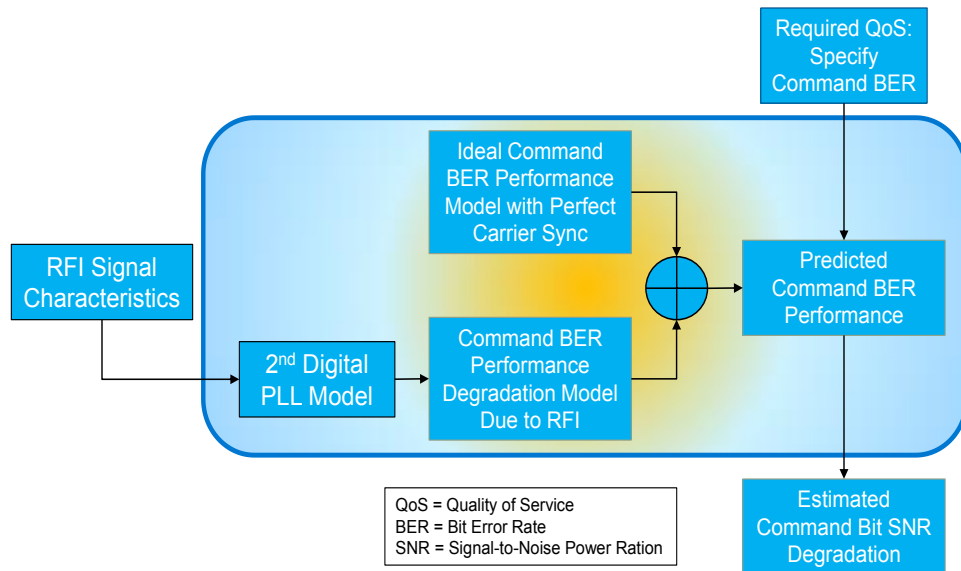


Figure 8. BER Performance Model for Predicting the Impacts of RFI on SATOPS Performance

3.2.3 Framework for RFI Assessment

Finally, a framework for assessing RFI impacts on overall performance of the SATOPS USB system is presented in Figure 9. Using the bit SNR degradation found from the “BER Performance Model”, this framework describes a process to overcome the effects of RFI by increasing the transmitted SATOPS signal power.

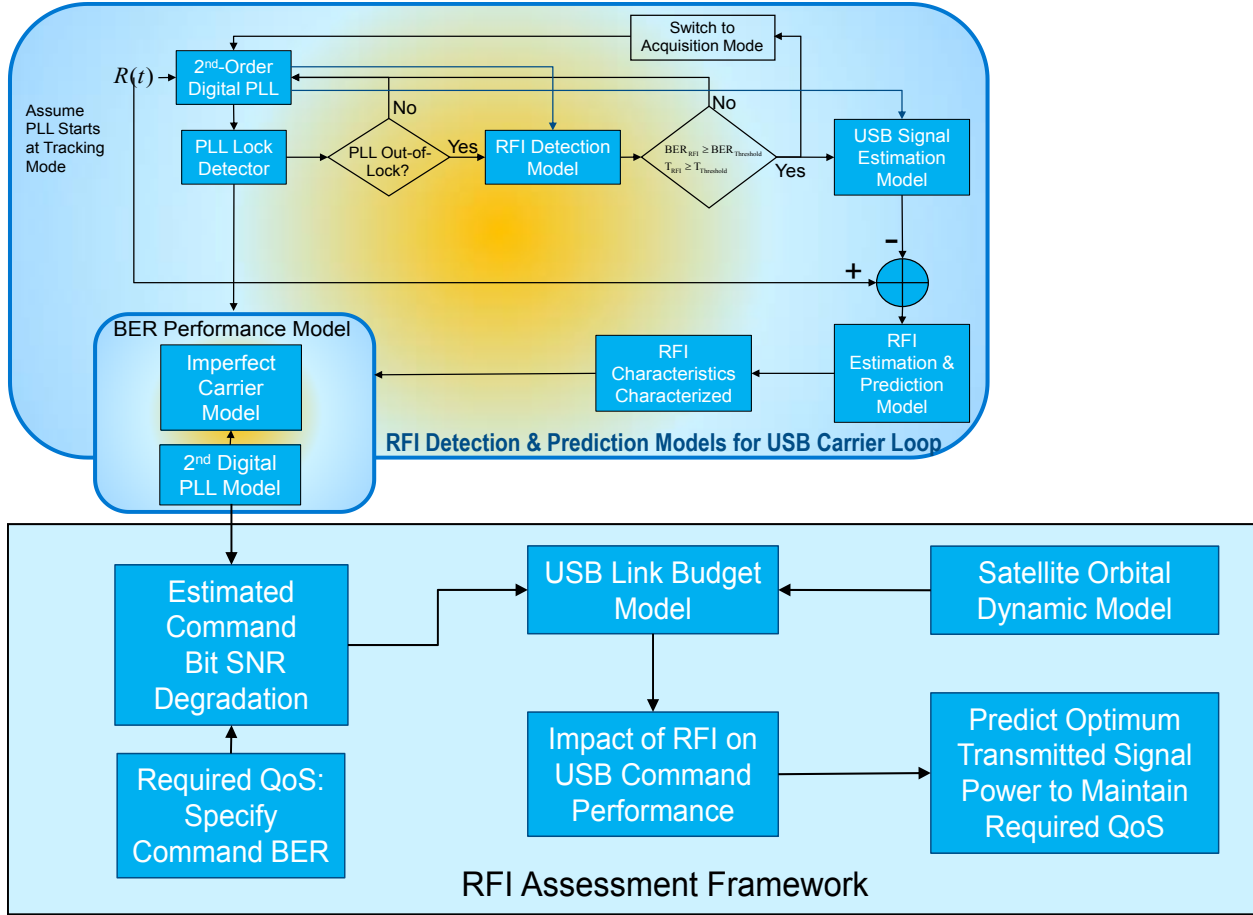


Figure 9. RFI Assessment Framework

3.3 RFI Analytical and Simulation Model Development

This section provides a detailed description of the required analytical/simulation models shown in Figure 6, Figure 7, Figure 8 and Figure 9.

3.3.1 Analytical Models for Unified S-band Waveforms

As described earlier, the PCM/PSK/PM and PCM/PM/Bi-Phase waveforms were the focus of this study. Simplified modulator and transmitter models for these two waveforms are presented in Figure 10 and Figure 11, respectively. For PCM/PSK/PM-Sinewave Subcarrier waveform, the NRZ (Non-Return-to-Zero) command data is PSK modulated on the subcarrier, with subcarrier frequency, f_{sc} , set at 8 kHz when the command bit rate is less than 2 kbps, and at

16 kHz when the bit rate is between 2 kbps and 4 kbps. The modulated command subcarrier is then phase-modulated on the carrier frequency, f_c . The uplink command (or tele-command) S-band carrier frequency is selected between 2025 MHz and 2125 MHz. The PCM/PM/Bi-Phase waveform is used when the command data rate is greater than 4 kbps. For this waveform, the NRZ command data is converted to bi-phase data format and then phase modulated on the command S-band carrier frequency. The modulation index, m , for these two waveforms is selected to ensure proper power is allocated to the carrier signal component and command signal component to achieve predefined carrier and command margins [3]. Margin is defined as the difference between the required signal power and received signal power. A detailed description of this waveform is given below.

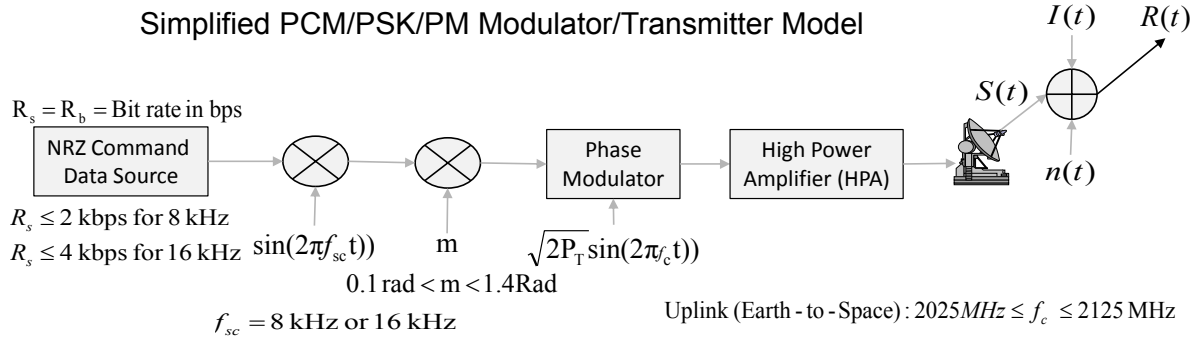


Figure 10. PCM/PSK/PM Modulator-Transmitter Model

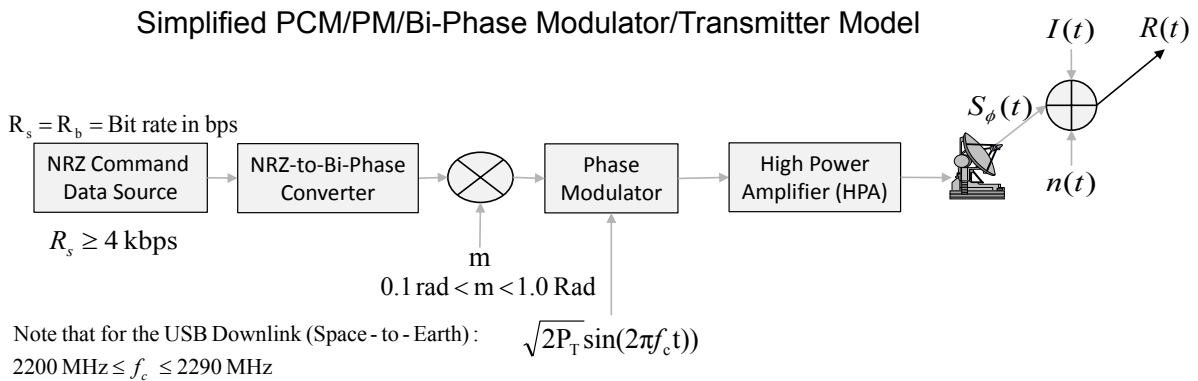


Figure 11. PCM/Bi-Phase Modulator-Transmitter Model

Analytical and simulation models and tools are required to detect and predict the RFI signal characteristics in the presence of these two USB waveforms, and to assess the impacts of RFI on these two waveforms. Using the USB command modulator/transmitter models presented in Figure 10 and Figure 11, a high-level framework for the RFI detection-prediction tools development is described in Figure 6. Figure 6 describes the required USB signal, noise and interference models to detect and predict the RFI signals in the presence of the two USB signals. As indicated earlier, Figure 6 is color-coded to show that the “USB Carrier Loop Model” and “Imperfect Carrier Model” are the focus for this phase of the research.

3.3.1.1 *PCM/PSK/PM Sine Wave Subcarrier Waveform*

The mathematical expression for the PCM/PSK/PM-sine-wave subcarrier is defined by:

$$S(t) = \sqrt{2P_T} \cos(2\pi f_c t + m d(t) \sin(2\pi f_{sc} t)) \quad (1)$$

where

P_T = total transmitted power,

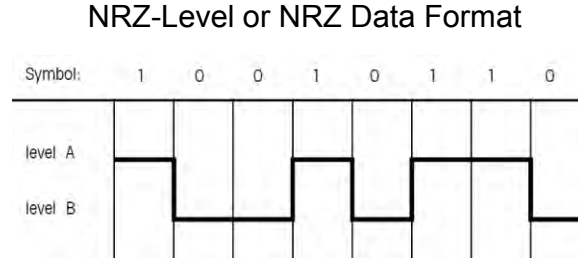
f_c = transmitted carrier frequency (Hz),

m = command modulation index in radians,

$d(t)$ = NRZ command data with symbol rate R_s , and

f_{sc} = command subcarrier frequency (Hz).

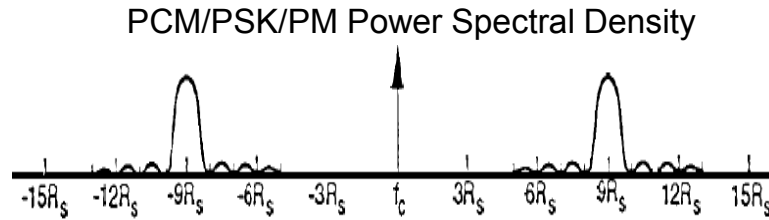
Figure 12 illustrates the NRZ data format used by the PCM/PSK/PM-sine-wave subcarrier waveform. As shown in this figure, the data format is a non-return-to-zero (NRZ) format. Figure 13 shows the power spectral density (PSD) of the PCM/PSK/PM-sine-wave subcarrier waveform. The subcarrier is used to separate the carrier component and the data component. When the subcarrier frequency to bit rate ratio, n , is larger (i.e., $n > 4$), the interference from the data component to the carrier tracking loop can be neglected.



$$R_s = R_b = \text{Bit rate in bps}$$

$$T_s = T_b = \text{Bit duration in second}$$

Figure 12. NRZ Data Format for PCM/PSK/PM-Sinewave Subcarrier



$$f_{sc} = 9R_s$$

Figure 13. Power Spectral Density for PCM/PSK/PM-Sinewave Subcarrier Waveform

The receiver-demodulator for the PCM/PSK/PM-sine-wave subcarrier waveform is shown in Figure 14. This figure is also color-coded to show that the focus of this study is on the carrier synchronizer loop. This report focused on the acquisition and tracking performance of the carrier PLL in the presence of RFI sources.

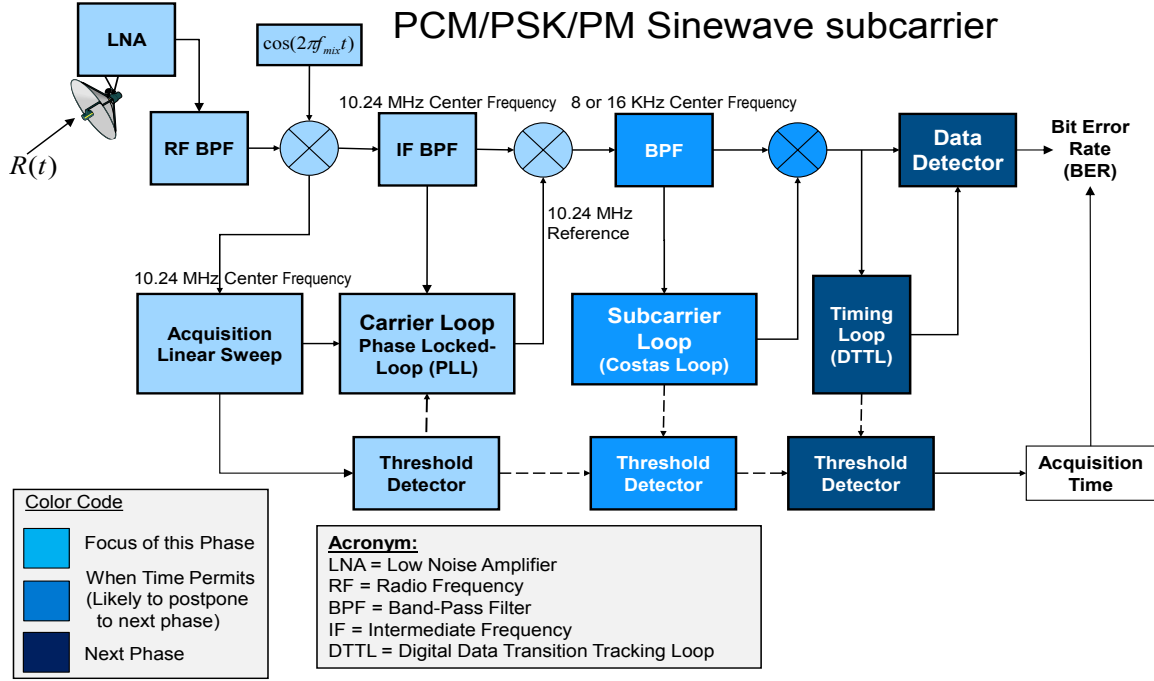


Figure 14. Receiver-Demodulator for PCM/PSK/PM-Sinewave Subcarrier Waveform

3.3.1.2 PCM/PM/Bi-phase Waveform

Figure 15 illustrates the bi-phase data format used by the PCM/PM/Bi-Phase waveform. The mathematical expression for the PCM/PM/Bi-Phase is defined by [1]:

$$S_{\phi}(t) = \sqrt{2P_T} \cos(2\pi f_c t + m d_{\phi}(t)) \quad (2)$$

where $d_{\phi}(t)$ is the bi-phase command data with symbol rate, R_s , or bit rate, R_b . Figure 16 shows the PSD of the PCM/PM-Bi-Phase waveform. The spectral null created by using the bi-phase data format allows the communication designer to insert the carrier component into the waveform. When the command data rate is greater than or equal to 4 kbps, the spectral null becomes “flat” and causes negligible degradation to the carrier PLL performance. The receiver-demodulator for the PCM/PM-Bi-Phase waveform is shown in Figure 17. Similarly, this figure is color-coded to illustrate that the focus of this study is on the carrier synchronizer loop. Table 2 shows acquisition and tracking typical parameters used by the SATOPS USB receiver-

demodulator for acquisition and tracking of the carrier, subcarrier, and timing of the received waveforms.

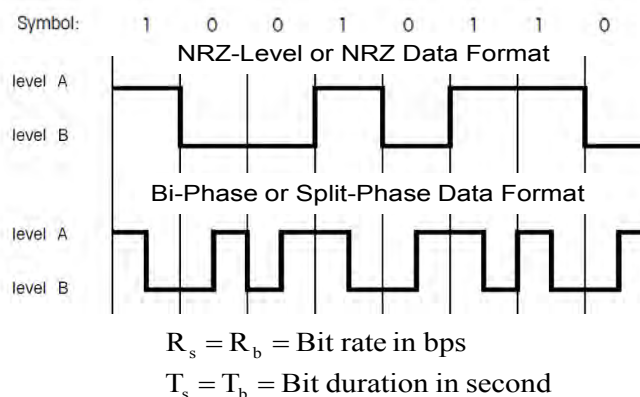


Figure 15. Bi-Phase Data Format Used By PCM/PM-Bi-Phase Waveform

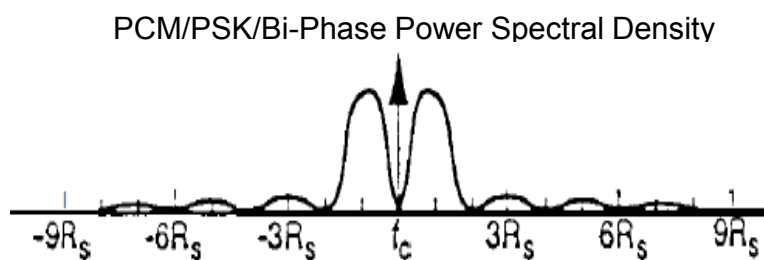


Figure 16. Power Spectral Density of PCM/PM/Bi-Phase Waveform

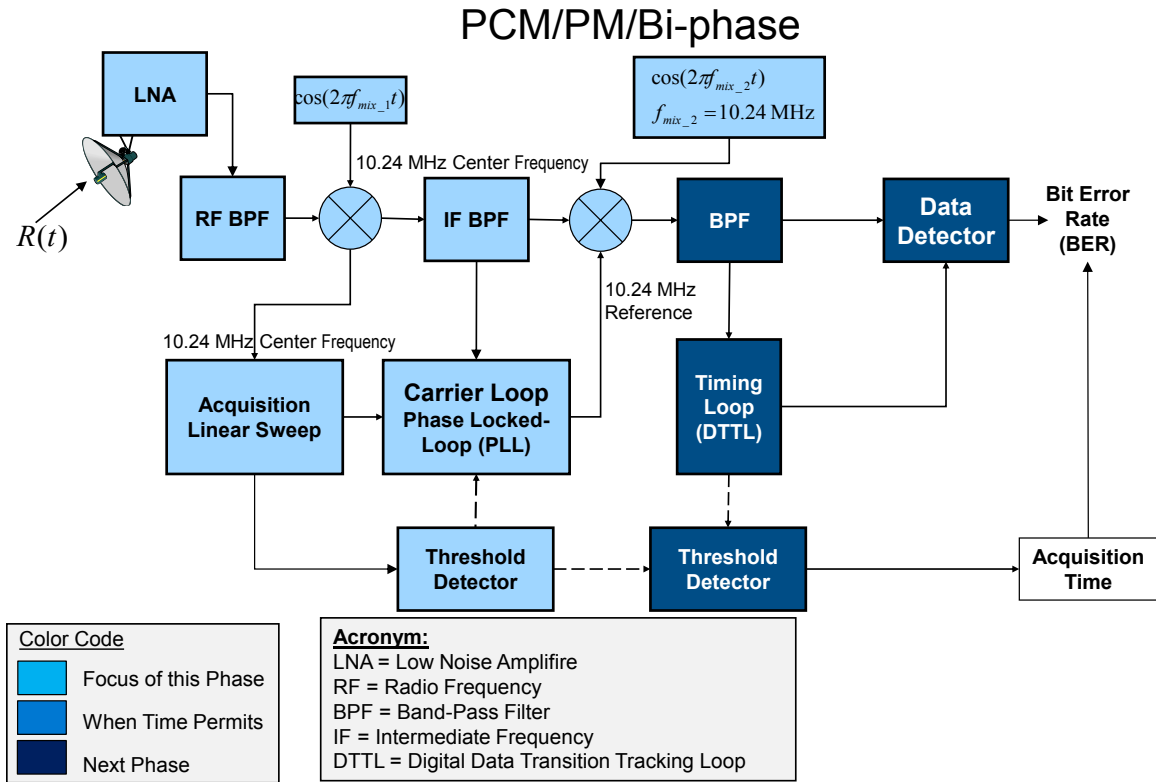


Figure 17. Receiver-Demodulator for PCM/PM/Bi-Phase Waveform

Table 2. Typical Parameters for USB Waveform Acquisition and Tracking Modes

Tracking Mode	Acquisition Mode
<ul style="list-style-type: none"> Carrier Recovery Loop (PLL) <ul style="list-style-type: none"> Loop Bandwidth (B_L): 10 - 400 Hz $B_L T_b \leq 0.1$ SubCarrier Recovery Loop (Costas) <ul style="list-style-type: none"> Loop Bandwidth: 100 - 400 Hz Damping factor: $1/\sqrt{2}$ $B_L T_b \leq 0.1$ Timing Recovery Loop (DTTL) <ul style="list-style-type: none"> Loop Bandwidth: 10 - 20 Hz Damping factor: $1/\sqrt{2}$ $B_L T_b \leq 0.1$ 	<ul style="list-style-type: none"> Carrier <ul style="list-style-type: none"> Acquisition Loop Bandwidth: <ul style="list-style-type: none"> $B_{LAcq} \geq \text{Doppler Frequency}$ Linear Sweep of ± 55 kHz <ul style="list-style-type: none"> 12.18 seconds (duration) Lock Detector Integration time ~ 300 symbols Sub-Carrier <ul style="list-style-type: none"> Lock Detector Integration time ~ 256 symbols Timing <ul style="list-style-type: none"> Lock Detector Integration time ~ 400 symbols

3.3.2 Analytical Models for RFI Signals

The received signal at the SATOPS USB receiver-demodulator can be characterized by:

$$R(t) = S(t) + I(t) + n(t), \quad (3)$$

where $n(t)$ is the average white Gaussian noise with one-sided power spectral density, N_0 . $S(t)$ is the received USB signal of interest. For PCM/PSK/PM-sine-wave subcarrier, it is given by:

$$\begin{aligned} S(t) &= a\sqrt{2P_T} \cos(2\pi(f_c + f_d)t + md(t) \sin(2\pi f_{sc}t) + \theta_c) \\ \tilde{S}(t) &= a\sqrt{2P_T} [\exp(j(2\pi(f_c + f_d)t + \theta_c)) \exp(j(md(t) \sin(2\pi f_{sc}t)))] \\ S(t) &= \text{Real}\left\{\tilde{S}(t)\right\} \end{aligned}, \quad (4)$$

where

f_d = Doppler shift due to satellite movement,

θ_c = received carrier phase shift of the desired signal, and

a = channel gain factor.

$I(t)$ is the RFI signal received at the SATOPS USB receiver-demodulator, and it is defined as:

$$\begin{aligned} I(t) &= \sqrt{2P_I} d_I(t) \cos(2\pi(f_c + \Delta f_c)t + \theta_I) \\ d_I(t) &= \sum_{n=-\infty}^{\infty} I_n \cdot p(t - nT_I - \tau), \end{aligned} \quad (5)$$

where

P_I = RFI power,

Δf_c = RFI frequency offset from the desired carrier frequency, f_c , and

θ_I = RFI phase.

Here, I_n and $p(t)$ characterize the type of RFI. The RFI signal can be rewritten in the following form:

$$I(t) = \sqrt{2P_I} d_I(t) \text{Re}[\exp(j2\pi(f_c + \Delta f_c)t + \theta_I)], \quad (6)$$

with I_n the RFI data sequence, $p(t)$ the RFI unit amplitude rectangular pulse of duration, T_I , and τ the time asynchronization of the RFI with respect to the desired signal, $s(t)$. RFI signals can be classified into: (1) narrowband RFI or continuous wave (CW) RFI, (2) wideband RFI, and (3) pulsed RFI. For narrowband RFI, $I_n = 1$ and $T_I = 0$. For wideband RFI, I_n is an independent and identically distributed sequence taking on equiprobable values of ± 1 , with

$$T_I \geq T_b = \frac{1}{R_b}, \quad (7)$$

which is the bit duration of the desired signal in seconds. For pulsed RFI, $I_n = 1$ during T_I and $I_n = 0$ during $T_{PRF} - T_I$, where T_I is the RFI pulse duration in seconds, and PRF is the pulse repetition frequency.

3.3.3 Simulation Models for the Second-Order Phase Locked Loop

A typical analog PLL model used by advanced NASA spacecraft and satellite is shown in Figure 18. This PLL has advanced features to cut-out the loop noise and smoothing the tracking phase error for improved carrier tracking performance. These two features are characterized by the low-pass filter $B(s)$ and phase smoother $V(s)$ shown in Figure 18, in addition to existing loop filter $F(s)$ and VCO filter $K(s)$. Figure 18 also describes the characteristics of the filters. Figure 19 describes the digital modeling of the advanced second-order PLL shown in Figure 18 [4]. The figure shows detailed description of the filter coefficients. The digital closed-loop transfer function of the digital filters shown in Figure 19 is defined as [4]:

$$H(Z) = \frac{AK [B(Z)F(Z)V(Z)K(Z)]}{1 + AK [B(Z)F(Z)V(Z)K(Z)]} \quad (8)$$

The one-sided loop noise bandwidth is given by:

$$B_{DL} = \frac{1}{4\pi j T_S H^2(1)} \oint_{|Z|=1} H(Z)H(Z^{-1}) \frac{dZ}{Z} \quad (9)$$

Substituting (8) into (9), one obtains:

$$B_{DL} = \left[\frac{1}{2T_S H^2(1)} \right] \left[\frac{a_0 b_0 Q_0 - a_0 B_1 Q_1 + a_0 B_2 Q_2 - a_0 B_3 Q_3 + B_4 Q_4}{a_0 \{ (a_0^2 - a_4^2) Q_0 - (a_0 a_1 - a_3 a_4) Q_1 + (a_0 a_2 - a_2 a_4) Q_2 - (a_0 a_3 - a_1 a_4) Q_3 \}} \right]$$

where

$$B_0 = b_0^2 + b_1^2 + b_2^2 + b_3^2 + b_4^2; \quad B_1 = 2(b_0 b_1 + b_1 b_2 + b_2 b_3 + b_3 b_4)$$

$$B_2 = 2(b_0 b_2 + b_1 b_3 + b_2 b_4); \quad B_3 = 2(b_0 b_3 + b_1 b_4); \quad B_4 = 2b_0 b_4$$

$$Q_0 = a_0 e_1 e_4 - a_0 a_3 e_2 + a_4(a_1 e_2 - e_3 e_4); \quad Q_1 = a_0 a_1 e_4 - a_0 a_2 a_3 + a_4(a_1 a_2 - a_3 e_4)$$

$$Q_2 = a_0 a_1 e_2 - a_0 a_2 e_1 + a_4(a_2 e_3 - a_3 e_2); \quad Q_3 = a_1(a_1 e_2 - e_3 e_4) - a_2(a_1 e_1 - a_3 e_3) + a_3(e_1 e_4 - a_3 e_2)$$

$$Q_4 = a_0 [e_2(a_1 a_4 - a_0 a_3) + e_5(a_0^2 - a_4^2)] + (e_2^2 - e_5^2)[a_1(a_1 - a_3) + (a_0 - a_4)(e_4 - a_2)]$$

$$e_1 = a_0 + a_2; \quad e_2 = a_1 + a_3; \quad e_3 = a_2 + a_4$$

$$e_4 = a_0 + a_4; \quad e_5 = a_0 + a_2 + a_4$$

(10)

with

$$a_0 = 2F_S A_{10} A_{11} + AK A_0; \quad a_1 = 2F_S (A_{10} A_{00} A_1 + A_{01} A_{11} A_1 - A_{10} A_{11} B_1 - A_{11} A_{10} A_1) + AK(3A_0 - B_0)$$

$$a_2 = 2F_S A_1 (A_{00} A_{01} - A_{01} A_{11}) + 2F_S B_1 (A_{10} A_{11} - A_{10} A_{00} - A_{01} A_{11}) + 3AK(A_0 - B_0)$$

$$a_3 = 2F_S B_1 (A_{00} A_{10} - A_{01} A_{00} + A_{01} A_{11}) - 2F_S A_1 A_{01} A_{00} + AK(A_0 - 3B_0); \quad a_4 = 2F_S B_1 A_{10} A_{00} - AK B_0$$

$$b_0 = AK A_0; \quad b_1 = AK(3A_0 - B_0); \quad b_2 = 3AK(A_0 - 3B_0)$$

$$b_3 = AK(A_0 - 3B_0); \quad b_4 = -AK B_0$$

(11)

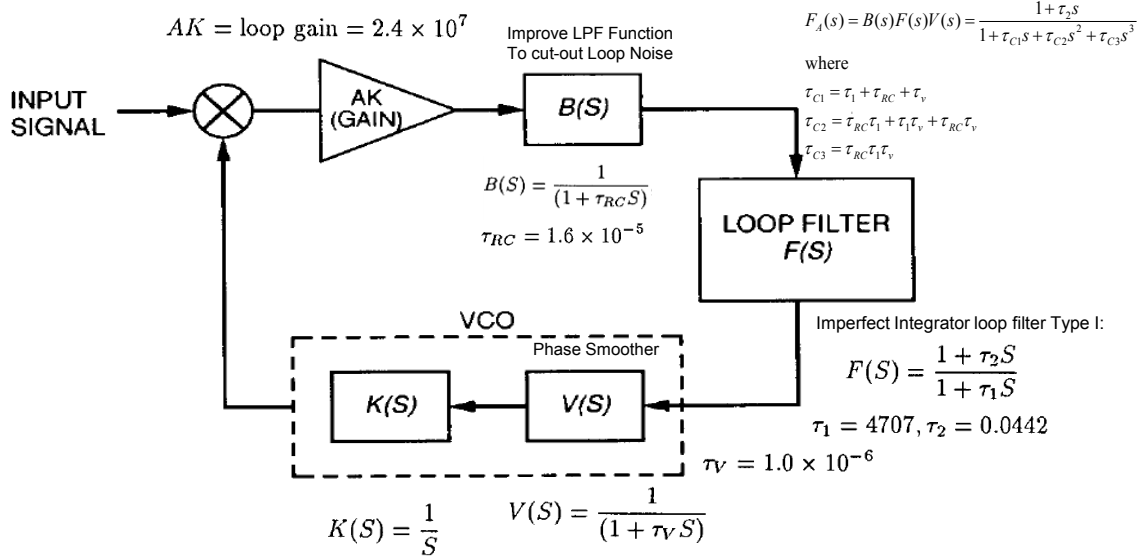


Figure 18. Advanced Second-Order PLL Employed by NASA Spacecraft and Satellites

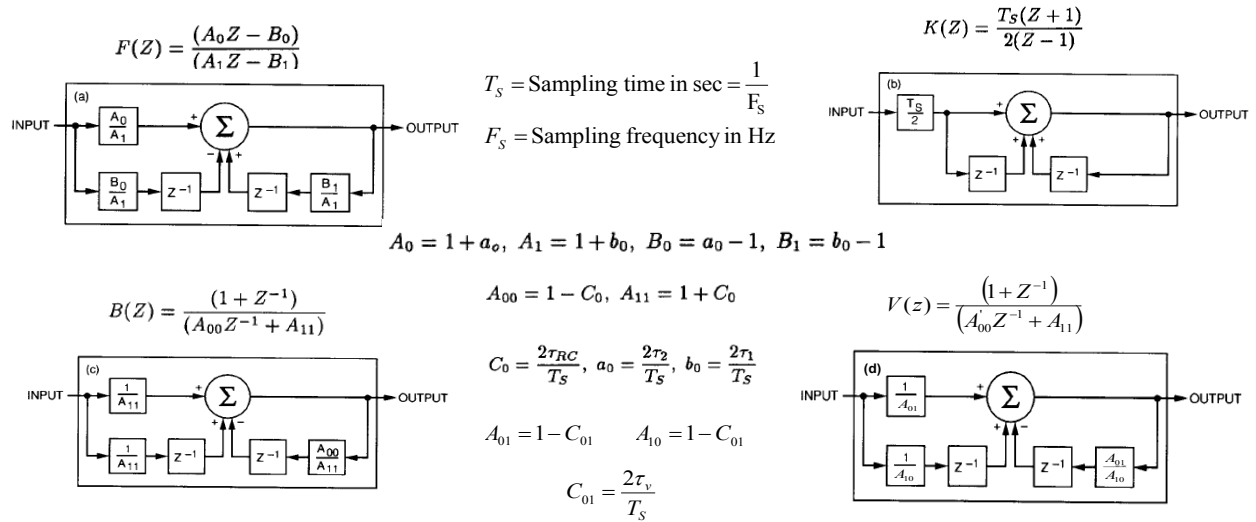


Figure 19. Recursive Implementation of $F(z)$, $B(z)$, $K(z)$ and $V(z)$ Using Bilinear Transformation

The sampling frequency, f_s , for the digital filters must be selected to satisfy: $f_s > 1 \text{ MHz}$.
 The loop bandwidth, B_{DL} , for tracking mode must be selected to satisfy: $B_{DL}T_s = B_{DL}T_b < 0.01$.
 where T_b is the symbol time duration.

The carrier loop SNR, or $LSNR$, for tracking mode in the absence of RFI is found to be:

$$LSNR = \frac{J_0^2(m)P_T}{N_0B_{DL}} \quad (12)$$

The carrier $LSNR$ for acquisition mode in the absence of RFI is defined as:

$$LSNR_{Acq} = \frac{J_0^2(m)P_T}{N_0B_{Acq-DL}} \quad (13)$$

A typical second-order PLL employed by civil and commercial satellites is shown in Figure 20. As shown in this figure, $B(s) = V(s) = 1$, and the loop filter, $F(s)$, is usually selected as a Type-II (imperfect integrator) or a Type-III (perfect integrator) filter. Note that the figure also defines the voltage controlled oscillator (VCO) gain in terms of the clock frequency and the number of bits in the accumulator. For imperfect loop filter Type-II, the open-loop response $G(s)$ is defined as:

$$G(s) = AK.K_{VCO} \cdot \frac{F(s)}{s} = \frac{AK.K_{VCO}}{s} \left[\frac{1+s\tau_2}{s\tau_1} \right] \quad (14)$$

For perfect loop filter, the closed-loop response $H(s)$ is defined as:

$$H(s) = \frac{G(s)}{1+G(s)} = \frac{(A+Bs)e^{-sT_D}}{s^2 + (A+Bs)} \quad (15)$$

where

$$\begin{aligned} a &= \tau_1.AK.K_{VCO} \\ b &= \tau_2.AK.K_{VCO} \end{aligned} \quad (16)$$

When the time delay is zero, the closed-loop filter becomes:

$$H(s) = \frac{\varpi_N^2 + 2\zeta\varpi_N s}{s^2 + 2\zeta\varpi_N s + \varpi_N^2} \quad (17)$$

The loop noise bandwidth is found as:

$$\begin{aligned} B_L &= \text{Loop noise bandwidth (BW) in Hz} \\ B_L &= \int_{-\infty}^{\infty} |H(f)|^2 df = \varpi_N \left[\zeta + \frac{1}{4\zeta} \right] \end{aligned} \quad (18)$$

where

$$\begin{aligned}\varpi_N &= \text{Natural frequency of the loop in rad/sec} = \sqrt{a} = \sqrt{\tau_1 \cdot AK \cdot K_{VCO}} \\ \zeta &= \text{Loop damping factor} = \frac{b}{2\varpi_N} = \frac{b}{2\sqrt{\tau_1 \cdot AK \cdot K_{VCO}}}\end{aligned}\quad (19)$$

For perfect loop filter, the open-loop response $G(s)$ is defined as:

$$G(s) = AK \cdot K_{VCO} \cdot \frac{F(s)}{s} = \frac{AK \cdot K_{VCO}}{s} \left[\frac{\tau_1}{s} + \tau_2 \right] e^{-sT_D} \quad (20)$$

For perfect loop filter, the closed-loop response $H(s)$ becomes:

$$H_p(s) = \frac{G(s)}{1 + G(s)} = \frac{(A + Bs)}{s^2 + (A + Bs)}, \quad (21)$$

where

$$\begin{aligned}A &= \frac{AK \cdot K_{VCO}}{\tau_1} \\ B &= \frac{\tau_2}{\tau_1} \cdot AK \cdot K_{VCO}\end{aligned}\quad (22)$$

Similarly, the loop bandwidth for a perfect loop filter is found to be the same as before:

$$B_{LP} = \int_{-\infty}^{\infty} |H(f)|_P^2 df = \varpi_{NP} \left[\zeta_P + \frac{1}{4\zeta_P} \right], \quad (23)$$

and

$$\begin{aligned}\varpi_{NP} &= \text{Natural frequency of the loop in rad/sec} = \sqrt{A} = \sqrt{\frac{AK \cdot K_{VCO}}{\tau_1}} \\ \zeta_P &= \text{Loop damping factor} = \frac{B}{2\varpi_N} = \frac{B}{2\sqrt{\frac{AK \cdot K_{VCO}}{\tau_1}}}\end{aligned}\quad (24)$$

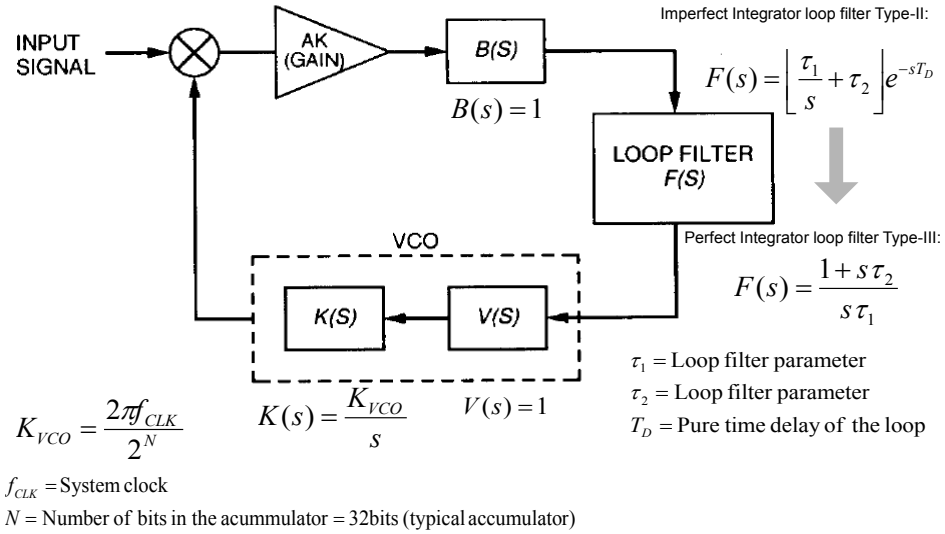


Figure 20. Typical Second-Order PLL Employed by Civil and Commercial Satellites

3.3.4 Existing Carrier Acquisition Approaches

Most USB Command Detector Unit (CDU) performs carrier acquisition at the satellite by going through four carrier modulation mode (CMM) recommended by the Consultative Committee for Space Data System (CCSDS) listed in Table 3.

Table 3. Carrier Modulation Mode (CMM) for SATOPS USB Acquisition

CARRIER MODULATION MODE (CMM)	DESCRIPTION
CMM-1	UNMODULATED CARRIER ONLY
CMM-2	CARRIER MODULATED* WITH "ACQUISITION SEQUENCE"
CMM-3	CARRIER MODULATED WITH COMMAND DATA
CMM-4	CARRIER MODULATED WITH "IDLE SEQUENCE"

For CMM-2, the “acquisition sequence” is usually an alternating sequence (+1) with a predefined length, L , in terms of number of command bits N . The length L is usually selected using the following relationship:

$$L = 2^N \quad (25)$$

The “idle sequence” is usually a non-alternating sequence.

CCSDS also recommends two approaches for the carrier frequency. The approaches are described in Figure 21. The main difference between the two approaches is the approach for reacquiring the carrier when the subcarrier and/or data timing synchronizers drop lock. Approach 1 assumes the subcarrier and/or data timing synchronizers drop lock, but the carrier synchronizer is still “in lock”. Approach 2 assumes the subcarrier and/or data timing synchronizers drop lock and the carrier synchronizer is also “drop lock”. The carrier acquisition mode includes carrier frequency acquisition and carrier phase acquisition modes. The subsections below describe these two modes.

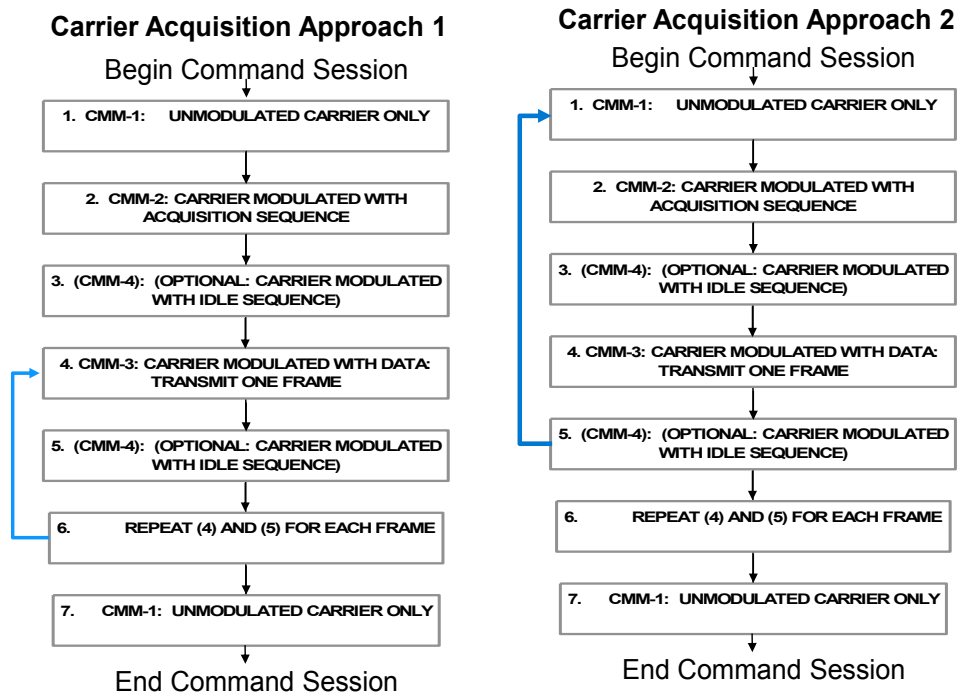


Figure 21. Carrier Acquisition Approaches for USB SATOPS Systems

3.3.4.1 Carrier Frequency Acquisition Mode

The most commonly used technique for frequency acquisition mode is the frequency sweep technique shown in Figure 22. The technique consists of the following steps:

- Step 1: Select the frequency sweep rate based on the estimated received carrier signal-to-noise power ratio, or CNR, or carrier SNR.
 - The frequency sweep rate as a function of received signal power is derived based on simulation and actual operational data.
- Step 2: Uplink command carrier frequency is swept during carrier acquisition using the selected sweep rate.
- Step 3: When the command signal carrier frequency and the receiver PLL VCO frequency coincide, the PLL will lock onto the carrier signal.
 - Assuming that the selected sweep rate is not too large.

In practice, the SATOPS USB receiver utilizes a hard limiter in front of the PLL to control the tracking loop. The second-order PLL is typically employed by military, civil and commercial satellites for tracking the carrier signal component. The minimum sweep rate and probability of lock for the loop are usually obtained by simulation using actual operating conditions. When the carrier is acquired, the PLL will track it with certainty, i.e., with probability of lock greater than 90%. Figure 23 shows the minimum sweep rate and probability of lock as a function of the received power.

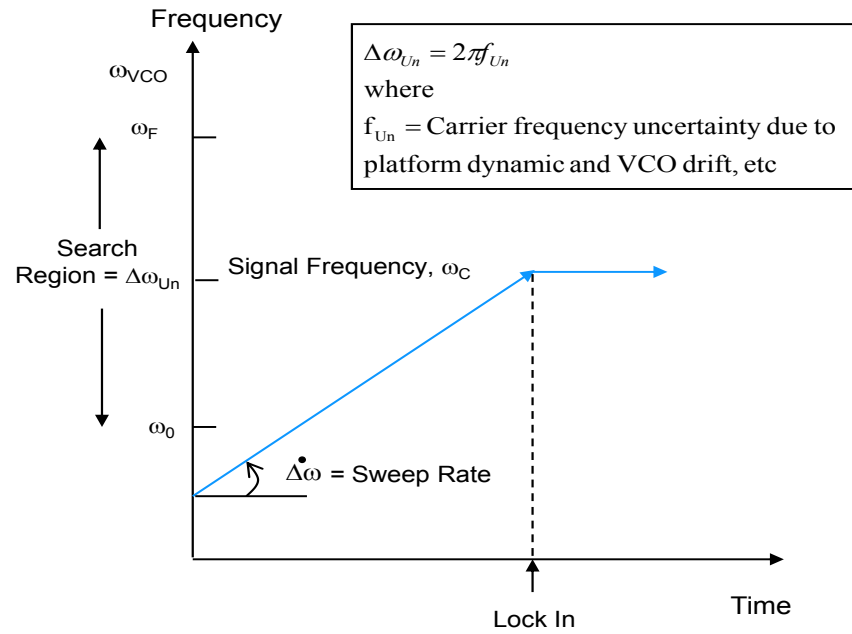


Figure 22. Carrier Frequency Acquisition Using Frequency Sweep Technique

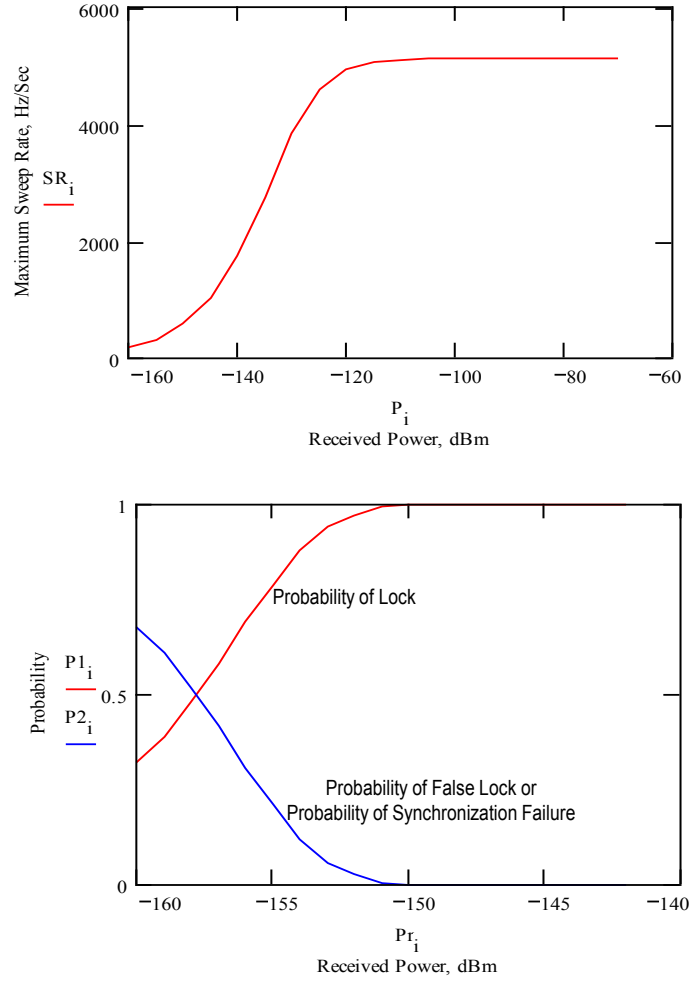


Figure 23. Minimum Sweep Rate and Probability of Lock as a Function of Receive Power

3.3.4.2 Carrier Frequency Acquisition Time Using Sweeping Technique

For the frequency sweep technique, the carrier frequency acquisition time, T_{acq} , is developed using the minimum sweep rate specified in Figure 23 and simulation results using actual operational conditions from practical SATOPS missions, and it is found to be:

$$T_{freq} = \frac{\Delta\omega_{Un}}{\Delta\dot{\omega}} = \frac{2\pi f_{Un}}{\Delta\dot{\omega}}, \quad (26)$$

where f_{Un} is the frequency uncertainty due to Doppler and drift of the voltage controlled oscillator and,

$$\Delta \dot{\omega} = \text{Sweep rate in Hz/sec} = \omega_N^2 \left[1 - \left(\frac{1}{\text{Loop SNR}_{\text{Acq}} - 2} \right)^{1/2} \right], \text{ for } 3 < \text{Loop SNR}_{\text{Acq}} < 4.75 \quad (27)$$

$$\Delta \dot{\omega} = \begin{cases} \omega_N^2 \left[1 - \left(\frac{2}{\text{Loop SNR}_{\text{Acq}} - 4} \right)^{1/2} \right], & \text{for } 6 < \text{Loop SNR}_{\text{Acq}} < 9.5 \\ \frac{\omega_N^2}{2}, & \text{for } \text{Loop SNR}_{\text{Acq}} \geq 9.5 \end{cases} \quad (28)$$

$$\omega_N^2 = \frac{2B_{LAcq}}{\zeta} \left[1 + \frac{1}{\zeta^2} \right], \zeta = 0.707$$

$$B_{LAcq} = \text{Acquisition loop bandwidth} \quad (29)$$

Note that during acquisition, the loop SNR is defined as:

$$\text{Loop SNR}_{\text{Acq}} = \frac{J_0^2(m)P_T}{N_0 B_{LAcq}} \quad (30)$$

Note that without loss of generality, one can assume the channel gain factor is equal to unity.

3.3.4.3 Carrier Phase Acquisition Mode

For carrier phase acquisition mode, the most commonly used techniques in practice are carrier phase sweep and synchronization (or sync) word. The carrier phase acquisition process is described in Figure 24 and is briefly described below:

T_0 = Time required for the PLL to estimate the initial phase θ_0 , and

T_e = Time it takes the PLL to reach steady state phase error θ_e .

The carrier phase acquisition time, T_{PAcq} , is calculated using the following relationship:

$$T_{PAcq} = T_0 + T_e \quad (31)$$

The carrier phase acquisition time improves significantly with phase-aided acquisition using the sync word, or phase sweeping technique, to estimate initial phase. The discussion of these techniques is provided below.

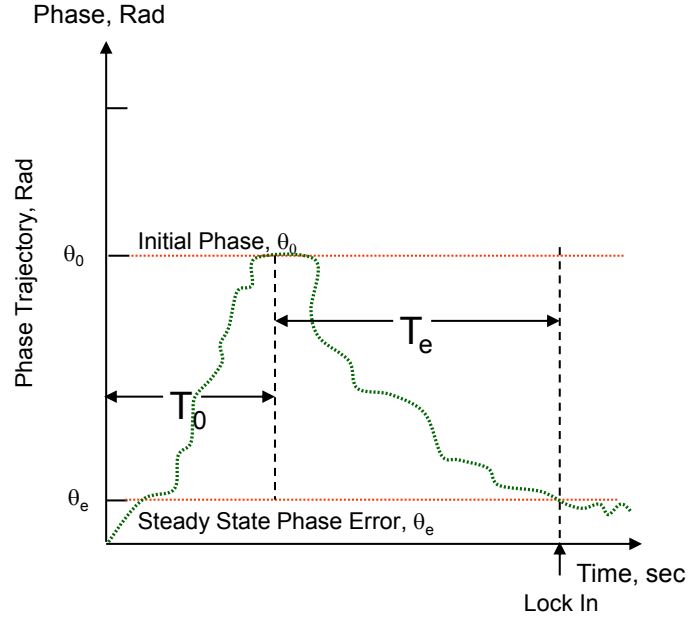


Figure 24. Phase Acquisition Process of a PLL

3.3.4.4 Carrier Phase Acquisition Using Sync Word Technique

Typical carrier phase acquisition technique is to use sync word (or alternating sequence or acquisition sequence) to estimate initial phase. This subsection assumes that the Doppler frequency and timing are known in advance and that the command data is formatted as an NRZ rectangular data pulse, i.e.,

$$p(t) = \begin{cases} 1, & 0 \leq t \leq T_b \\ 0, & \text{elsewhere} \end{cases} \quad (32)$$

It is also assumed that the sync word or acquisition sequence with length L is known, and the sync word is transmitted during CMM-2 (see Figure 20 and Figure 21), using direct modulation with word sequence. Mathematically, the carrier signal modulated with an acquisition sequence can be expressed as:

$$\begin{aligned}
\tilde{S}_{CMM-2}(t) &= \sqrt{2P_T} d_{Acq}(t) [\exp(j(2\pi(f_c + f_d)t + \theta_c))] \\
S_{CMM-2}(t) &= \text{Real}\left\{\tilde{S}_{CMM-2}(t)\right\} \\
d_{Acq}(t) &= \sum_{n=-L/2}^{L/2} C_n \cdot p(t - nT_b),
\end{aligned} \tag{33}$$

where

f_d = Doppler shift due to satellite movement,

θ_c = Received carrier phase shift of the desired signal, and

C_n = Acquisition sequence with length L .

The carrier signal modulated with an acquisition sequence or sync word sequence is received at the SATOPS USB receiver-demodulator and processed by a typical Maximum Likelihood (ML) phase estimator shown in Figure 25.

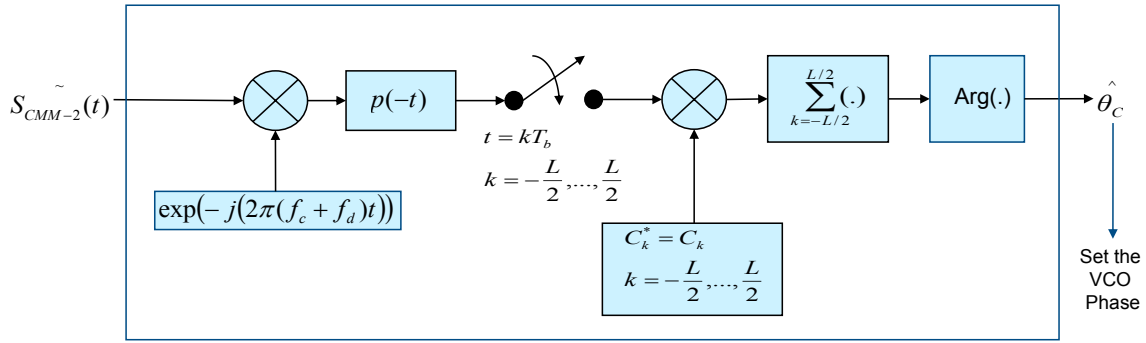


Figure 25. Typical Maximum Likelihood (ML) Phase Estimator

The performance of the ML phase estimator shown in Figure 25 is expressed in terms of the variance of the estimated carrier phase, which is given by [5]:

$$\sigma_{\hat{\theta}_c}^2 = \text{var}\left\{\hat{\theta}_c - \theta_c\right\} = \frac{1}{2L} \frac{N_0}{(2J_1^2(m)P_T T_b)} = \left(\frac{1}{2L}\right) \left[\frac{1}{\text{Bit SNR}_{Acq}} \right]$$

where

$$\text{Bit SNR}_{Acq} = \frac{2J_1^2(m)P_T T_b}{N_0} \tag{34}$$

The above equation as a function of bit SNR is only for acquisition mode, and without loss of generality, one can assume the channel gain factor is equal to unity. For a given bit SNR and a

specified variance of the estimated carrier phase, the length of the sync word sequence is determined using Equation (34).

3.3.4.5 *Carrier Phase Acquisition Time Using Sync Word*

The length of sync word must be selected to ensure the variance of the carrier phase estimate error is small such that the time it takes the PLL to reach steady-state phase error, θ_e , is about $1/2B_{Acq-DL}$. The acquisition models presented here ensure the probability of synchronization failure at 10^{-8} . The phase sync work can be computed from:

$$T_{Phase_Sync} = \frac{1}{2B_{LAcq}} + LT_b, \quad (35)$$

where

L = length or number of bits in the sync word,
 T_b = sync work bit duration in seconds, and
 B_{LAcq} = acquisition loop bandwidth in Hz.

3.3.4.6 *Carrier Phase Acquisition Time Using Phase Sweeping Technique*

Based on the simulation results using the various sources, the carrier phase acquisition time using phase sweeping technique is found to be:

$$T_{Phase_Swp} = \begin{cases} \frac{1}{2B_{LAcq}} + \frac{12.2}{4B_{LAcq}}, & \text{for Loop SNR}_{Acq} = 10 \text{ dB} \\ \frac{1}{2B_{LAcq}} + \frac{8}{4B_{LAcq}}, & \text{for Loop SNR}_{Acq} = 14 \text{ dB} \end{cases}. \quad (36)$$

The total carrier acquisition time, T_{acq} , is calculated using the following relationship:

$$T_{Acq} = T_{Freq} + T_{Phase}, \quad (37)$$

where T_{Freq} is defined in (26), and T_{Phase} is defined as in (35) or (36), depending on the phase sync technique used by the SATOPS USB receiver.

3.3.5 **Analytical Models for Assessing PLL Acquisition Performance in the Presence of RFI**

This section presents analytical models for evaluating the impacts of CW and wideband RFI signals on the second order PLL acquisition performance.

3.3.5.1 Analytical Models of PLL Acquisition with CW RFI

Recall from previous section, the CW RFI signal is defined as:

$$I(t) = \sqrt{2P_I} \cos(2\pi(f_c + \Delta f_c)t + \theta_I), \quad (38)$$

where

P_I = RFI power,

Δf_c = RFI frequency offset from the desired carrier frequency, f_c , and

θ_I = RFI phase.

For continuous wave (CW) RFI, the effects of RFI depend on the RFI carrier frequency, namely, case 1 for out-of-band interference, and case 2 for in-band interference. The in-band interference occurs when the RFI carrier frequency is within the carrier acquisition loop bandwidth, B_{LAcq} , and the out-of-band interference happens when RFI carrier frequency is outside the carrier tracking loop bandwidth.

3.3.5.1.1 Case 1: $\Delta f_c > B_{LAcq}$

For case 1, the loop SNR in the presence of CW RFI is given by:

$$LSNR_{CW-1} = \frac{LSNR_{Acq}}{\Delta_{Acq-1}}, \quad (39)$$

where

$$LSNR_{Acq} = \frac{J_0^2(m)P_T}{N_0 B_{LAcq}}, \text{ and } \Delta_{Acq-1} = 1. \quad (40)$$

For case 1, the carrier acquisition time, T_{acq} , remains the same as the non-interference case presented in the previous section.

3.3.5.1.2 Case 2: $\Delta f_c < B_{LAcq}$

For case 2, the loop SNR in the presence of CW RFI is given by:

$$LSNR_{CW-2} = \frac{LSNR_{Acq}}{\Delta_{Acq-2}}, \quad (41)$$

where

$$\Delta_{Acq-2} = [1 + INR], \quad (42)$$

and INR is the ratio of P_I / N_0 , the interference power-to-noise ratio. For case 2, the carrier acquisition time, $T_{\text{acq-CW-2}}$, will be longer due to the loop SNR degradation by a factor $\Delta_{\text{Acq-2}}$. The frequency sweep rate will be calculated using $LSNR_{\text{CW-2}}$, i.e.,

$$\Delta \omega_{\text{CW-2}} = \omega_N^2 \left[1 - \left(\frac{1}{\text{Loop SNR}_{\text{CW-2}} - 2} \right)^{1/2} \right], \text{ for } 3 < \text{Loop SNR}_{\text{CW-2}} < 4.75 \quad (43)$$

$$\Delta \omega_{\text{CW-2}} = \begin{cases} \omega_N^2 \left[1 - \left(\frac{2}{\text{LSNR}_{\text{CW-2}} - 4} \right)^{1/2} \right], & \text{for } 6 < \text{LSNR}_{\text{CW-2}} < 9.5 \\ \frac{\omega_N^2}{2}, & \text{for } \text{LSNR}_{\text{CW-2}} \geq 9.5 \end{cases} \quad (44)$$

$$\omega_N^2 = \frac{2B_{LAcq}}{\zeta} \left[1 + \frac{1}{\zeta^2} \right], \zeta = 0.707$$

$$B_{LAcq} = \text{Acquisition loop bandwidth} \quad (45)$$

Again, without loss of generality, one can assume the channel gain factor is equal to unity. The carrier frequency acquisition time becomes:

$$T_{\text{Freq-CW-2}} = \frac{2\pi f_{Un}}{\Delta \omega_{\text{CW-2}}} \quad (46)$$

Similarly, for case 2, the carrier phase acquisition time becomes:

$$T_{\text{Phase_Swp-CW-2}} = \begin{cases} \frac{1}{2B_{Acq-DL}} + \frac{12.2}{4B_{Acq-DL}}, & \text{for } \text{LSNR}_{\text{CW-2}} = 10 \text{ dB} \\ \frac{1}{2B_{Acq-DL}} + \frac{8}{4B_{Acq-DL}}, & \text{for } \text{LSNR}_{\text{CW-2}} = 14 \text{ dB} \end{cases}, \quad (47)$$

where

$$T_{\text{Phase_Sync-CW-2}} = \frac{1}{2B_{LAcq}} + L_{\text{CW-2}} T_b$$

$L_{\text{CW-2}}$ = Required length or number of bits in the sync word in the presence of CW RFI

T_b = Sync word bit duration in second

(48)

For CW RFI case 2, the performance of the ML phase estimator becomes:

$$\sigma_{\hat{\theta}_{\text{C-CW-2}}}^2 = \left(\frac{1}{2L_{\text{CW-2}}} \right) \left[\frac{(1 + INR)}{\text{Bit SNR}_{\text{Acq}}} \right], \quad (49)$$

where bit SNR is defined as before, i.e.,:

$$\text{Bit SNR}_{\text{Acq}} = \frac{2J_1^2(m)P_T T_b}{N_0} \quad (50)$$

To compensate for the CW RFI, one can increase the length of the sync word or the bit SNR. For the phase sweep technique, the carrier acquisition time in the presence of CW RFI becomes:

$$T_{\text{Acq-Sweep-CW-2}} = T_{\text{Freq-CW-2}} + T_{\text{Phase_Swp-CW-2}} \quad (51)$$

For sync word technique, the carrier acquisition time is given by:

$$T_{\text{Acq-Phase-Sync-CW-2}} = T_{\text{Freq-CW-2}} + T_{\text{Phase_Sync-CW-2}} \quad (52)$$

3.3.5.2 Analytical Model of PLL Acquisition with WB RFI

Recall from the previous section, the wideband (WB) RFI signal is defined as:

$$I(t) = \sqrt{2P_I} d_I(t) \cos(2\pi(f_c + \Delta f_c)t + \theta_I), \quad (53)$$

where

$$d_I(t) = \sum_{n=-\infty}^{\infty} I_n \cdot p(t - nT_I - \tau),$$

P_I = RFI power,

T_I = RFI bit duration in seconds, and $T_I \leq T_b$,

Δf_c = RFI frequency offset from the desired carrier frequency, f_c , and

T_I = RFI phase.

The loop SNR in the presence of wideband (WB) RFI can be shown to have the following form:

$$LSNR_{WB} = \frac{LSNR_{\text{Acq}}}{\Delta_{\text{Acq-WB}}}, \quad (54)$$

where

$$LSNR_{\text{Acq}} = \frac{J_0^2(m)P_T}{N_0 B_{LAcq}}, \quad (55)$$

$$\begin{aligned} \Delta_{\text{Acq-WB}} &= \left[1 + \frac{P_I}{N_0} S_{\text{RFI-WB}}(B_{DL}, f_{Un}) \right], \frac{P_I}{N_0} = \text{INR} \\ S_{\text{RFI-WB}}(f, f_{Un}) &= [S_I(f - f_{Un}) + S_I(f + f_{Un})] \\ S_I(f) &= T_I \int_{-B_{Acq-DL}}^{B_{Acq-DL}} \left[\frac{\sin(\pi f T_I)}{\pi f T_I} \right]^2 df, \text{ where } T_I = 1 / R_I \end{aligned} \quad (56)$$

Again, f_{Un} is defined as the frequency uncertainty due to Doppler and VCO drift.

For the phase sweep technique, the carrier acquisition time in the presence of WB RFI becomes:

$$T_{Acq-Sweep-WB} = T_{Freq-WB} + T_{Phase_Swp-WB} \quad (57)$$

For sync word technique, the carrier acquisition time is:

$$T_{Acq-Phase-Sync-WB} = T_{Freq-WB} + T_{Phase_Sync-WB} \quad (58)$$

where:

$$T_{Freq-WB} = \frac{2\pi f_{Un}}{\Delta \omega_{WB}} \quad (59)$$

where:

$$\Delta \omega_{WB} = \begin{cases} \omega_n^2 \left[1 - \left(\frac{2}{\text{LSNR}_{WB} - 4} \right)^{1/2} \right], & \text{for } 6 < \text{LSNR}_{WB} < 9.5 \\ \frac{\omega_n^2}{2}, & \text{for } \text{LSNR}_{WB} \geq 9.5 \end{cases} \quad (60)$$

$$T_{Phase_Swp-WB} = \begin{cases} \frac{1}{2B_{LAcq}} + \frac{12.2}{4B_{LAcq}}, & \text{for } \text{LSNR}_{WB} = 10 \text{ dB} \\ \frac{1}{2B_{LAcq}} + \frac{8}{4B_{LAcq}}, & \text{for } \text{LSNR}_{WB} = 14 \text{ dB} \end{cases} \quad (61)$$

$$T_{Phase_Sync-WB} = \frac{1}{2B_{LAcq}} + L_{WB} T_b$$

L_{WB} = Required length or number of bits in the syncword in the presence of WB RFI

T_b = Sync word bit duration in second . (62)

For WB RFI, the performance of the ML phase estimator becomes:

$$\sigma_{\theta_{c-WB}}^2 = \left(\frac{1}{2L_{WB}} \right) \left| \frac{\Delta_{Acq-WB}}{\text{Bit SNR}_{Acq}} \right| \quad (63)$$

$$\begin{aligned} \Delta_{Acq-WB} &= [1 + INR.S_{RFI-WB}(B_{Acq-DL}, f_{Un})] \\ S_{RFI-WB}(f, f_{Un}) &= [S_I(f - f_{Un}) + S_I(f + f_{Un})] \\ S_I(f) &= T_I \int_{-B_{Acq-DL}}^{B_{Acq-DL}} \left[\frac{\sin(\pi f T_I)}{\pi f T_I} \right]^2 df, \text{ where } T_I = 1/R_I \end{aligned} \quad (64)$$

Approved for public release; distribution is unlimited.

For the ML phase estimator, the acquisition loop bandwidth, $B_{\text{Acq-DL}}$, is identical to L_{WB} . To compensate for the WB RFI, one can increase the length of the sync word or the bit SNR.

3.3.6 Analytical Models for Assessing PLL Lock Detector

Figure 26 shows how a PLL lock detector is integrated into the PLL operation for acquiring and tracking the carrier signal. Note that the parameters B_{DL} and $B_{\text{Acq-DL}}$ shown in Figure 26 denote the digital loop bandwidth for tracking and acquisition mode, respectively, assuming that the second-order PLL is implemented in the digital domain. Regardless of whether the loop is implemented in digital domain or analog domain, the loop bandwidth should be set the same for both cases, i.e., $B_{\text{DL}} = B_{\text{L}}$ and $B_{\text{Acq}} = B_{\text{Acq-DL}}$, where B_{L} and B_{Acq} are the analog loop bandwidth for tracking and acquisition modes, respectively.

As shown in Figure 26, the PLL initially will be in the acquisition mode, acquiring the carrier signal component. In this mode, the loop bandwidth will be open wide enough to cover the range of the expected frequency uncertainty of the carrier signal, normally 110 kHz for SATOPS applications. During this mode, the phase lock loop will monitor the carrier phase error over an observation time T_{L} . If the phase error is less than a threshold values σ_{Thcar} , then the PLL will switch to the tracking mode. For the tracking mode, the PLL tracking loop bandwidth will be set according to the loop bandwidth product $B_{\text{L}}T_{\text{b}} \leq 0.01$, where T_{b} is the command data bit duration. This section describes how the threshold values σ_{Thcar} and T_{L} are set for the optimum lock detector performance.

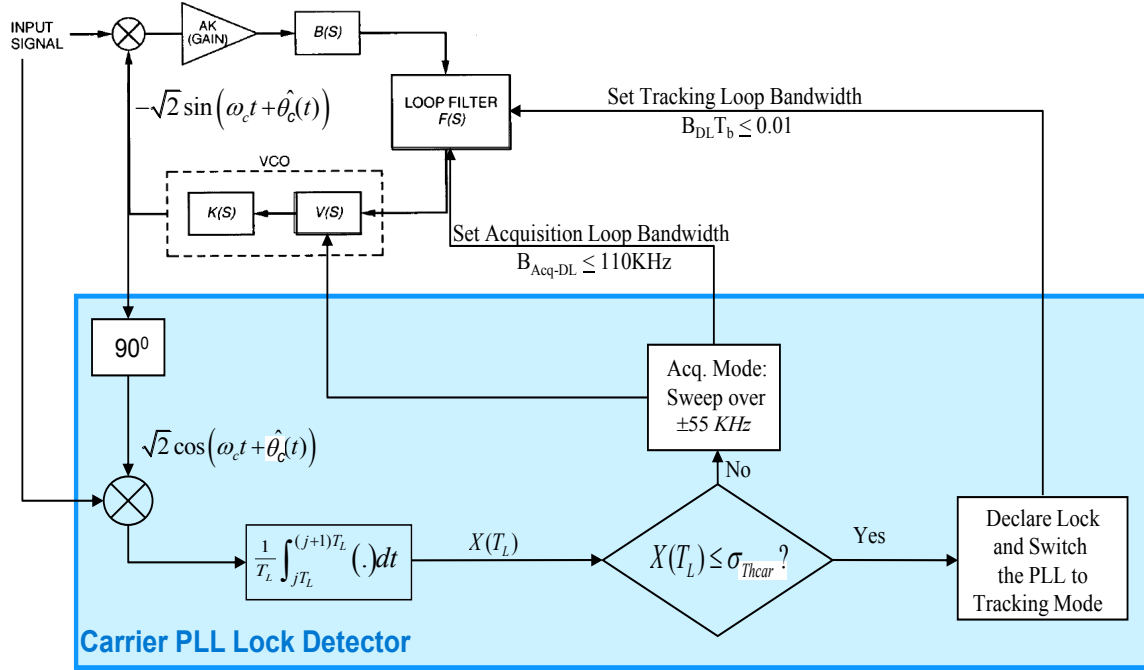


Figure 26. Typical PLL Lock Detector Employed By Civil, Commercial and Military SATOPS Satellites

The value σ_{Thecar} is selected to ensure the probability of lock is greater than 90%. Theoretically, it is chosen by using the following relationship:

$$\sigma_{Thecar} = \left[\frac{1}{\sqrt{LSNR_{Eff}}} + \sigma_{Margin} \right] (Radians). \quad (65)$$

The effective loop SNR ($LSNR_{eff}$) shown in (65) is defined as the loop SNR in the presence of noisy carrier reference for a specified BER performance. The $LSNR_{eff}$ can be calculated using (70) shown below, and σ_{Margin} is the phase error margin that is specified by the communications designer to take into account the phase jitter caused by VCO drift, residual Doppler, phase noise, etc. In practice, the phase error margin can be 5% to 10% of the value of $1/\sqrt{LSNR_{eff}}$.

The value σ_{Thecar} is selected using the effective loop SNR that is evaluated in the absence of RFI. It is assumed that the PLL tracking error follows the Tikhonov distribution and that the carrier tracking phase error is small. By using Taylor series expansion on the average uncoded BER equation, one can approximate the uncoded BER as [6]:

$$BER_{RL} = \frac{1}{2} \operatorname{erfc}\{\sqrt{BSNR_0}\} + \frac{1}{2} \sqrt{\frac{1}{\pi} BSNR_0 \sigma_\theta^2} e^{-\{BSNR_0\}}$$

where

$$BSNR_0 = 2J_1^2(m) \frac{P_T T_b}{N_0}$$

$$\sigma_\theta^2 = \frac{1}{LSNR_0}$$
(66)

As before, if one defines the PLL tracking loop bandwidth as B_L and the carrier tracking loop SNR, $LSNR_0$ as:

$$LSNR_0 = J_0^2(m) \frac{P_T}{N_0 B_L},$$
(67)

then the uncoded BER, in the absence of RFI with small carrier tracking error, can be rewritten as a function of the carrier tracking loop SNR, $LSNR_0$:

$$BER_{RL} = \frac{1}{2} \operatorname{erfc}\{\sqrt{\alpha(B_L T_b) LSNR_0}\} + \frac{1}{2} \frac{\sqrt{\frac{1}{\pi} \alpha(B_L T_b) LSNR_0}}{LSNR_0} e^{-\{\alpha(B_L T_b) LSNR_0\}},$$
(68)

where

$$\alpha = 2 \frac{J_1^2(m)}{J_0^2(m)}.$$
(69)

The first term of (68) represents the ideal BER performance with perfect carrier tracking, and the second term is the BER degradation due to imperfect carrier tracking due to the presence of AWGN. The imperfect carrier tracking is represented by the carrier tracking jitter, σ_θ^2 . This term is also defined as the “Radio Loss” (RL). From (68), the effective loop SNR is defined as:

$$\text{Effective Loop SNR} = LSNR_{\text{Eff}} = \alpha(B_L T_b) LSNR_0.$$
(70)

Substituting (70) into (68), the uncoded BER becomes:

$$BER_{RL} = \frac{1}{2} \operatorname{erfc}\{\sqrt{LSNR_{\text{Eff}}}\} + \frac{\alpha(B_L T_b)}{2} \frac{\sqrt{\frac{1}{\pi} LSNR_{\text{Eff}}}}{LSNR_{\text{Eff}}} e^{-\{LSNR_{\text{Eff}}\}}.$$
(71)

The effective loop SNR must be chosen for the uncoded BER to meet the desired threshold BER value, e.g., $BER_{\text{Threshold}} = 10^{-9}$ or 10^{-6} .

The effective loop SNR must also be chosen to ensure that the mean time between cycle slips, T_{MBCS} , is sufficiently large that probability due to cycle slip occurring due to noise can be ignored:

$$T_{\text{MTBCS}} \approx \frac{2}{B_L} e^{\{\pi \cdot \text{LSNR}_{\text{Eff}}\}} \quad (72)$$

To ensure a small probability of false lock at approximately 10^{-4} [6], the integration time T_L of the PLL detector can be set as follows:

$$T_L \approx \frac{1}{0.018 * \text{LSNR}_{\text{Eff}} * B_L} \quad (73)$$

Effective loop SNR must be set to meet the specified uncoded BER performance and mean time between cycle slips. The above equations are used to determine the required carrier-to-noise power spectral density (C/N_0).

3.3.7 Analytical Models for Assessing PLL Tracking Performance

This section describes analytical models for evaluating the impacts of CW and wideband RFI signals on the PLL tracking performance.

3.3.7.1 Analytical Model of PLL Tracking Jitter in the Absence of RFI

The performance of the PLL is characterized by the variance of the tracking phase error, $\sigma_{\theta_c}^2$, and in the absence of RFI, it is given by:

$$\sigma_{\theta_c}^2 = \frac{\Delta}{\text{LSNR}} \quad (74)$$

where

$$\begin{aligned}
LSNR &= \text{Loop SNR} = \frac{P_C}{N_0 B_L}, \text{ Note that } P_C / N_0 \text{ is the carrier SNR} \\
P_C &= J_0^2(m) P_T \\
\Delta &= \left[1 + \frac{P_C}{N_0} S_{CD}(1,0) \right] \\
S_{CD}(k, f) &= \sum_{k=1, k=\text{odd}}^{\infty} J_k^2(m) [S_d(f - kf_{SC}) + S_d(f + kf_{SC})] \\
S_d(f) &= T_b \int_{-B_L}^{B_L} \left[\frac{\sin(\pi f T_b)}{\pi f T_b} \right]^2 df, \text{ where } T_b = 1 / R_b
\end{aligned} \tag{75}$$

Note that without loss of generality, one can assume the channel gain factor is equal to unity.

Note that when $f_{sc} > 4R_b$, $\sigma_{\theta_c}^2$ becomes:

$$\sigma_{\theta_c}^2 \approx \frac{1}{LSNR} \tag{76}$$

In practice, for reliable tracking, the loop SNR is usually set at about 11 dB or more to ensure reliable tracking performance.

3.3.7.2 Analytical Model of PLL Tracking Jitter with CW RFI

A continuous wave (CW) RFI signal is defined as:

$$I(t) = \sqrt{2P_I} \cos(2\pi(f_c + \Delta f_c)t + \theta_I), \tag{77}$$

where

P_I = RFI power,

Δf_c = RFI frequency offset from the desired carrier frequency, f_c , and

θ_I = RFI phase.

3.3.7.2.1 Case 1: $\Delta f_c > B_{DL}$

For Case 1, the variance of the tracking phase error, $\sigma_{\theta_c}^2$, in the presence of CW RFI can be shown to have the following form:

$$\sigma_{\theta_c}^2 = \frac{\Delta}{LSNR} \tag{78}$$

Here, Δ is defined as in (74), and for $f_{sc} \geq 4R_b$, $\Delta = 1$.

3.3.7.2.2 *Case 2: $\Delta f_c < B_{DL}$*

For Case 2, the variance of the tracking phase error, $\sigma_{\theta_c}^2$, in the presence of CW RFI can be shown to have the following form:

$$\begin{aligned}\sigma_{\theta_c}^2 &= \frac{\Delta_{CW}}{LSNR} \\ \Delta_{CW} &= [1 + INR] \\ INR &= \frac{P_I}{N_0} = \text{Interference - to - noise power ratio}\end{aligned}\tag{79}$$

Here, one can assume that $f_{sc} \geq 4R_b$. Note that when INR is greater than the carrier SNR, the PLL will drop lock on the command signal and lock onto the CW RFI signal. Note that for this case, the effective loop SNR, $LSNR_{Eff}$, is calculated from (79), using: $LSNR_{Eff} = \frac{LSNR}{\Delta_{CW}}$. Using this effective loop SNR, one can calculate the SATOPS BER performance in the presence of AWGN and CW RFI taking into account of imperfect carrier synchronization using (71).

3.3.7.3 *Analytical Model of PLL Tracking Jitter with WB RFI*

Recall from the previous sections, the WB RFI signal is defined as:

$$\begin{aligned}I(t) &= \sqrt{2P_I} d_I(t) \cos(2\pi(f_c + \Delta f_c)t + \theta_I) \\ d_I(t) &= \sum_{n=-\infty}^{\infty} I_n \cdot p(t - nT_I - \tau), \\ \text{where} \\ P_I &= \text{RFI power} \\ T_I &= \text{RFI bit duration in seconds, where } T_I \leq T_b \\ \Delta f_c &= \text{RFI frequency offset from the desired carrier frequency } f_c \\ \theta_I &= \text{RFI phase}\end{aligned}\tag{80}$$

The variance of the tracking phase error, $\sigma_{\theta_c}^2$, in the presence of CW RFI can be shown to have the following form:

$$\sigma_{\theta_c}^2 = \frac{\Delta_{WB}}{LSNR}\tag{81}$$

Here, one can assume that $f_{sc} > 4R_b$, and the degradation factor Δ_{WB} is found to be:

$$\begin{aligned}
\Delta_{WB} &= [1 + INR \cdot S_{WB}(B_L, T_I, \Delta f_C)] \\
INR &= \frac{P_I}{N_0} \\
S_{WB}(f, T_I, \Delta f_C) &= \frac{1}{2} [S_{RFI}(f - \Delta f_C) + S_{RFI}(f + \Delta f_C)]
\end{aligned} \tag{82}$$

where

$$S_{RFI}(f) = T_I \int_{-B_L}^{B_L} \left[\frac{\sin(\pi f T_I)}{\pi f T_I} \right]^2 df$$

here

$$T_I = 1/R_I \leq T_b = 1/R_b$$

Note that for this case, the effective loop SNR, $LSNR_{Eff}$, is calculated from (81), using:

$LSNR_{Eff} = \frac{LSNR}{\Delta_{WB}}$. Again, using this effective loop SNR, one can calculate the SATOPS BER performance in the presence of AWGN and WB RFI taking into account of imperfect carrier synchronization using (71).

3.3.7.4 Mean Value of Tracking Error in the Presence of RFI

This section derives a simulation model to characterize the mean value of the phase error in the presence of RFI signal. The model presented here assumes that the PLL is in acquisition mode at Carrier Modulation Mode 2 (CMM-2). This means the transmitted SATOPS signal uses direct modulation with a known acquisition sequence, $d_{Acq}(t)$. For this case, the received signal at the satellite is given by:

$$\begin{aligned}
R_{CMM-2}(t) &= S_{CMM-2}(t) + I(t) + n(t) \\
\text{where} \\
S_{CMM-2}(t) &= \sqrt{2P_T} d_{Acq}(t) \cos(2\pi(f_c + f_d)t + \theta_c)
\end{aligned} \tag{83}$$

where $n(t)$ is the AWGN defined earlier.

3.3.7.4.1 CW RFI Case: $\Delta f_c > B_L$

As defined previously, the CW RFI signal $I(t)$ is given by:

$$I(t) = \sqrt{2P_I} \cos(2\pi(f_c + \Delta f_c)t + \theta_I) \tag{84}$$

The received signal becomes:

$$R_{\text{CMM-2}}(t) = \sqrt{2P_T} d_{\text{Acq}}(t) \cos(2\pi(f_c + f_d)t + \theta_c) + \sqrt{2P_I} \cos(2\pi(f_c + \Delta f_c)t + \theta_I) + n(t) \quad (85)$$

The VCO signal is defined as:

$$VCO(t) = \sin(2\pi(f_c + f_d)t + \theta_{VCO}(t)) \quad (86)$$

Assume that the acquisition sequence is perfectly removed by the correlation processing at the satellite receiver. The tracking error signal, $e(t)$, is formed by:

$$e_{\text{CW}}(t) = VCO(t) \cdot R(t) \cdot d_{\text{Acq}}(t) \approx \sqrt{2P_T} \sin(\theta_{VCO}(t) - \theta_c) + \sqrt{2P_I} \sin(\theta_{VCO}(t) - \theta_{\text{CW}}(t)) d_{\text{Acq}}(t) + n_{\text{LPF}}(t)$$

where

$$\theta_{\text{CW}}(t) = 2\pi(f_d - \Delta f_c)t + \theta_I$$

$$n_{\text{LPF}}(t) = \text{Low pass filter version of the AWGN} \quad (87)$$

The mean value of the tracking error signal is found to be:

$$E[e_{\text{CW}}(t)] \approx \sqrt{2P_T} E[\theta_{VCO}(t) - \theta_c]$$

Assuming that $(\theta_{VCO}(t) - \theta_c)$ is small

$$(88)$$

For CW RFI, the mean value of the interference signal has been removed during the sync word correlation processing as shown in (87), and the mean value of the tracking error is the average of the difference between the incoming carrier phase and the VCO's phase.

3.3.7.4.2 WB RFI Case

As defined previously, the WB RFI signal $I(t)$ is given by:

$$I(t) = \sqrt{2P_I} d_I(t) \cos(2\pi(f_c + \Delta f_c)t + \theta_I) \quad (89)$$

Assume that the acquisition sequence is perfectly removed by the correlation processing, the tracking error signal $e(t)$ is found to be:

$$e_{\text{WB}}(t) = VCO(t) \cdot R(t) \cdot d_{\text{Acq}}(t) \approx \sqrt{2P_T} \sin(\theta_{VCO}(t) - \theta_c) + \sqrt{2P_I} d_{\text{Acq}}(t) \cdot d_I(t) \sin(\theta_{VCO}(t) - \theta_{\text{CW}}(t)) + n_{\text{LPF}}(t) \quad (90)$$

Assume the acquisition sequence and $d_{\text{Acq}}(t)$ are independent. We get:

$$E[e_{\text{WB}}(t)] \approx \sqrt{2P_T} E[\theta_{VCO}(t) - \theta_c]$$

Assuming that $(\theta_{VCO}(t) - \theta_c)$ is small

$$(91)$$

Equation (91) shows that the mean value of the PLL tracking error is found to be the same as the CW RFI case.

3.3.8 RFI Detection Models

Currently, there are three approaches for the RFI detection, namely:

- Approach #1: Employ ITU and NTIA definitions for “harmful” interference and use the maximum allowable PFD (Power Flux Density) expressed in dB/m²/Hz to determine whether harmful interference has occurred.
- Approach #2: Monitor the received BER and when the received BER falls below a threshold value for T_{RFI} second, one can declare an RFI event has occurred.
- Approach #3: Monitor the sync errors, if they exceed the threshold values for T_{RFI} seconds, then one can declare an RFI event has occurred.

As indicated in the introduction and our survey results presented in Sections 3.1 and Section 3.2, Approach #1 and Approach #2 are the ones that are currently adopted by many existing RFI analysis tools. Our research effort considered a combined Approach # 2 and Approach #3 to detect an RFI event. The combined approach takes into consideration of the synchronization loops and BER performance of the SATOPS system. The combined approach includes the following steps:

- Step 1: Assume the PLL is in tracking mode, monitor the carrier PLL tracking error, σ_{Tracking} :
 - RFI is flagged when the PLL carrier tracking phase error σ_{Tracking} exceeds a predefined threshold value $\sigma_{\text{Threshold}}$ for T_{RFI} second, i.e., $\sigma_{\text{Tracking}} > \sigma_{\text{Threshold}}$ for T_{RFI} seconds.
 - From Section 3.3.6, the carrier PLL tracking error, σ_{Tracking} , is evaluated using the following relationships:

$$\sigma_{\text{Tracking}}^2 = \frac{\Delta_{\text{RFI}-i}}{LSNR_0}, i = 1, 2 \quad (92)$$

Recall that $LSNR_0$ is the loop SNR, which is defined as:

$$LSNR_0 = J_0^2(m) \frac{P_T}{N_0 B_L} \quad (93)$$

For $i = 1$, the loop receives the desired carrier signal component in the presence of CW RFI, and $\Delta_{\text{RFI}-1}$ is given by, from Section 3.3.6:

$$\Delta_{RFI-1} = [1 + INR]$$

where

$$INR = \frac{P_I}{N_0} \quad , \quad (94)$$

where INR is defined as the Interference power-to-Noise Ratio. For $i = 2$, the loop receives the desired carrier signal component in the presence of WB RFI, and Δ_{RFI-2} is given by, from Section 3.3.7:

$$\begin{aligned} \Delta_{Acq-WB} &= [1 + (INR) \cdot S_{RFI-WB}(B_{DL}, f_{RFI})] \\ S_{RFI-WB}(f, f_{Un}) &= [S_I(f - f_{RFI}) + S_I(f + f_{RFI})] \\ S_I(f) &= T_I \int_{-B_L}^{B_L} \left[\frac{\sin(\pi f T_I)}{\pi f T_I} \right]^2 df, \text{ where } T_I = 1/R_I \end{aligned} \quad , \quad (95)$$

where f_{RFI} is defined as the RFI frequency relative to the desired carrier frequency f_c .

- From Section 3.3.6, Eqn. (65), the value of $\sigma_{Threshold}$ is calculated using the following equation:

$$\sigma_{Threshold} = \left[\frac{1}{\sqrt{LSNR_{Eff}}} \right] \text{Radian} \quad , \quad (96)$$

where $LSNR_{Eff}$ is calculated from (70).

- Step 2: From Section 3.3.6, Eq. (71), using the value of $\sigma_{Tracking}$, evaluate the impacts of the carrier PLL tracking error on BER performance using the following analytical models:

$$BER_{RFI} = \frac{1}{2} \operatorname{erfc} \left\{ \frac{1}{\sigma_{Tracking}} \right\} + \sqrt{\frac{1}{\pi}} \cdot \frac{\alpha(B_L T_b)}{2} \sigma_{Tracking} e^{-\left\{ \frac{1}{\sigma_{Tracking}^2} \right\}} \quad (97)$$

where α is defined as in (69). As indicated in Figure 26, the loop-bandwidth-bit-time-product is: $B_L T_b < 0.01$.

- Step 3: Determine the threshold values of the BER_{RFI} and T_{RFI} caused by the RFI. The threshold values of the BER_{RFI} and T_{RFI} caused by the RFI are defined as $BER_{Threshold}$ and T_{ThRFI} , respectively.

- From Eq. (97), the threshold value $BER_{Threshold}$ is calculated using the following equation:

$$BER_{Threshold} = \frac{1}{2} \operatorname{erfc} \left\{ \frac{1}{\sigma_{Threshold}} \right\} + \sqrt{\frac{1}{\pi}} \cdot \frac{\alpha(B_L T_b)}{2} \sigma_{Threshold} e^{-\left\{ \frac{1}{\sigma_{Threshold}^2} \right\}} , \quad (98)$$

where $\sigma_{Threshold}$ is defined as in (96).

- The threshold of the interference time duration T_{RFI} is calculated using the following relationship:

$$T_{ThRFI} = f(\%) \cdot T_O , \quad (99)$$

where T_O is the total observation time within the ground station antenna FOV (field-of-view), and $f(\%)$ is the fraction of time that is allowed for the SATOPS data to be corrupted by the interference sources. For NASA missions, the fraction of time $f(\%)$ of 1% is usually selected, and the threshold of the interference time duration T_{RFI} is given by:

$$T_{ThRFI} = (0.01) \cdot T_O . \quad (100)$$

- Step 4: RFI is declared when BER_{RFI} and T_{RFI} exceed threshold values, i.e.,:
 - $BER_{RFI} > BER_{Threshold}$ when $\sigma_{Tracking} = \sigma_{Threshold}$ for $T_{RFI} \geq T_{ThRFI}$.
- Step 5: In conjunction with the above steps (activities), the lock detector also monitors the PLL tracking error $\sigma_{Tracking}$.
 - The loop is declared to drop lock when $\sigma_{Tracking} \geq \sigma_{Thear}$.
 - σ_{Thear} is the carrier threshold of the PLL, and it is derived from (65). Note that in practice: $\sigma_{Thear} \geq \sigma_{Threshold}$.
 - If the drop-lock duration is greater than T_{ThRFI} , then evaluate the BER.
 - RFI is declared when $BER > BER_{Threshold}$.

In practice, to ensure meeting the required command QoS and un-interrupted PLL operation, we want to set:

$$\sigma_{Thear} \geq \sigma_{Threshold} . \quad (101)$$

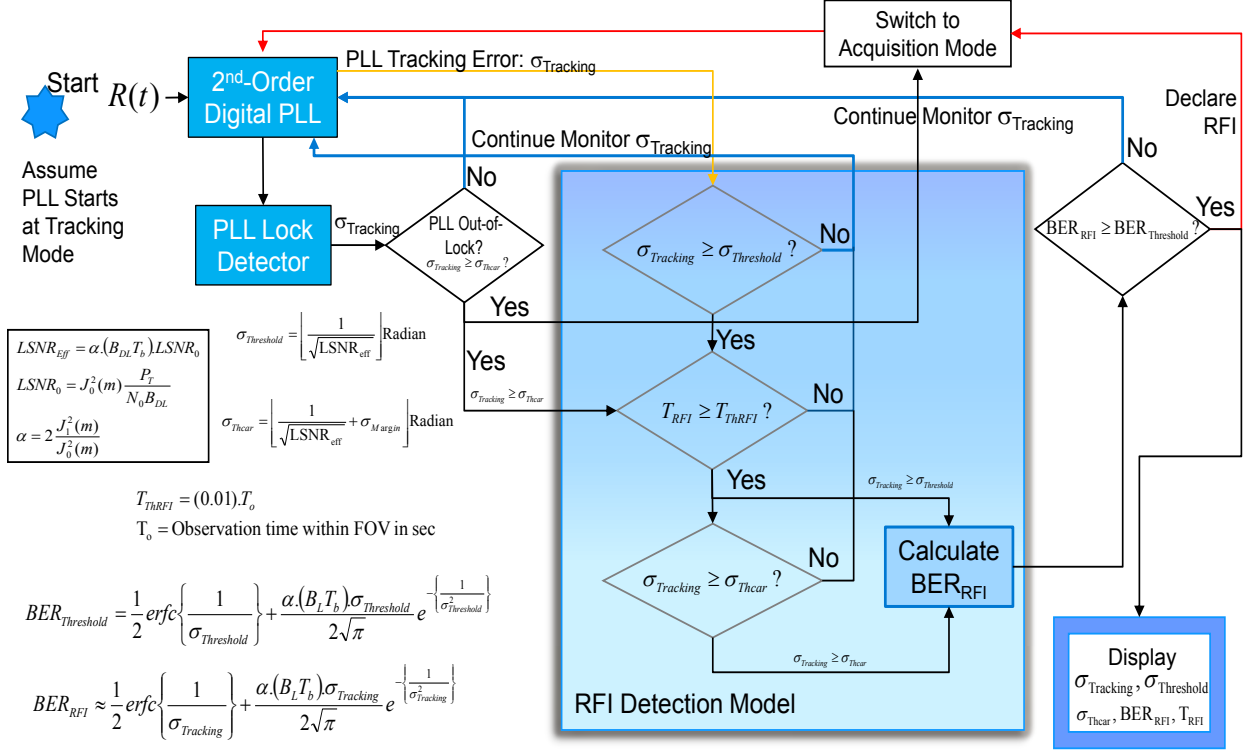


Figure 27. Proposed Framework and Algorithm for RFI Detection

3.3.9 USB Signal Estimation Models

3.3.9.1 CW RFI Case

Recall that the SATOPS command signal $S(t)$ and RFI signal $I(t)$ received at the satellite are given by:

$$S(t) = a\sqrt{2P_r} \cos(2\pi(f_c + f_d)t + md(t) \sin(2\pi f_{sc}t) + \theta_c)) \quad (102)$$

$$I(t) = \sqrt{2P_I} \cos(2\pi(f_c + \Delta f_c)t + \theta_I) \quad (103)$$

Using the identities:

$$\cos(m \sin(x)) = J_0(m) + 2 \sum_{n=1}^{\infty} J_{2n}(m) \cos(2nx) \quad (104)$$

$$\sin(m \sin(x)) = \sum_{n=1}^{\infty} 2J_{2n-1}(m) \sin((2n-1)x) \quad (105)$$

the signal $S(t)$ can be expanded as:

$$S(t) = a\sqrt{2P_T} [J_0(m)\cos(2\pi(f_c + f_d)t + \theta_c) - 2J_1(m)d(t)\sin(2\pi(f_c + f_d)t + \theta_c)\sin(2\pi f_{sc}t) + h.o.t] \quad (106)$$

$h.o.t$ = Higher order terms that contained signal components at twice of frequencies or higher

The goal here is to estimate the “carrier component” of the USB signal, i.e., to estimate the following signal:

$$S(t) = a\sqrt{2P_T}J_0(m)\cos(2\pi(f_c + f_d)t + \theta_c) \quad (107)$$

The channel gain factor, a , is calculated from the estimated a (dB) as:

$$a = 10^{\frac{\hat{a}(dB)}{10}} \quad (108)$$

The estimated channel gain factor, \hat{a} , expressed in dB is:

$$\hat{a} = 10^{\frac{\hat{a}(dB)}{10}}, \quad (109)$$

where

$$\begin{aligned} \hat{a}(dB) &= L_s(dB) + G_T(dB) + G_R(dB) + L_{Atm}(dB) + L_{CaT}(dB) + L_{CaR}(dB) \\ L_s(dB) &= \text{Space loss} = 10 \log \left[\left(\frac{c}{4\pi D f_c} \right)^2 \right] \\ G_T(dB) &= \text{Transmitter antenna gain in dB} = 10 \log \left[\frac{4\pi A_T f_c^2}{c^2} \right] \\ G_R(dB) &= \text{Receiver antenna gain in dB} = 10 \log \left[\frac{4\pi A_R f_c^2}{c^2} \right] \end{aligned} \quad (110)$$

and

$$\begin{aligned} L_{Atm}(dB) &= \text{Loss due to atmospheric in dB} \\ L_{CaT}(dB) &= \text{Loss due to transmitter's cable in dB} \\ L_{CaR}(dB) &= \text{Loss due to receiver's cable in dB} \end{aligned}$$

where

c = Speed of light in m/sec

D = The distant from ground station tracking to the satellite in meters

A_T = Transmitter antenna diameter in m^2

A_R = Receiver antenna diameter in m^2

The Doppler frequency, f_d , is estimated using the following equation:

$$\hat{f}_d = f_c \left[\frac{c + v_s}{c - v_g} - 1 \right] \quad (111)$$

where

f_c = Transmitted carrier frequency in Hz
 c = Speed of light in m/sec
 v_s = Satellite's speed in m/sec
 v_g = Ground station's speed in m/sec. It is assumed to be zero.

It should be pointed out that the channel gain, a , can also be derived from the link budget model described in Section 3.3.11.

3.3.9.2 *Estimating the Received Carrier Phase θ_e - Case 1: PLL in Tracking Mode*

For small phase tracking errors, Figure 28 illustrated the linearized model of the advanced NASA PLL shown in Figure 18. As shown in Figure 28, during tracking mode, the phase error is small and given by:

$$\theta_e(t) = \theta_c(t) - \theta_{VCO}(t), \quad (112)$$

where the VCO's phase is defined as:

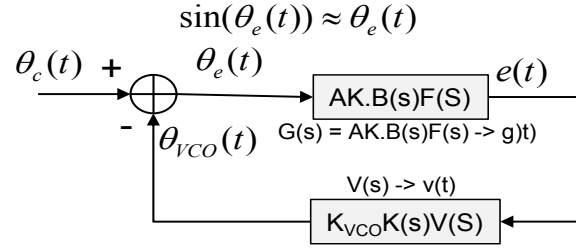
$$\theta_{VCO}(t) = 2\pi \cdot K_{VCO} \cdot \int_0^t \int_0^\infty e(\tau) v(s - \tau) d\tau ds, \quad (113)$$

where

$$e(t) = AK \cdot \int_0^\infty \theta_e(\tau) g(t - \tau) d\tau. \quad (114)$$

Figure 29 describes a mathematical framework for characterizing the estimate of carrier tracking phase error of the advanced NASA second-order PLL shown in Figure 18, and how it is used in the USB signal estimation model. Figure 30 shows where the carrier tracking phase error is incorporated in the simulation of a PLL in the presence of RFI. Simulation models for the NASA advanced second-order PLL and typical Type-I imperfect integrator second-order PLL employed by many SATOPS systems will be presented in the following sub-sections. Both CW and wide-band (WB) RFI signal types will be investigated. For Type-I imperfect integrator, discrete simulation models will be presented for implementation in Matlab. Finally, a framework to show

how these simulation models of the PLL tracking phase error will be integrated into the USB estimator model.



PLL Closed loop transfer function:

$$H_{PLL}(s) = \frac{B(s)F(s)K(s)V(s)}{1 + B(s)F(s)K(s)V(s)}$$

Figure 28. Linearized Model of Advanced NASA PLL Shown in Figure 18 for Tracking Mode

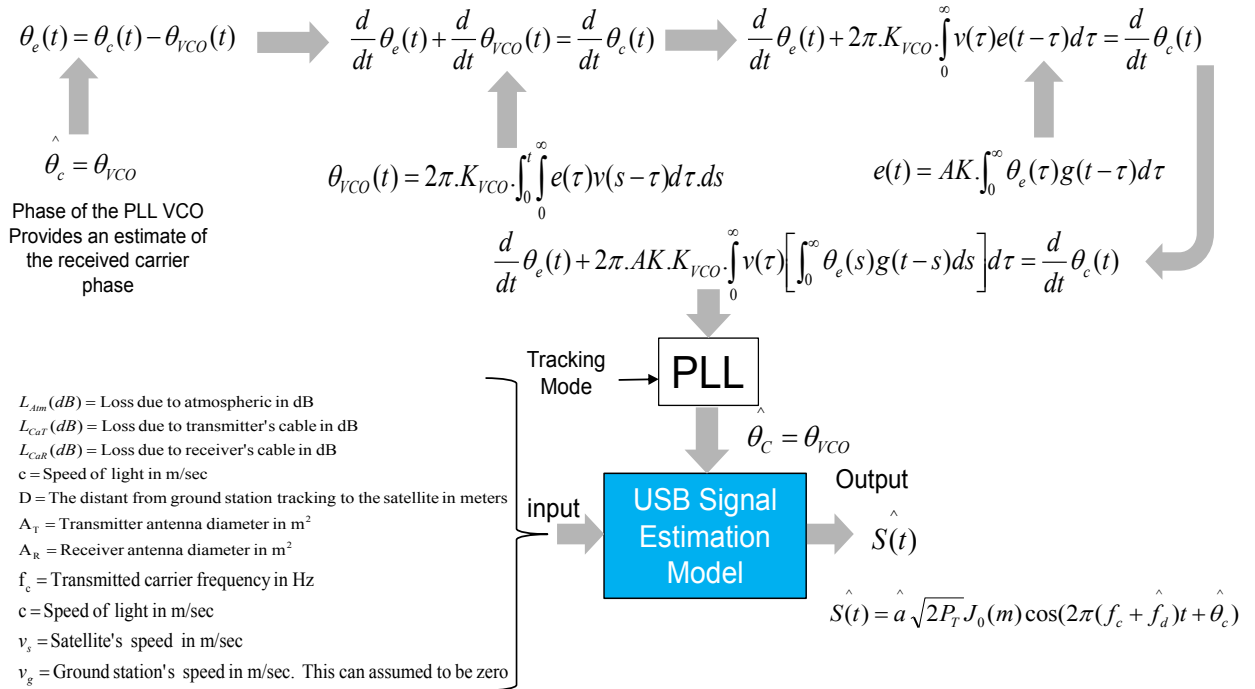


Figure 29. Mathematical Framework and Algorithm to Incorporate PLL Tracking Error into USB Signal Estimation Model

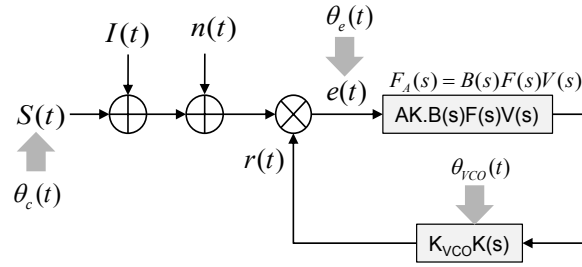


Figure 30. Simulation Model for Incorporating Carrier Tracking Error into NASA Advanced Second-Order PLL

3.3.9.3 Mathematical Model of NASA Advanced Second-Order PLL Tracking Error

3.3.9.3.1 Case 1: CWRFI

Recall from previous sections, the signals $S(t)$, $I(t)$, $n(t)$ and $r(t)$ shown in Figure 30, are defined as follow:

$$S(t) = a \sqrt{2P_T} J_0(m) \cos(2\pi(f_c + f_d)t + \theta_c) \quad (115)$$

$$I(t) = \sqrt{2P_I} \cos(2\pi(f_c + \Delta f_c)t + \theta_I), \quad (116)$$

where,

$$n(t) = \text{AWGN with two-sided powerspectral density of } N_0 / 2$$

and

$$r(t) = \sqrt{2} \sin(2\pi f_c t + \theta_{VCO}(t)) \quad (117)$$

Let's define the Heavy-side operator “ p ” as:

$$p = \frac{d}{dt}(\cdot) \quad (118)$$

For typical NASA, civil and commercial SATOPS receiver, the loop-gain and filters shown in Figure 30 are given below:

$$AK = \text{loop gain} = 2.4 \times 10^7, \quad (119)$$

$$B(s) = \frac{1}{(1 + \tau_{RC}s)}, \quad (120)$$

$$\tau_{RC} = 1.6 \times 10^{-5} . \quad (121)$$

For a Type-I imperfect integrator loop filter, $F(s)$ is given by:

$$F(s) = \frac{1 + \tau_2 s}{1 + \tau_1 s} , \quad (122)$$

where

$$\tau_1 = 4707, \tau_2 = 0.0442 \quad (123)$$

$$\tau_V = 1.0 \times 10^{-6} . \quad (124)$$

The phase smoother filter, $V(s)$, is defined as:

$$V(s) = \frac{1}{(1 + \tau_V s)} . \quad (125)$$

The VCO filter is:

$$K(s) = \frac{1}{s} . \quad (126)$$

We define the following system parameters:

$$ISR = \frac{P_I}{J_0^2(m) P_T} \quad (127)$$

$$K = AK.K_{VCO} \quad (128)$$

$$\theta_c = \theta_c(t) = \omega_0 t - \theta_0 = 2\pi f_0 t - \theta_0 \quad (129)$$

$$\theta_I(t) = 2\pi \Delta f_c t + 2\pi f_{I-OSC} t + \theta_I = 2\pi f_I t + \theta_I$$

where

$$f_I = \Delta f_c + f_{I-OSC} \quad (130)$$

$$\Delta \varpi_0 = 2\pi(f_I + f_0) \quad (131)$$

$$\Delta \theta_0 = \theta_I - \theta_0 \quad (132)$$

and

$$\theta_e(t) = \theta_c(t) - \theta_{VCO}(t) . \quad (133)$$

The carrier tracking phase error of a typical second-order PLL in the presence of RFI can be characterized by a differential equation shown below:

$$\frac{1}{KJ_0(m)\sqrt{P_T}} \frac{d}{dt} \theta_e(t) = \frac{\varpi_0}{KJ_0(m)\sqrt{P_T}} - F_A(p) \left[\sin(\theta_e(t)) + \sqrt{ISR} \sin(\theta_e(t) + \Delta \varpi_0 t + \Delta \theta_0) + \frac{1}{J_0(m)\sqrt{P_T}} n(t) \right] . \quad (134)$$

For a typical advanced NASA Type-I second-order PLL, $F_A(p)$ is given by:

$$\begin{aligned}
F_A(p) &= \left[\frac{1+\tau_2 p}{1+\tau_1 p} \right] \left[\frac{1}{1+\tau_{RC} p} \right] \left[\frac{1}{1+\tau_v p} \right] = \frac{1+\tau_2 p}{(1+\tau_1 p)(1+\tau_{RC} p)(1+\tau_v p)} \\
F_A(p) &= \frac{1+\tau_2 p}{1+\tau_1 p + \tau_{RC} p + \tau_{RC} \tau_1 p^2 + \tau_v p + \tau_1 \tau_v p^2 + \tau_{RC} \tau_v p^2 + \tau_{RC} \tau_1 \tau_v p^3} \\
F_A(p) &= \frac{1+\tau_2 p}{1+(\tau_1 + \tau_{RC} + \tau_v) p + (\tau_{RC} \tau_1 + \tau_1 \tau_v + \tau_{RC} \tau_v) p^2 + \tau_{RC} \tau_1 \tau_v p^3} \\
F_A(p) &= \frac{1+\tau_2 p}{1+\tau_{C1} p + \tau_{C2} p^2 + \tau_{C3} p^3}
\end{aligned} \tag{135}$$

where

$$\begin{aligned}
\tau_{C1} &= \tau_1 + \tau_{RC} + \tau_v \\
\tau_{C2} &= \tau_{RC} \tau_1 + \tau_1 \tau_v + \tau_{RC} \tau_v \\
\tau_{C3} &= \tau_{RC} \tau_1 \tau_v
\end{aligned} \tag{136}$$

Thus, from (135), a differential equation characterizes the behavior of the PPL tracking phase error in the presence of narrowband RFI and AWGN. It can be shown to have the following form:

$$\begin{aligned}
\frac{1}{KJ_0(m)\sqrt{P_T}} (1+\tau_{C1} p + \tau_{C2} p^2 + \tau_{C3} p^3) \frac{d}{dt} \theta_e(t) = \\
\frac{(1+\tau_{C1} p + \tau_{C2} p^2 + \tau_{C3} p^3) \varpi_0}{KJ_0(m)\sqrt{P_T}} - (1+\tau_2 p) \left[\sin(\theta_e(t)) + \sqrt{ISR} \sin(\theta_e(t) + \Delta \varpi_0 t + \Delta \theta_0) + \frac{1}{J_0(m)\sqrt{P_T}} n(t) \right]
\end{aligned} \tag{137}$$

One can rewrite the above equation and obtain the following equation:

$$\begin{aligned}
\frac{1}{KJ_0(m)\sqrt{P_T}} \left[\frac{d}{dt} \theta_e(t) + \tau_{C1} \frac{d^2}{dt^2} \theta_e(t) + \tau_{C2} \frac{d^3}{dt^3} \theta_e(t) + \tau_{C3} \frac{d^4}{dt^4} \theta_e(t) \right] = \\
- \left[\sin(\theta_e(t)) + \sqrt{ISR} \sin(\theta_e(t) + \Delta \varpi_0 t + \Delta \theta_0) + \frac{1}{J_0(m)\sqrt{P_T}} n(t) \right] \\
- \left[\frac{d}{dt} \sin(\theta_e(t)) + \sqrt{ISR} \frac{d}{dt} \sin(\theta_e(t) + \Delta \varpi_0 t + \Delta \theta_0) + \frac{1}{J_0(m)\sqrt{P_T}} \frac{d}{dt} n(t) \right]
\end{aligned} \tag{138}$$

3.3.9.3.2 Case 2: Wideband (WB) RFI

For WB RFI, recall that the interference signal has the following form:

$$I(t) = \sqrt{2P_I} d_I(t) \cos(2\pi(f_c + \Delta f_c)t + \theta_I) \tag{139}$$

From (137), the differential equation characterizes the behavior of the PPL tracking phase error in the presence of wideband RFI and AWGN. It can be shown to have the following form:

$$\begin{aligned}
& \frac{1}{KJ_0(m)\sqrt{P_T}} \left[\frac{d}{dt} \theta_e(t) + \tau_{c1} \frac{d^2}{dt^2} \theta_e(t) + \tau_{c2} \frac{d^3}{dt^3} \theta_e(t) + \tau_{c3} \frac{d^4}{dt^4} \theta_e(t) \right] = \\
& - \left[\sin(\theta_e(t)) + \sqrt{ISR} d_I(t) \sin(\theta_e(t) + \Delta\omega_0 t + \Delta\theta_0) - \frac{1}{J_0(m)\sqrt{P_T}} n(t) \right] \\
& - \left[\frac{d}{dt} \sin(\theta_e(t)) + \sqrt{ISR} d_I(t) \frac{d}{dt} \sin(\theta_e(t) + \Delta\omega_0 t + \Delta\theta_0) + \frac{1}{J_0(m)\sqrt{P_T}} \frac{d}{dt} n(t) \right] .
\end{aligned} \tag{140}$$

3.3.9.4 Discrete Simulation Model of Type I Imperfect Integrator PLL Tracking Error

This sub-section presents the simulation models for a second-order PLL using Type-I imperfect integrator. Figure 31 depicts a block diagram of this PLL.

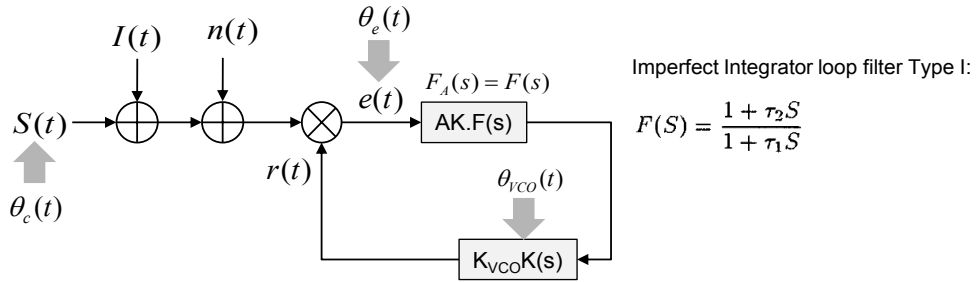


Figure 31. Simulation Model for Incorporating Carrier Tracking Error into Typical Type-I Imperfect Integrator Second-Order PLL

3.3.9.4.1 Case I: CW RFI

For Type-I imperfect integrator loop filter with the worst case CW RFI, Eq. (134) becomes:

$$\begin{aligned}
\frac{d^2}{dt^2} \theta_e(t) &= \frac{K'}{\tau_1} \left[-\sin(\theta_e(t)) - \sqrt{ISR} \sin(\theta_e(t)) - \frac{n_1(t)}{A'} \right] \\
&- \frac{1}{\tau_1} \left[1 + K' \tau_2 \cos(\theta_e(t)) + K' \tau_2 \sqrt{ISR} \cos(\theta_e(t)) \right] \frac{d}{dt} \theta_e(t) + \frac{1}{A' \tau_1} \frac{d}{dt} n_1(t) ,
\end{aligned} \tag{141}$$

where we have defined the worst case scenario when $\theta_l(t) = 0$, $\Delta\omega_0 = 0$, and $\Delta\tilde{\theta} = 0$. The parameters A' , K' and interference to signal ratio (ISR) are defined as:

$$A' = J_0(m) \sqrt{2P_T} \tag{142}$$

$$K' = \frac{K}{A'} = \frac{AK \cdot K_{VCO}}{J_0(m) \sqrt{2P_T}} \quad (143)$$

and

$$ISR = \frac{P_I}{P_T} \quad (144)$$

Note that $n_I(t)$ is the defined as:

$$n_I(t) = n_c(t) \cos(\theta_e(t)) - n_s(t) \sin(\theta_e(t)) \quad (145)$$

where $n_c(t)$ and $n_s(t)$ are the in-phase and quadrature components of the AWGN, $n(t)$. Viterbi [7] has shown that $n_I(t)$ is essentially white Gaussian noise with spectral density $N_0/2$ when the carrier loop bandwidth is smaller than the input noise bandwidth. Using, Eqn. (138) can be transformed into two first-order differential equations that are suitable for simulation using Matlab program. If we define T_s as the sampling interval and “ n ” as the number of sample points, then (138) can be rewritten as:

$$\begin{aligned} \theta_e((n+1)T_s) &= \theta_e(nT_s) + T_s \theta_e'(nT_s) \\ \theta_e'((n+1)T_s) &= \frac{T_s K'}{\tau_1} \left[-\sin(\theta_e(nT_s)) - \sqrt{ISR} \sin(\theta_e(nT_s)) - \frac{n_{1N}(nT_s)}{SNR} \right] \\ &\quad - \frac{T_s}{\tau_1} \left[1 + K' \tau_2 \cos(\theta_e(nT_s)) + K' \tau_2 \sqrt{ISR} \cos(\theta_e(nT_s)) \right] \theta_e'(nT_s) + \frac{T_s}{\tau_1 SNR} n_{1N}'(nT_s) \end{aligned} \quad (146)$$

where

$$\theta_e'(t) = \frac{d}{dt} \theta_e(t) \quad (147)$$

and

$$\theta_e'(nT_s) = \frac{\theta_e((n+1)T_s) - \theta_e(nT_s)}{T_s} \quad (148)$$

$$n_{1N}(nT_s) = \frac{n_1(nT_s)}{|n_1(nT_s)|} \quad (149)$$

When $\theta_I(t) = \theta_{I0}$, $\Delta \widetilde{\omega}_0 = 0$, and $\Delta \theta_0 = \theta_0$, Eqn. (146) becomes:

$$\begin{aligned}
\theta_e((n+1)T_s) &= \theta_e(nT_s) + T_s \theta_e'(nT_s) \\
\theta_e'((n+1)T_s) &= \frac{T_s K'}{\tau_1} \left[-\sin(\theta_e(nT_s) + \theta_0) - \sqrt{ISR} \sin(\theta_e(nT_s) + \theta_{I0}) - \frac{n_{1N}(nT_s)}{SNR} \right] \\
&\quad - \frac{T_s}{\tau_1} \left[1 + K' \tau_2 \cos(\theta_e(nT_s) + \theta_0) + K' \tau_2 \sqrt{ISR} \cos(\theta_e(nT_s) + \theta_{I0}) \right] \theta_e'(nT_s) + \frac{T_s}{\tau_1 SNR} n_{1N}'(nT_s)
\end{aligned} \tag{150}$$

3.3.9.4.2 Case 2: WB RFI

For Type-I imperfect integrator loop filter with the worst case WB (wideband) RFI, Eqn. (134) becomes:

$$\begin{aligned}
\frac{d^2}{dt^2} \theta_e(t) &= \frac{K'}{\tau_1} \left[-\sin(\theta_e(t)) - \sqrt{ISR} d_I(t) \sin(\theta_e(t)) - \frac{n_1(t)}{A'} \right] \\
&\quad - \frac{1}{\tau_1} \left[1 + K' \tau_2 \cos(\theta_e(t)) + K' \tau_2 \sqrt{ISR} d_I(t) \cos(\theta_e(t)) \right] \frac{d}{dt} \theta_e(t) + \frac{1}{A' \tau_1} \frac{d}{dt} n_1(t)
\end{aligned} \tag{151}$$

Similarly, this equation can be transformed into two first-order differential equations that are suitable for simulation using Matlab program. It is found to be:

$$\begin{aligned}
\theta_e((n+1)T_s) &= \theta_e(nT_s) + T_s \theta_e'(nT_s) \\
\theta_e'((n+1)T_s) &= \frac{T_s K'}{\tau_1} \left[-\sin(\theta_e(nT_s)) - \sqrt{ISR} d_I(nT_s) \sin(\theta_e(nT_s)) - \frac{n_{1N}(nT_s)}{SNR} \right] \\
&\quad - \frac{T_s}{\tau_1} \left[1 + K' \tau_2 \cos(\theta_e(nT_s)) + K' \tau_2 \sqrt{ISR} d_I(nT_s) \cos(\theta_e(nT_s)) \right] \theta_e'(nT_s) + \frac{T_s}{\tau_1 SNR} n_{1N}'(nT_s)
\end{aligned} \tag{152}$$

When $\theta_I(t) = \theta_{I0}$, $\Delta \widetilde{\omega}_0 = 0$, and $\Delta \theta_0 = \theta_0$, Eqn. (152) becomes:

$$\begin{aligned}
\theta_e((n+1)T_s) &= \theta_e(nT_s) + T_s \theta_e'(nT_s) \\
\theta_e'((n+1)T_s) &= \frac{T_s K'}{\tau_1} \left[-\sin(\theta_e(nT_s) + \theta_0) - \sqrt{ISR} d_I(nT_s) \sin(\theta_e(nT_s) + \theta_{I0}) - \frac{n_{1N}(nT_s)}{SNR} \right] \\
&\quad - \frac{T_s}{\tau_1} \left[1 + K' \tau_2 \cos(\theta_e(nT_s) + \theta_0) + K' \tau_2 \sqrt{ISR} d_I(nT_s) \cos(\theta_e(nT_s) + \theta_{I0}) \right] \theta_e'(nT_s) + \frac{T_s}{\tau_1 SNR} n_{1N}'(nT_s)
\end{aligned} \tag{153}$$

The characteristics of the second-order Type-I imperfect integrator employed by a typical NASA PLL is shown in Table 4. The loop parameters τ_1 and τ_2 in (145) and (149) are calculated based the PLL tracking loop bandwidth selected. Table 4 shows the values for the two-sided loop noise bandwidth, $2B_L$, two-sided pre-detection noise bandwidth, $2B_{LPD}$, normalized gain constant K' , loop parameters τ_1 and τ_2 .

Table 4. Typical Type-I Imperfect Integrator Employed By NASA PLL

Tracking Mode	$2B_L$ (Hz)	$2B_{LPD}$ (Hz)	K'	τ_1 (Sec)	τ_2 (Sec)
Narrow	1.0	200	1340.9	33940.0	1.50
	3.0	200	1340.9	6510.0	0.50
	10.0	2000	1340.7	339.4	0.15
	30.0	2000	1340.7	65.1	0.05
Wide	10.0	2000	13409.3	3394.0	0.15
	30.0	2000	13409.3	651.0	0.05
	100.0	20000	13406.7	33.9	0.015
	300.3	20000	13406.7	6.5	0.005

3.3.9.5 Lock Point and Definition of Loss of Lock of Type-I Imperfect Integrator PLL

It is assumed that the PLL is initially in lock with the phase of the desired signal, and the RFI signal is subsequently injected into the receiver. Since the Type-I imperfect integrator is of a lag-lead type filter, the PLL is a second-order loop, and consequently only one stable point in the phase error region of $(-\pi, +\pi)$. In this same region, there also exists a single saddle point. Thus, using the same argument in, the selected threshold for determining the loss of lock of a PLL is $\pi/2$. This threshold will be used in analyzing the loss of lock of a PLL using Type-I imperfect integrator.

Eqn. (150) is simulated in Matlab and the results are presented in Figure 32, Figure 33, and Figure 34. These figures show the simulation of the second-order Type-I imperfect integrator PLL with SNR = 16 dB, ISR = -15 dB, and initial phase offset θ_0 between the desired signal and the reference VCO phase is set at $\pi/4$ radians. Figure 32 shows the tracking jitter settled down to $\pi/4$ as expected. Figure 33 shows the difference of tracking error fluctuates around 0 radians, and Figure 34 shows the PLL's VCO phase starts at 0 degrees and it eventually locks onto the incoming phase at $\pi/4$ radians. When the initial phase offset, θ_0 , between the desired signal and the reference VCO phase is set at 0 rad, and the phase offset between the RFI signal and the reference VCO phase is set at $\pi/18$ rad, Figure 35 shows that the PLL drops lock on the desired signal phase at 0 degree, and it eventually locks on to the incoming RFI phase at $\pi/18$ radians.

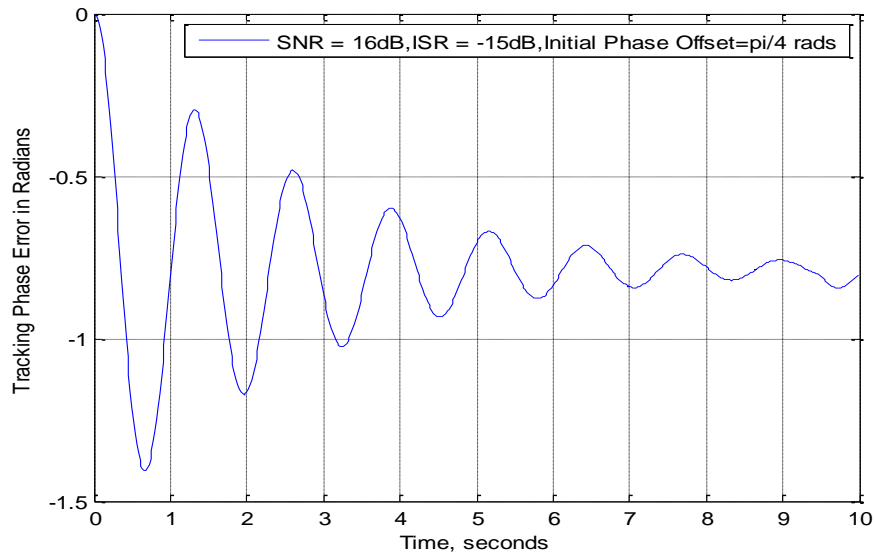


Figure 32. Tracking Phase Error as a Function of Time

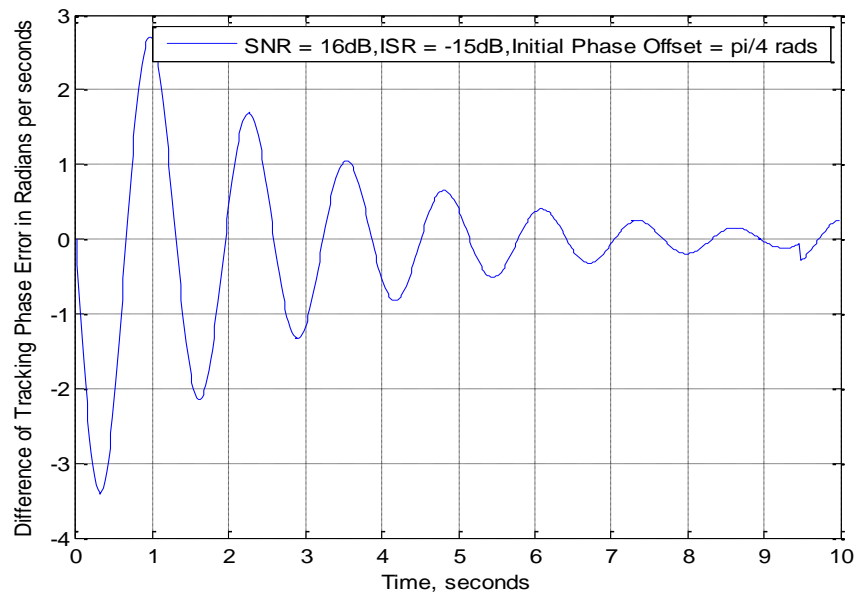


Figure 33. Difference of Tracking Error as a function of Time

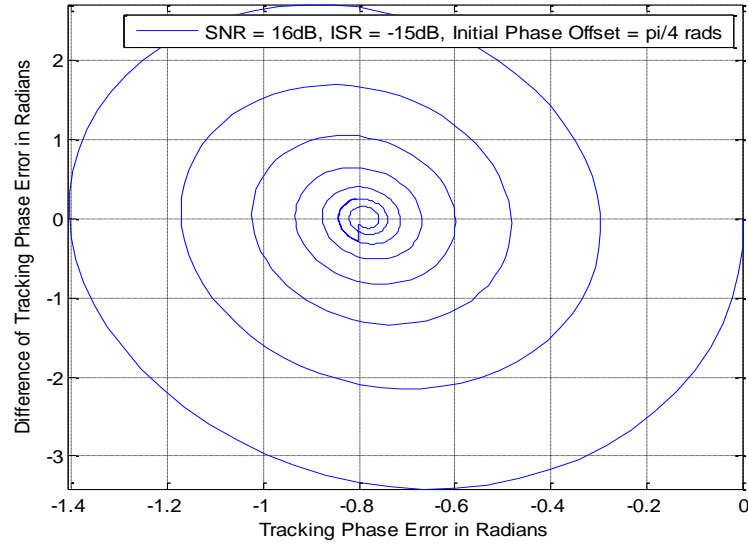


Figure 34. Phase Plane Plot for a Typical PLL Using Type-I Imperfect Integrator for ISR = -15 dB

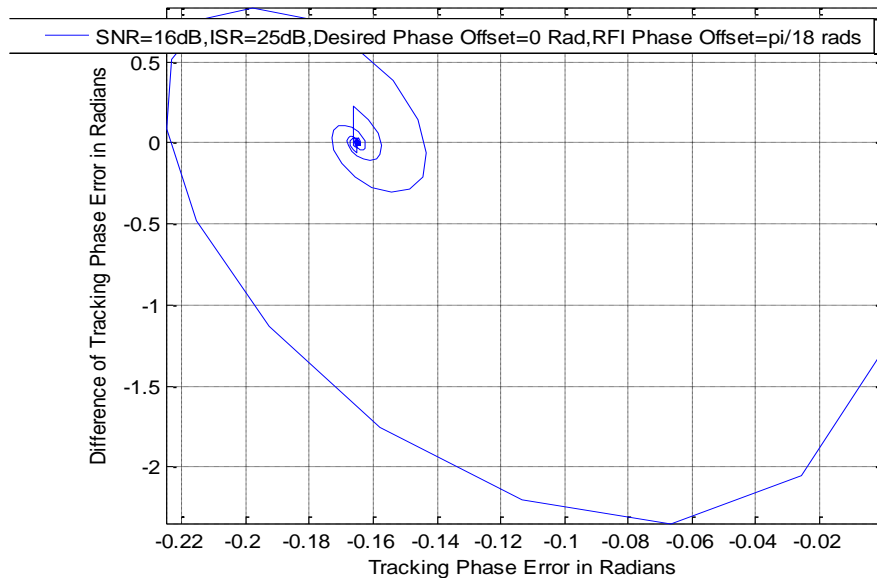


Figure 35. Phase Plane Plot for a Typical PLL Using Type-I Imperfect Integrator for ISR = 25 dB

3.3.9.6 USB Carrier Signal Component Estimator

Figure 36 shows how to incorporate the simulation models for the carrier phase error, described by equations (137), (139), (145), and (149), into the USB carrier estimator model to generate an estimate of the received SATOPS command signal, $\hat{S}(t)$.

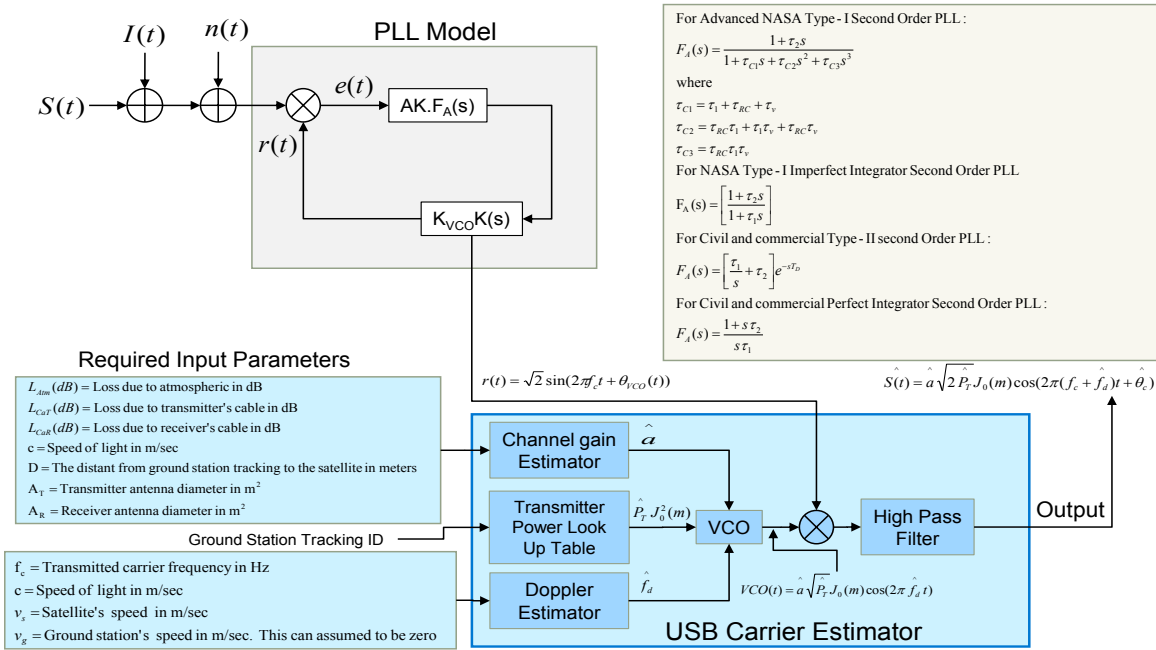


Figure 36. Block Diagram of the USB Carrier Signal Component Estimator

3.3.10 RFI Signal Estimation and Prediction Models

3.3.10.1 Case 1: CW RFI Signal Estimation and Prediction Model

This section describes the CW RFI prediction models using the USB carrier signal component estimator presented previously. Figure 37 presents a high-level block diagram for extracting the CW RFI signal from the received signal, $R(t)$. Recall the received signal at the SATOPS satellite is:

$$R(t) = S(t) + I(t) + n(t)$$

$$S(t) = a \sqrt{2P_T} J_0(m) \cos(2\pi(f_c + f_d)t + \theta_c) \quad (154)$$

$$I(t) = \sqrt{2P_I} \cos(2\pi(f_c + \Delta f_c)t + \theta_I) , \quad (155)$$

where

$n(t)$ = AWGN with two-sided power spectral density of $N_0 / 2$.

In Figure 37, $R_I(t)$ is defined as the estimate of the CW RFI signal at RF frequency in the presence of noise and error signal caused by inaccurate estimate of the USB carrier signal, i.e.,

$$R_I(t) = I(t) + n(t) + \varepsilon(t)$$

where $\varepsilon(t)$ is the error signal caused by inaccurate carrier signal estimator due to RFI

$$\varepsilon(t) = S(t) - \hat{S}(t) = a \sqrt{2P_T} J_0(m) \cos(2\pi(f_c + f_d)t + \theta_c) - \hat{a} \sqrt{2P_T} J_0(m) \cos(2\pi(\hat{f}_c + \hat{f}_d)t + \hat{\theta}_c) . \quad (156)$$

Due to the RFI, the PLL may not provide an accurate estimate of the incoming carrier phase signal. However, in practice, one knows the transmitted power, and can estimate the Doppler frequency and channel gain factor fairly accurate, thus without loss of generality one can set:

$$a = \hat{a} = \sqrt{\frac{\hat{P}_R}{P_T}}; f_d = \hat{f}_d \quad (157)$$

The error signal becomes:

$$\varepsilon(t) = \sqrt{2\hat{P}_R} J_0(m) \left[\cos(2\pi(f_c + \hat{f}_d)t + \theta_c) - \cos(2\pi(\hat{f}_c + \hat{f}_d)t + \hat{\theta}_c) \right] . \quad (158)$$

Rewriting the error signal, one gets:

$$\varepsilon(t) = -2\sqrt{2\hat{P}_R} J_0(m) \left[\sin(2\pi(f_c + \hat{f}_d)t + (\frac{\theta_c + \hat{\theta}_c}{2})) \sin\left[\left(\frac{\theta_c - \hat{\theta}_c}{2}\right)\right] \right] . \quad (159)$$

Down-converting the received signal, $R_I(t)$, signal to baseband signal, $R_{IBB}(t)$, one obtains:

$$R_{IBB}(t) = \left| R_I(t) \cdot 2 \cos(2\pi(f_c + \hat{f}_d)t \right|_{LPF} = \sqrt{2P_I} \cos(2\pi\Delta f_I t + \theta_I) - \sqrt{2\hat{P}_R} J_0(m) [\sin(\theta_e^+) \sin(\theta_e^-)] + N'(t) , \quad (160)$$

where

$$\Delta f_I = \Delta f_c - \hat{f}_d$$

$$\theta_e^+ = \frac{\theta_c + \hat{\theta}_c}{2}$$

$$\theta_e^- = \frac{\theta_c - \hat{\theta}_c}{2} \quad (161)$$

and

$$N'(t) = \sqrt{2N_0} \cdot N(t) , \quad (162)$$

where $N(t)$ is the normalized AWGN with zero-mean and unit variance. For small tracking error, one can approximate (160) as follows:

$$R_{IBB}(t) \approx \sqrt{2P_I} \cos(2\pi\Delta f_I t + \theta_I) - \left(\frac{\sqrt{2P_R} J_0(m)}{2} \right) \Theta_c(t) + N'(t) , \quad (163)$$

where, for small PLL carrier phase tracking jitter, one can write:

$$\Theta_c(t) = [\sin(\theta_e^+) \sin(\theta_e^-)] \approx \theta_e(t) \cdot \sin(\theta_c) ; \theta_c < \frac{\pi}{2} . \quad (164)$$

Here, one has assumed that θ_c is a constant phase offset between the desired signal and the PLL VCO's phase, and that the PLL phase tracking error is small, such that $\theta_e = \theta_c - \hat{\theta}_c \ll 0$ and $\theta_c \approx \hat{\theta}_c$.

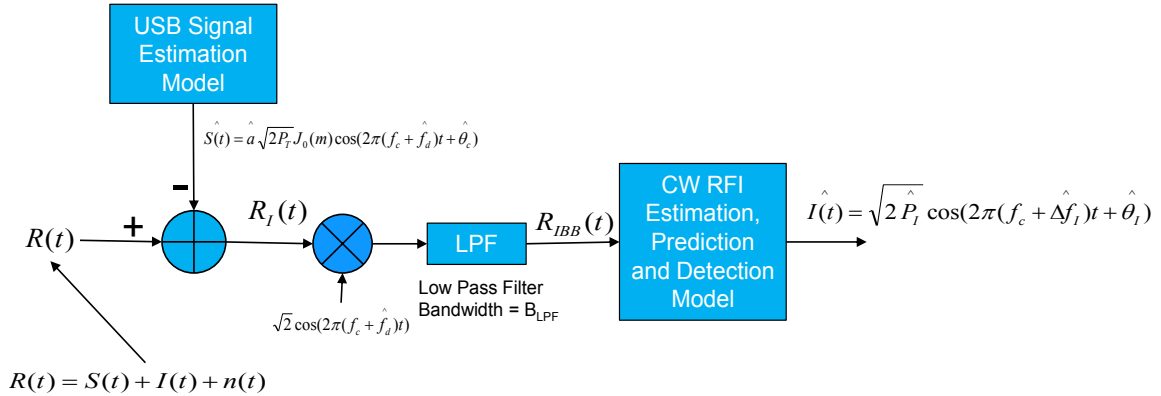


Figure 37. Block Diagram for Extracting the CW RFI Signal from the Received Signal, $R(t)$

Figure 38 presents a proposed approach for CW RFI estimation, prediction and detection model. The proposed approach estimates the CW RFI signal power first and uses its estimate for estimating the CW RFI frequency. The estimated CW RFI frequency, along with the estimated CW RFI power, is then used for the CW RFI phase estimation and detection. The details of these steps will be described in the following sections.

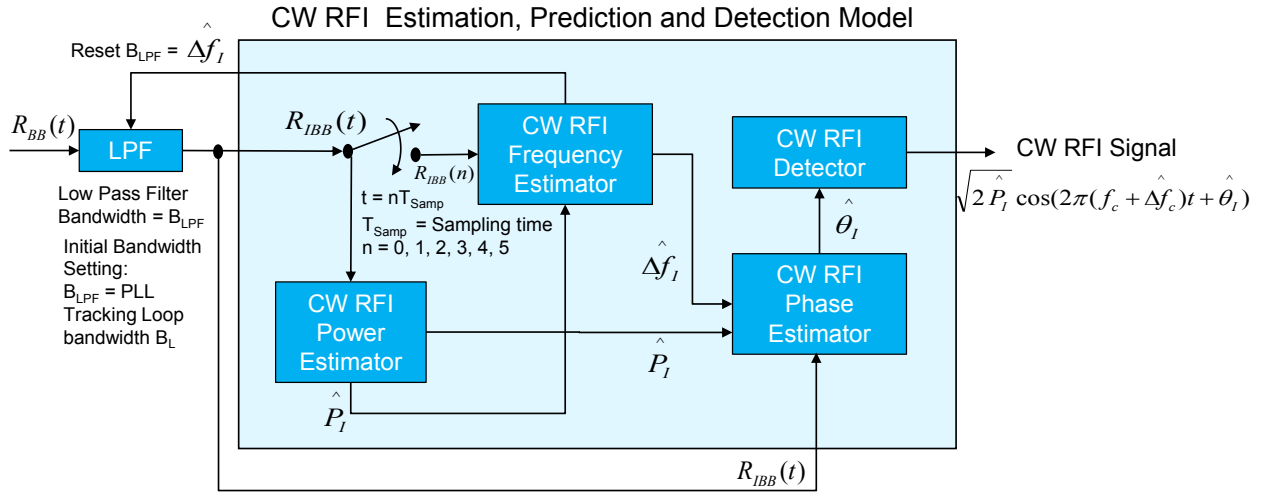


Figure 38. Block Diagram for CW RFI Estimation, Prediction and Detection Model

Before getting into the detailed discussion of the CW RFI estimation, prediction and detection models, it is noted that from (160), one observes that if the CW RFI frequency can be estimated accurately, then the 3-dB cutoff bandwidth of the LPF is set exactly at Δf_I such that the CW RFI signal is passed through it without distortion. If the 3-dB cutoff bandwidth of the LPF is not known, the LPF's bandwidth is set larger than the RFI frequency, Δf_I . Then, more noise is allowed to pass through the filter, causing performance degradation in the “CW RFI estimation, prediction and detection” model. The proposed approach to resolve this problem is described as follow:

- **Step 1:** Set the initial LPF's bandwidth $BW_{LPF} = B_L$ (PLL tracking loop bandwidth). Note that in order to cause potential interference to SATOPS receiver, the RFI frequency Δf_I , must be less than the PLL tracking loop bandwidth.
- **Step 2:** Perform the CW RFI signal power and frequency estimations to obtain the initial estimate of the CW RFI signal power and frequency.
- **Step 3:** Use the estimate of the CW RFI signal frequency to reset LPF's bandwidth BW_{LPF} .

- Step 4: One can repeat Steps 2 and 3 until the estimate of the CW RFI frequency Δf_I settles to a constant frequency and uses that frequency to set the LPF's bandwidth BW_{LPF} .

3.3.10.1.1 Estimating the CW RFI Signal Power

A combined CW RFI signal power estimator and the RFI signal power-to-noise power ratio estimator (INR) is shown in Figure 39. The proposed approach shown in Figure 39 has assumed the signal properties do not change during the observation time. It calculates the average power of all points received since the last reset. When signal properties change during the observation time, the sliding-block discussed in Ref. [8] would be used to estimate the CW RFI signal power.

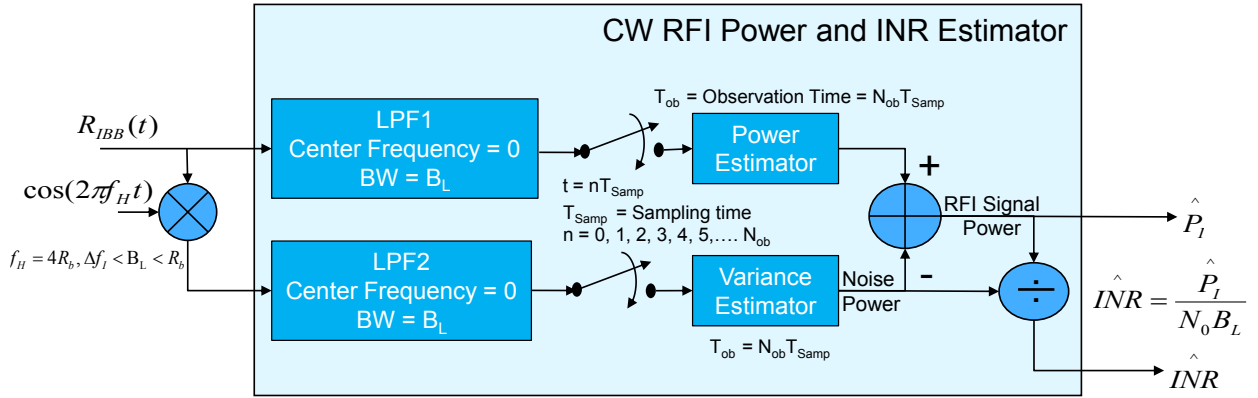


Figure 39. Block Diagram for CW RFI Signal Power Estimation

If one defines the carrier signal power-to-noise power spectral density ratio, CSNR, interference signal power-to-carrier signal power ratio, ICSR, and the normalized baseband signal $R_{IBB}(t)$, $R_{IBBN}(t)$ as, respectively:

$$CSNR = \frac{\hat{P}_R J_0^2(m)}{N_0 B_{LPF}}, \quad (165)$$

where the B_{LPF} is initially set at B_L . As described above, the optimum setting of B_{LPF} happens when it approaches the true value of the CW RFI signal frequency:

$$ICSR = \frac{P_I}{\hat{P}_R J_0^2(m)} \quad (166)$$

$$R_{IBBN}(t) = \frac{R_{IBB}(t)}{\sqrt{2P_R J_0(m)}} \quad (167)$$

Eqn. (163) can be rewritten in terms of CSNR and ICSR as follows:

$$R_{IBB}(t) \approx \sqrt{2P_R J_0(m)} \left[\sqrt{ICSR} \cdot \cos(2\pi\Delta f_I t + \theta_I) - \left(\frac{1}{2}\right) \Theta_c(t) + \frac{N(t)}{\sqrt{2CSNR}} \right] \quad (168)$$

or

$$R_{IBBN}(t) \approx \sqrt{ICSR} \cdot \cos(2\pi\Delta f_I t + \theta_I) - \left(\frac{1}{2}\right) \Theta_c(t) + \frac{N(t)}{\sqrt{2CSNR}}$$

Note that in (165), B_{LPF} is defined as the bandwidth of the LPF that is dependent on the RFI CW signal frequency. As mentioned above, the initial LPF bandwidth will be set at the PLL tracking bandwidth B_L .

The unknown power P_I of the CW RFI can be estimated by using power estimator or by taking the expected value of the square of the baseband signal $R_{IBBN}(t)$, (168). From Figure 39, the output of the power estimator is found to be:

$$E[(R_{IBBN}(t))^2] \approx E \left[\sqrt{ICSR} [\cos(2\pi\Delta f_I t + \theta_I)] - \left(\frac{1}{2}\right) [\Theta_c(t)] + \frac{[N(t)]}{\sqrt{2CSNR}} \right]^2 \quad (169)$$

$$E[(R_{IBBN}(t))^2] \approx ICSR \cdot E[\cos(2\pi\Delta f_I t + \theta_I)]^2 + \left(\frac{1}{4}\right) E[\Theta_c(t)]^2 + \frac{E[N(t)]^2}{2CSNR} \quad (170)$$

Here

$$E[\cos(2\pi\Delta f_I t + \theta_I)]^2 = \frac{1}{2} \quad (171)$$

$$E[\Theta_c(t)]^2 = \sigma_{\theta_c}^2 [\sin(\theta_c)]^2 \quad (172)$$

and

$$E[N(t)]^2 = 1 \quad (173)$$

Note that we have assumed that θ_c is a constant phase offset between the desired signal and the PLL VCO's phase. Hence $\sin(\theta_c)$ is a constant between 0 and 1. Similarly, from Figure 39, the output of the variance estimator is found to be:

$$Var \left[\left(R_{IBBN}(t) \cdot \cos(2\pi\Delta f_I t) \right) \right]_{LPF} \approx \left(\frac{1}{4} \right) \sigma_{\theta_c}^2 [\sin(\theta_c)]^2 + \frac{1}{2CSNR} \quad (174)$$

The estimate of the CW RFI power is given by, from Figure 39:

$$\hat{P}_I = \left[2\hat{P}_R J_0^2(m) \right] E \left[(R_{IBBN}(t))^2 \right] - Var \left[(R_{IBBN}(t) \cdot \cos(2\pi f_H t))^2 \right]_{L_{PF}} = P_I \quad (175)$$

As shown in Figure 39, the sampling frequency is F_{Samp} and the observation time T_{ob} in seconds is defined as:

$$T_{Ob} = N_{ob} T_{Samp} = \frac{N_{ob}}{F_{Samp}}, \quad (176)$$

where N_{ob} is the number of samples during the observation time. The performance of the CW RFI signal power described in (175) is given by:

$$Var(\hat{P}_I) = \frac{2\hat{P}_R J_0^2(m)}{N_{ob}} \left[\left(\frac{1}{4} \right) \cdot \sigma_{\theta_c}^2 \cdot [\sin(\theta_c)]^2 + \frac{1}{2CSNR} \right] = \frac{[N_o B_L]}{N_{ob}} \left[1 + \frac{\Delta_{cw}}{2} [\sin(\theta_c)]^2 \right] \quad (177)$$

Note that the factor is calculated using (79).

3.3.10.1.2 Estimating the CW RFI Signal Frequency

Since the CW RFI frequency is unknown, the proposed approach here is to estimate the RFI frequency before detection. Using (168), the normalized input signal of $R_{IBBN}(t)$ to the “CW RFI Frequency Estimator” shown in Figure 38 can be approximated as, taking into account of the CW RFI power estimate:

$$R_{IBBN}(t) \approx \sqrt{2\hat{P}_I} \cdot \cos(2\pi \Delta f_I t + \theta_I) + N_{IBBN}(t), \quad (178)$$

where the frequency, Δf_I , and phase, θ_I , of the CW RFI are unknown, and

$$N_{IBBN}(t) = \sqrt{2\hat{P}_R J_0^2(m)} \left[\frac{N(t)}{\sqrt{2CSNR}} - \left(\frac{1}{2} \right) \cdot \sin(\theta_c) \cdot \theta_e(t) \right], \theta_c < \frac{\pi}{2} \quad (179)$$

$N_{IBBN}(t)$ can be characterized as AWGN with zero-mean and variance is given by:

$$Var[N_{IBBN}(t)] = \sigma_{IBBN}^2 = 2\hat{P}_R J_0^2(m) \left[\frac{1}{4} \sin^2(\theta_c) \cdot \sigma_{\theta_e}^2 + \frac{1}{2CSNR} \right]; \theta_c < \frac{\pi}{2} \quad (180)$$

Note that the CSNR for this case is: $CSNR = \frac{\hat{P}_R J_0^2(m)}{N_o B_{L_{PF}}} \Big|_{B_{L_{PF}} = B_L} = \frac{\hat{P}_R J_0^2(m)}{N_o B_L}$. Therefore, the

interference signal-to-noise power ratio (ISNR) is given by:

$$ISNR = \frac{\hat{P}_I}{\sigma_{IBBN}^2} = \frac{\hat{P}_I}{N_0 B_L \left[1 + \frac{\Delta_{CW}}{2} \sin^2(\theta_C) \right]} \quad (181)$$

This subsection presents an approach to estimate the CW RFI frequency, Δf_I , at low ISNR using iterative weighted phase averaging (iWPA) [9]. From Figure 39, the sampled signal $R_{BBN}(n)$ is given by:

$$R_{BBN}(n) = \sqrt{2\hat{P}_I} \cdot \cos(2\pi f_0 n + \theta_I) + N_{IBBN}(n) \quad (182)$$

The corresponding unknown analog frequency Δf_I that is being estimated can be obtained from the following relationship:

$$\Delta f_I = \frac{f_0}{T_{Samp}} = F_{Samp} f_0 \quad (183)$$

where F_{Samp} is the sampling frequency that is defined as in (176). The discrete frequency f_0 is being estimated and can be written as:

$$f_0 = \frac{(L + \Delta)}{N_{ob}} = \frac{\lambda_0}{N_{ob}}, \quad -\frac{1}{2} \leq \Delta \leq \frac{1}{2} \quad (184)$$

where N_{ob} is related to the observation time, T_{Ob} , which is defined as in (176), L is the integer part, and Δ is the fractional part of λ_0 , where λ_0 denotes the number of signal cycles contained in the observation window. To understand the above notations, suppose that one observes a CW RFI signal of frequency 32.5 Hz, i.e., $\Delta f_I = 32.5$ Hz, that is sampled at 128 Hz during 1 second ($N = 128$ samples). Then, $f_0 = 32.5/128$. In this case, $\lambda_0 = 32.5$ (the frequency cycles), $L = 32$, and $\Delta = 0.5$.

Using the above notations, the Discrete Fourier Transform (DFT), $X(k)$, of $R_{BBN}(n)$ at spectral line k is given by, assuming the noise term is negligible:

$$X(k) = \frac{\sqrt{2\hat{P}_I}}{2} e^{j\theta_I} W\left(\left(\frac{k - \lambda_0}{N_{ob}}\right)\right) + \frac{\sqrt{2\hat{P}_I}}{2} e^{-j\theta_I} W\left(\left(\frac{k + \lambda_0}{N_{ob}}\right)\right) \quad (185)$$

where $W(f)$ is the Fourier transform of the selected time-domain window. For instance, considering a rectangular window of length N , we have:

$$W(f) = \frac{\sin(N_{ob}\pi f)}{\sin(\pi f)} e^{-j\pi f(N_{ob}-1)} \quad (186)$$

Since the frequency Δf_l of the CW RFI is far from the origin, $f=0$, such that the leakage coming from the negative part of the spectrum can be neglected, i.e.,

$$X(k) = \frac{\sqrt{2\hat{P}_l}}{2} e^{j\theta_l} W\left(\left(\frac{k-\lambda_0}{N_{ob}}\right)\right) \quad (187)$$

The coarse estimate of the CW RFI frequency is performed by selecting its largest peak, i.e.,

$$\hat{f}_0^{coarse} = \text{Max}\left[\frac{\arg(|X(k)|)}{N_{ob}}\right] = \frac{L}{N_{ob}} \quad (188)$$

The fine estimate of the CW RFI frequency is performed by estimating the fractional part Δ of λ_0 using iWPA [9]. The DFT signal $X(k)$ is divided into M non-overlapping segments of length P :

$$R_{lBB}^l(n) = R_{lBB}^l(n + lP), 0 \leq n \leq P-1 \quad (189)$$

The spectrum of each segment is evaluated at the previously estimated f_0 :

$$X_l(\hat{f}_0) = \sum_{n=0}^{P-1} R_{lBB}^l(n) e^{-j2\pi \hat{f}_0(n+lP)} \quad (190)$$

Substituting (182), assuming that the noise term is negligible and rectangular window, and taking into account that $\hat{f}_0 = (N_{ob} - \Delta)/N_{ob}$, one can show that:

$$X_l(\hat{f}_0) = \frac{\sqrt{2\hat{P}_l}}{2} \left[\frac{\sin(\pi\Delta P / N_{ob})}{\sin(\pi\Delta / N_{ob})} \right] e^{j\theta_l} e^{-j(2\pi\Delta P / N_{ob})(1+l)} \quad (191)$$

The phase of $X_l(\hat{f}_0)$ is given by:

$$\arg\left(X_l(\hat{f}_0)\right) = \theta_l - \frac{2\pi\Delta P}{N_{ob}}(1+l) \quad (192)$$

The frequency error can be estimated by:

$$\hat{\Delta} = \frac{N_{ob}}{2\pi L} \left[\arg\left(X_1(\hat{f}_0)\right) - \arg\left(X_2(\hat{f}_0)\right) \right] \quad (193)$$

In the above equation, we have split the original register into two segments ($P = N/2$). The fine frequency estimator is obtained using the following relationship:

$$\hat{f}_0^{fine} = \frac{L + \hat{\Delta}}{N_{ob}} \quad (194)$$

The block diagram for CW RFI frequency estimation is shown in Figure 40. The frequency estimator described above approaches the Cramer-Rao lower bound at high SNRs, which is the lowest variance that can be attained by any unbiased estimator. At high ISNR, the variance of the above frequency estimator can be approximated as:

$$\text{var}\left(\hat{f}_0^{fine}\right) \approx \left[\frac{12[N_o B_L]}{2\pi \hat{P}_I N_{ob} (N_{ob}^2 - 1)} \right] \left[1 + \frac{\Delta_{cw}}{2} [\sin(\theta_c)]^2 \right] \quad (195)$$

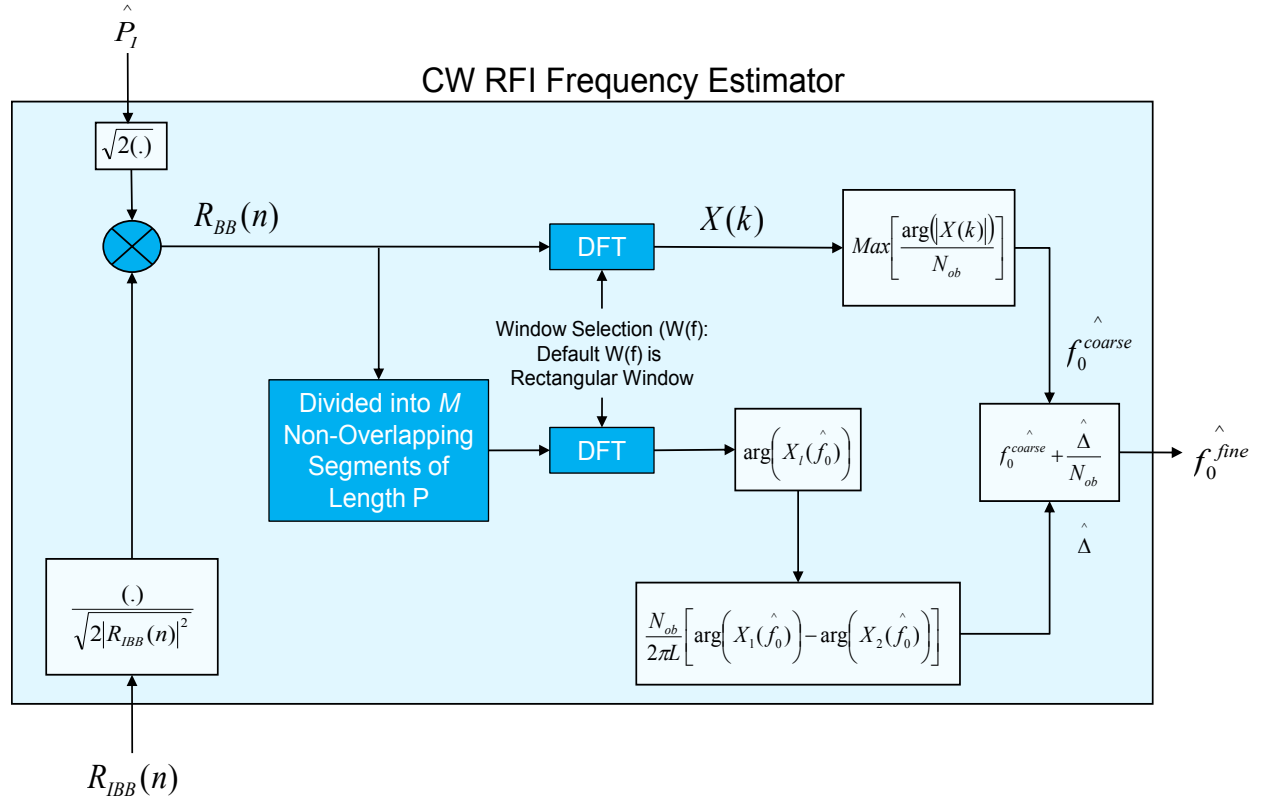


Figure 40. Block Diagram for CW RFI Frequency Estimation

3.3.10.1.3 Estimating the CW RFI Signal Phase and Detecting the CW RFI Signal

This subsection describes a Maximum Likelihood CW RFI phase estimator and CW RFI signal detector based on the approach presented in [10]. Figure 41 illustrates the proposed approach by incorporating the CW RFI power and frequency estimates. From Figure 41, the objective of the CW RFI phase estimator is to estimate the phase of the following CW RFI signal by incorporating the power and frequency estimates:

$$R_B(t) \approx \sqrt{2\hat{P}_I} \cdot \cos(2\pi \hat{\Delta f}_I t + \theta_I) + N_{IBBN}(t), \quad (196)$$

where the phase, θ_I , of the CW RFI are unknown, and the noise term $N_{IBBN}(t)$ is defined as in (179). It can be characterized as AWGN with zero-mean and variance as defined as in (180).

Note that (180) can be rewritten as:

$$\sigma_{IBBN}^2 = \text{Var}[N_{IBBN}(t)] = [N_0 B_L] \left[1 + \frac{\Delta_{CW}}{2} \sin^2(\theta_c) \right]; \theta_c < \frac{\pi}{2}. \quad (197)$$

The CW RFI phase estimator described in Figure 41 can be implemented in digital domain using a sampling frequency of F_{samp} and an observation time T_{Ob} in seconds. The T_{Ob} is defined as in (176). For this case, since the CW RFI frequency must be within the PLL tracking loop bandwidth B_L , the sampling frequency must be sampled at the Nyquist rate, i.e.,

$$F_{\text{samp}} = 2B_L, \quad (198)$$

$$T_{\text{Ob}} = \frac{N_{\text{ob}}}{2B_L}. \quad (199)$$

Again, N_{ob} is the number of samples during the observation time.

At high ISNR, the performance of the CW RFI phase estimator shown in Figure 41 approaches Cramer-Rao lower bound, which can be shown to have the following form:

$$\text{var}\left(\hat{\theta}_I\right) \approx \frac{\sigma_{IBBN}^2 \left[12n_0^2 N_{\text{ob}} + 12n_0 N_{\text{ob}}(N_{\text{ob}} - 1) + 2N_{\text{ob}}(N_{\text{ob}} - 1)(2N_{\text{ob}} - 1) \right]}{\hat{P}_I N_{\text{ob}}^2 (N_{\text{ob}}^2 - 1)}, \quad (200)$$

where n_0 is the time t_0 at which the first sample is taken for the estimate of the CW RFI phase.

Here t_0 is defined as:

$$t_0 = n_0 T_{\text{samp}} = \frac{n_0}{2B_L}. \quad (201)$$

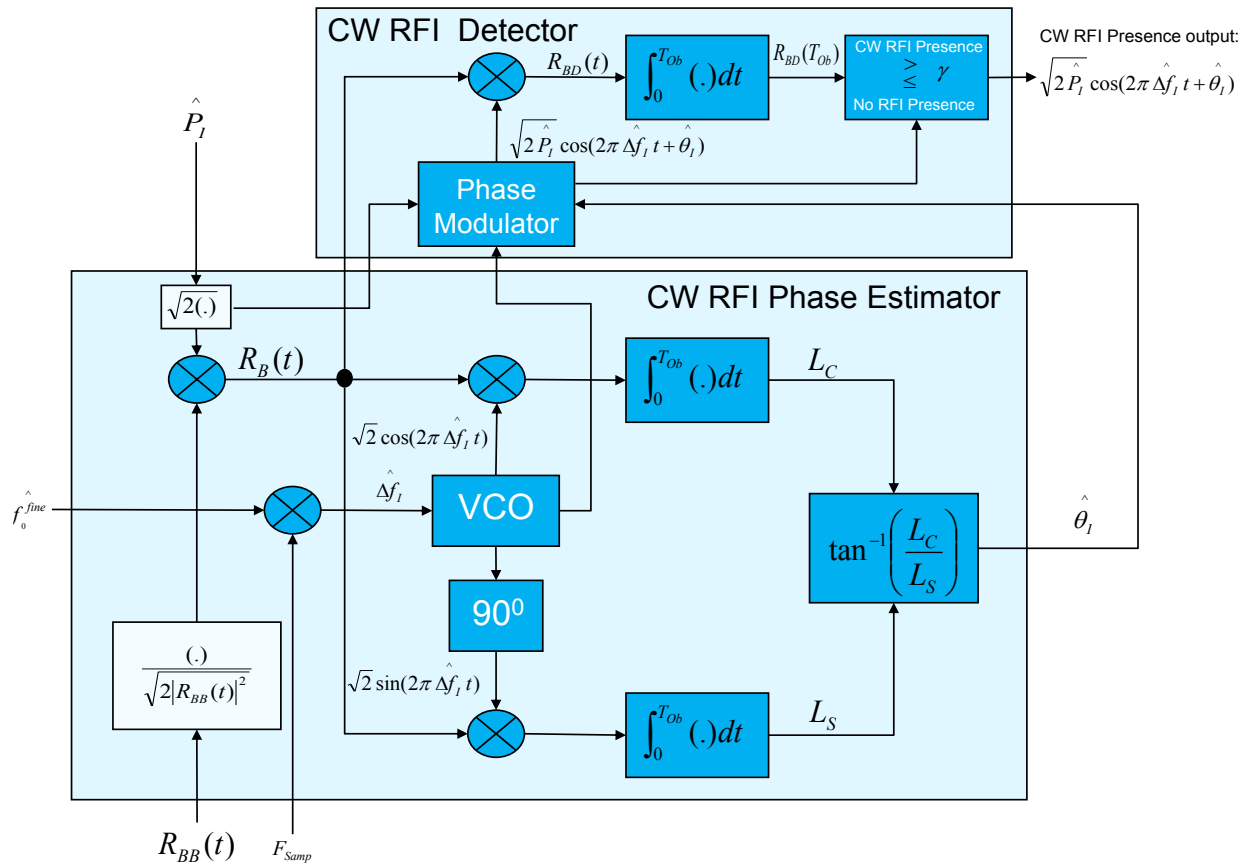


Figure 41. Block Diagram for CW RFI Phase Estimation and RFI Detection

From [10], the false alarm probability as a function of the threshold detection value, γ , can be shown to have the following form:

$$P_F = e^{-\frac{\gamma}{2\sigma_{IBBN}^2}} \quad (202)$$

Solving (198) for the threshold value:

$$\gamma = -2\sigma_{IBBN}^2 \ln[P_F] \quad (203)$$

where σ_{IBBN}^2 is given by (197). Similarly, the probability of detection as a function of the threshold detection value, γ , can be shown to have the following form [10]:

$$P_D = Q\left(\text{ISNR}, \sqrt{\frac{\gamma}{\sigma_{IBBN}^2}} \right) \quad (204)$$

where ISNR is defined as in (181), and $Q(a, b)$ is the Marcum Q-function defined by:

$$Q(a, b) = \int_b^{\infty} z e^{\left(\frac{z^2 + a^2}{2} \right)} I_0(az) dz \quad (205)$$

By combining (198) and (199), one obtains the receiver operating characteristic (ROC) given by:

$$P_D(\gamma) = Q\left(\text{ISNR}, \sqrt{-2 \ln(P_F)}\right) \quad (206)$$

Plot of Eq. (202) is shown in Figure 42 with the detection interference SNR (ISNR) as a parameter. For a given false alarm, the threshold detection value γ is chosen, using (203), to achieve the desired probability of detection at a given ISNR.

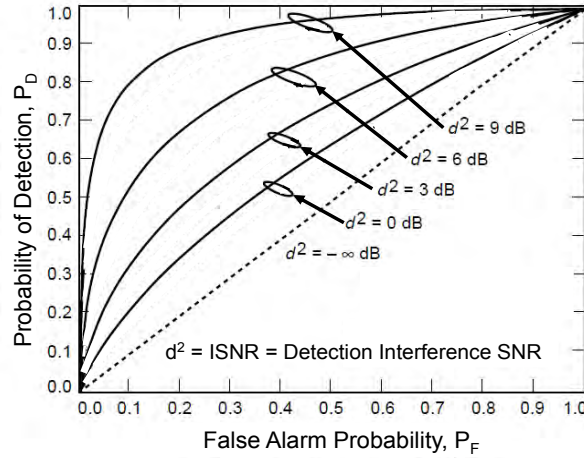


Figure 42. Receiver Operating Curve for the CW RFI Signal Detector Shown in Figure 41

3.3.10.2 Case 2: WB RFI Signal Estimation and Prediction Model

This section describes the WB RFI prediction models using the USB carrier signal component estimator presented in the previous section. Similar to the CW RFI case shown in Figure 37, Figure 43 shows a high-level block diagram for extracting the WB RFI signal from the received signal, $R(t)$.

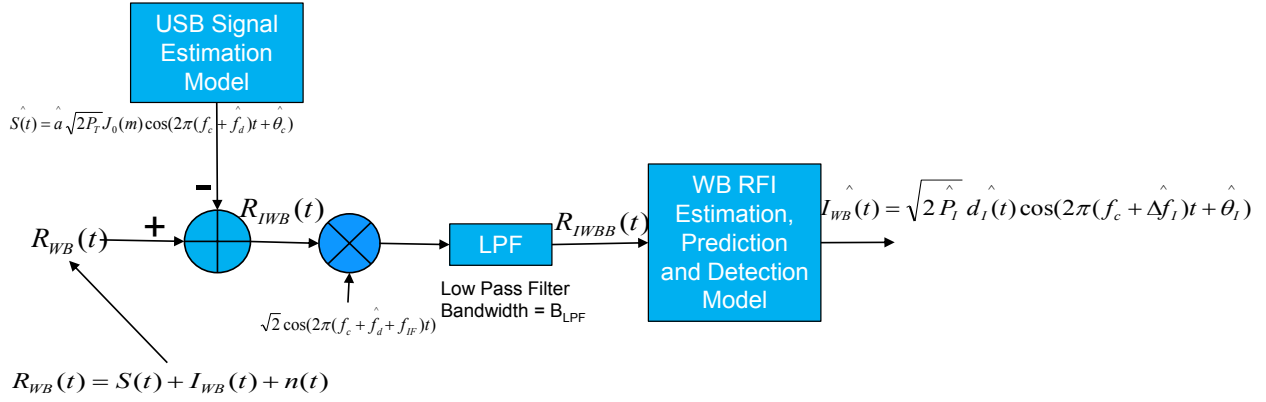


Figure 43. Block Diagram for Extracting the WB RFI Signal from the Received Signal, $R_{WB}(t)$

The received signal at the SATOPS satellite in the presence of WB RFI is given by:

$$R_{WB}(t) = S(t) + I_{WB}(t) + n(t), \quad (207)$$

where $S(t)$ and $n(t)$ are defined as before, and the WB RFI is defined as:

$$I_{WB}(t) = \sqrt{2P_I} d_I(t) \cos(2\pi(f_c + \Delta f_c)t + \theta_I). \quad (208)$$

Again, in Figure 43, $R_{IWB}(t)$ is defined as the estimate of the WB RFI signal at RF frequency in the presence of noise and error signal caused by inaccurate estimate of the USB carrier signal, i.e.,

$$R_{IWB}(t) = I_{WB}(t) + n(t) + \varepsilon(t), \quad (209)$$

where $\varepsilon(t)$ is the error signal caused by inaccurate carrier signal estimator due to RFI, which is defined in (159). Down-convert the received signal $R_{IWB}(t)$ signal to baseband signal $R_{IWBB}(t)$, one obtains:

$$R_{IWBB}(t) = \left| R_{IWB}(t) \cdot 2 \cos(2\pi(f_c + \hat{f}_d)t) \right|_{LPF} = \sqrt{2P_I} d_I(t) \cos(2\pi \Delta f_I t + \theta_I) - \sqrt{2\hat{P}_R} \hat{J}_0(m) [\sin(\theta_e^+) \sin(\theta_e^-)] + N'(t) \quad (210)$$

Similarly, for small tracking errors, one can approximate (209) as follows:

$$R_{IWBB}(t) \approx \sqrt{2P_I} d_I(t) \cos(2\pi \Delta f_I t + \theta_I) - \left(\frac{\sqrt{2\hat{P}_R} \hat{J}_0(m)}{2} \right) \Theta_c(t) + N'(t), \quad (211)$$

where Δf_I , $\theta_c(t)$ and $N'(t)$ are defined as in (161), (162) and (164).

Figure 44 shows an approach for WB RFI estimation, prediction and detection modeling. The proposed approach estimates the WB RFI signal power first and uses its estimate for estimating the WB RFI data rate (hence bandwidth of the WB RFI signal). These estimates are then used for the estimation of WB RFI frequency. The estimated WB RFI frequency along with the other estimates is then used for the CW RFI phase estimation and detection.

Similar to CW RFI case, the 3-dB cutoff bandwidth of the low pass filter (LPF) must set according to the RFI signal bandwidth (or RFI data rate R_I) such that the WB RFI signal can pass through without distortion. Since the 3-dB cutoff bandwidth of the LPF is not known at the beginning, the following steps are proposed to address this issue:

- Step 1: Set the initial LPF's bandwidth $BW_{LPF} = B_{RCX}$, where B_{RCX} is the SATOPS receiver bandwidth. This bandwidth is set based on the 99% power containment bandwidth. As an example, for uncoded bit rate of 2 kbps, the minimum subcarrier frequency recommended by CCSDS is 8 kHz. For this case, the subcarrier frequency-to-bit rate ratio " n " is 4. The CCSDS Recommendation 4.2.2 recommends that the 99% power containment bandwidth for this case is $16R_b$ for modulation index " m " from 0.8 radians to 1.2 radians. For this case, B_{RCX} is set at $16R_b$ and that the CW RFI bandwidth can be assumed to be less than $16R_b$ for uncoded system. For coded system, it is $16R_s$, where R_s is the symbol rate.
- Step 2: Perform the WB RFI signal power and WB RFI data rate estimations to obtain the initial estimate of the WB RFI signal power and bandwidth.
- Step 3: Use the estimate of the WB RFI signal bandwidth to reset LPF's bandwidth BW_{LPF} .
- Step 4: One can repeat Steps 2 and 3 until the estimate of the WB RFI data rate, R_I , settles to a constant data rate and uses that data rate to set the LPF's bandwidth BW_{LPF} .

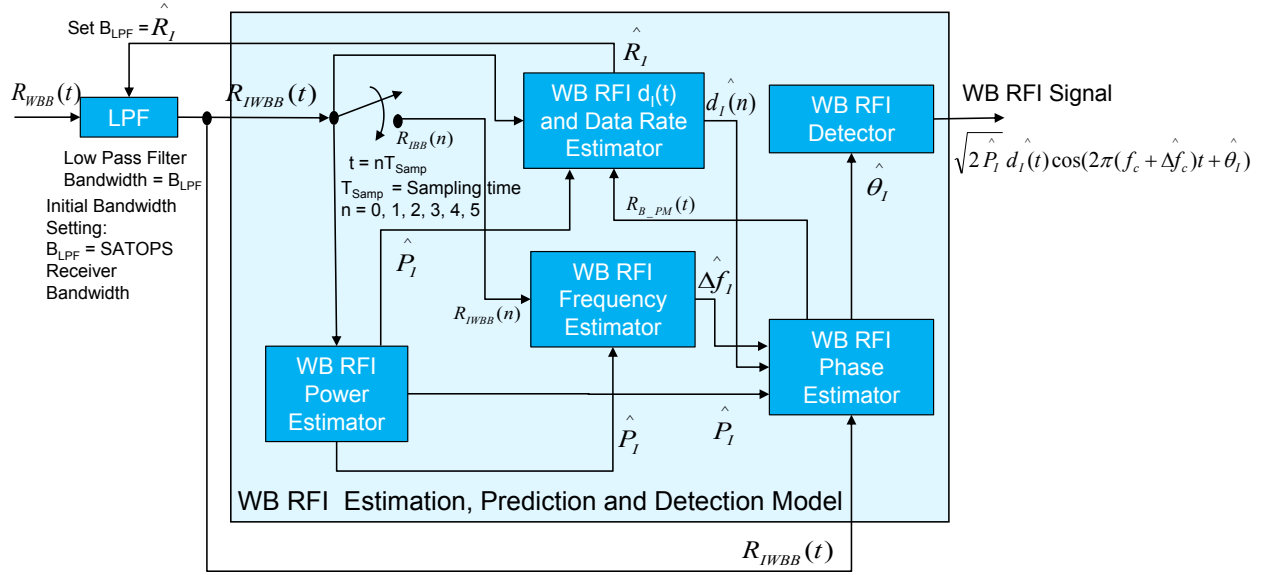


Figure 44. Block Diagram for the WB RFI Estimation, Prediction and Detection Model

3.3.10.2.1 Estimating the WB RFI Signal Power

A combined WB RFI signal power estimator and the WB RFI signal power-to-noise power ratio estimator (INR) is shown in Figure 45. Similar to the CW RFI case, the proposed approach shown in Figure 45 has assumed the signal properties do not change during the observation time. It calculates the average power of all points received since the last reset. When signal properties change during the observation time, the sliding-block discussed in Ref. [8] is used to estimate the WB RFI signal power.

The carrier signal power-to-noise power spectral density ratio, CSNR, interference signal power-to-carrier signal power ratio, ICSR, and the normalized baseband signal $R_{IWBB}(t)$, $R_{IWBBN}(t)$ as, respectively:

$$CSNR_{WB} = \frac{\hat{P}_R J_0^2(m)}{N_0 BW_{LPF}}, \quad (212)$$

where the BW_{LPF} is initially set at B_{RCX} . The optimum setting of BW_{LPF} happens when it approaches the true value of the WB RFI signal bandwidth:

$$ICSR_{WB} = \frac{P_I}{\hat{P}_R J_0^2(m)} \quad (213)$$

$$R_{IWBBN}(t) = \frac{R_{IWBB}(t)}{\sqrt{\hat{P}_R J_0^2(m)}} \quad (214)$$

and

$$R_{IWBBN}(t) \approx \sqrt{ICSR_{WB}} \cdot d_I(t) \cos(2\pi\Delta f_I t + \theta_I) - \left(\frac{1}{2}\right) \cdot \Theta_{c-WB}(t) + \frac{N(t)}{\sqrt{2CSNR_{WB}}}, \quad (215)$$

where $\theta_{c-WB}(t)$ denotes the tracking phase error in the presence of wideband RFI.

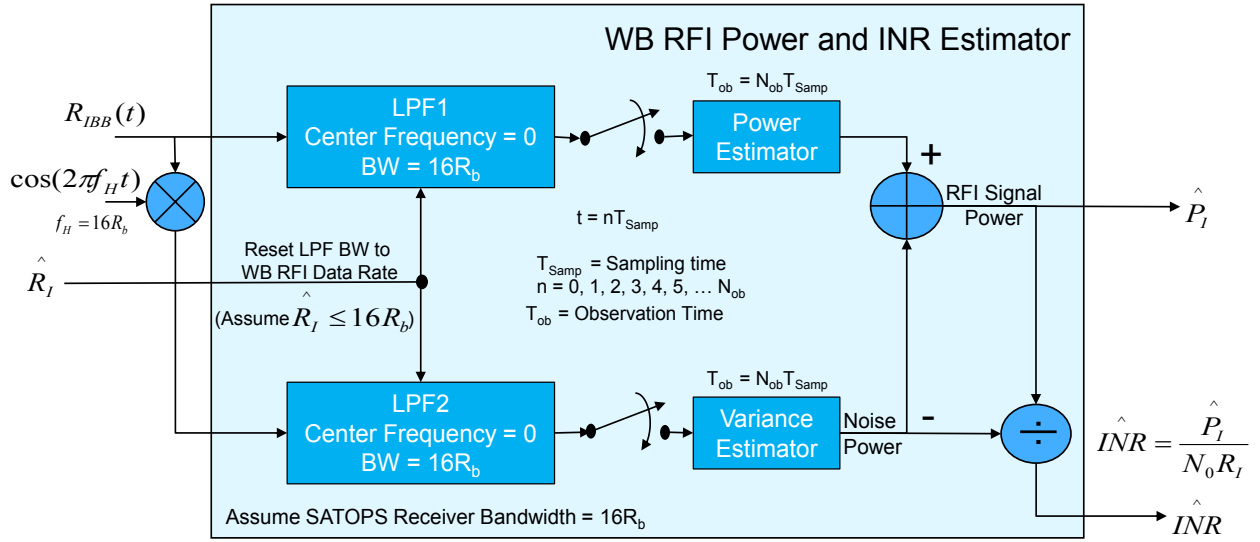


Figure 45. Block Diagram for the WB RFI Power Estimation

Note that in (212), BW_{LPF} is defined as the bandwidth of the LPF that is dependent on the RFI CW signal bandwidth. As mentioned above, the initial LPF bandwidth will be set at the SATOPS receiver bandwidth, B_{RCX} . Note that B_{RCX} is initially set at $16R_b$ for uncoded SATOPS systems. For this case, the CW RFI bandwidth is assumed to be less than $16R_b$.

The unknown power P_I of the WB RFI can be estimated by using power estimator or by taking the expected value of the square of the baseband signal $R_{IWBBN}(t)$, Eqn. (215). From Figure 45, the output of the power estimator is found to be:

$$E\left[(R_{IWBBN}(t))^2\right] \approx E\left[\sqrt{ICSR_{WB}}[\cos(2\pi\Delta f_I t + \theta_I)] - \left(\frac{1}{2}\right)[\Theta_{c-WB}(t)] + \frac{[N(t)]}{\sqrt{2CSNR_{WB}}}\right]^2 \quad (216)$$

and

$$E\left[(R_{IWBBN}(t))^2\right] \approx ICSR_{WB} \cdot E[d_I(t) \cos(2\pi\Delta f_I t + \theta_I)]^2 + \left(\frac{1}{4}\right) \cdot E[\Theta_{c-WB}(t)]^2 + \frac{E[N(t)]^2}{2CSNR} \quad (217)$$

Here,

$$E[d_I(t) \cos(2\pi\Delta f_I t + \theta_I)]^2 = \frac{1}{2} \quad (218)$$

$$E[\Theta_c(t)]^2 = \sigma_{WB-\theta_c}^2 [\sin(\theta_c)]^2 \quad (219)$$

$$E[N(t)]^2 = 1 \quad (220)$$

where $\sigma_{WB-\theta_c}^2$ is calculated using (81). Note that one has assumed that θ_c is a constant phase offset between the desired signal and the PLL VCO's phase. Hence, $\sin(\theta_c)$ is a constant between 0 and 1. Similarly, from Figure 45, the output of the variance estimator is found to be:

$$Var\left[\left(R_{IWBBN}(t) \cdot \cos(2\pi f_H t)\right)^2\right]_{LPF} \approx \left(\frac{1}{4}\right) \cdot \sigma_{WB-\theta_c}^2 [\sin(\theta_c)]^2 + \frac{1}{2CSNR_{WB}} \quad (221)$$

The estimate of the CW RFI power is given by, from Figure 45:

$$\hat{P}_I = \left[2\hat{P}_R J_0^2(m)\right] E\left[(R_{IWBBN}(t))^2\right] - Var\left[\left(R_{IWBBN}(t) \cdot \cos(2\pi f_H t)\right)^2\right]_{LPF} \approx P_I \quad (222)$$

From Figure 45, when the observation time is $N_{ob}T_{Samp}$, the performance of the WB RFI signal power estimator described in (222) can be shown to be:

$$Var\left(\hat{P}_I\right) = \left[\frac{2\hat{P}_R J_0^2(m)}{N_{ob}}\right] \left[\left(\frac{1}{4}\right) \cdot \sigma_{WB-\theta_c}^2 [\sin(\theta_c)]^2 + \frac{1}{2CSNR_{WB}}\right] = \frac{[N_o B_L]}{N_{ob}} \left[1 + \frac{\Delta_{WB}}{2} [\sin(\theta_c)]^2\right] \quad (223)$$

Note that the factor, Δ_{WB} , is calculated using (82).

3.3.10.2.2 Estimating the WB RFI Signal Frequency

Similar to CW RFI case, the WB RFI frequency is unknown and the proposed approach is the identical the CW RFI case with a slight modification. Figure 46 shows a block diagram for the WB RFI signal frequency estimator. The input signal $R_{IWBB}(n)$ to the “CW RFI Frequency Estimator” shown in Figure 38 can be approximated as:

$$R_{IWBBN}(n) \approx \sqrt{2\hat{P}_I} d_I(t) \cos(2\pi f_0 n + \theta_I) + N_{IWBBN}(n), \quad (224)$$

where the frequency, Δf , $d_I(n)$ and phase, θ_I , of the CW RFI are unknown, and

$$N_{IBBN}(t) = \sqrt{2\hat{P}_R} J_0(m) \left[\frac{N(t)}{\sqrt{2CSNR_{WB}}} - \left(\frac{1}{2}\right) \sin(\theta_c) \theta_e(t) \right], \theta_c < \frac{\pi}{2} \quad (225)$$

From Figure 45, the minimum sampling time, T_{Samp} , at Nyquist must be set at:

$$T_{\text{Samp}} = \frac{1}{2(16R_b)} = \frac{1}{32R_b}, \quad (226)$$

where $N_{IWBBN}(t)$ is AWGN with zero-mean and variance is given by:

$$\text{Var}[N_{IWBBN}(t)] = \sigma_{IWBBN}^2 = 2\hat{P}_R J_0^2(m) \left[\frac{1}{4} \sin^2(\theta_c) \sigma_{WB-\theta_e}^2 + \frac{1}{2CSNR_{WB}} \right]; \theta_c < \frac{\pi}{2} \quad (227)$$

The $CSNR_{WB}$ for this case is:

$$CSNR_{WB} = \frac{\hat{P}_R J_0^2(m)}{N_0 BW_{LPF}} \Big|_{BW_{LPF} = B16R_b} = \frac{\hat{P}_R J_0^2(m)}{16N_0 R_b}.$$

Therefore, for WB RFI case, the Interference Signal-to-Noise Power Ratio (ISNR) becomes:

$$ISNR_{WB} = \frac{\hat{P}_I}{\sigma_{IWBBN}^2} = \frac{\hat{P}_I}{16N_{ob}R_b \left[1 + \frac{\Delta_{WB}}{2} \sin^2(\theta_c) \right]} \quad (228)$$

Again, N_{ob} is the number of samples selected during the observation time T_{ob} (see Eqn. (176)).

The factor Δ_{WB} is calculated using (82).


$$R_{WBBN}(n) = \sqrt{2P_l} \cdot \cos(2\pi(2f_0)n + \theta_l) \quad (229)$$
$$2\Delta f_I = \frac{2f_0}{T_{Samp}} = 2.F_{Samp}f_0 \quad (230)$$
$$2f_0 = 2 \frac{(L + \Delta)}{N_{ob}} = 2 \frac{\lambda_0}{N_{ob}}, -\frac{1}{2} \leq \Delta \leq \frac{1}{2}. \quad (231)$$

Similar to CW RFI case, the value of N_{ob} is related to the observation time, T_{Ob} , which is defined as in (176), L is the integer part, Δ is the fractional part of λ_0 , and λ_0 denotes the number of signal cycles contained in the observation window. One can go through the remaining signal processing steps shown in Figure 45 and show that the coarse estimate of the WB RFI frequency is performed by selecting its largest peak, i.e.,

$$f_0^{\hat{coarse_WB}} = \text{Max} \left[\frac{\arg(|X(k)|)}{N_{ob}} \right] = 2 \frac{L}{N_{ob}} \quad (232)$$

Similarly, the fine estimate of the WB RFI frequency is performed by estimating the fractional part Δ_{WB} of λ_0 . It can be shown to have the following form:

$$\hat{\Delta}_{WB} = 2 \cdot \left[\frac{N_{ob}}{2\pi L} \left[\arg(X_1(\hat{f}_0)) - \arg(X_2(\hat{f}_0)) \right] \right] = 2\hat{\Delta} \quad (233)$$

From Figure 45, the fine frequency estimator can be shown to be identical to the case for CW RFI, i.e.,

$$f_0^{\hat{fine_WB}} = \frac{1}{2} \left(2 \frac{L}{N_{ob}} + 2 \frac{\hat{\Delta}}{N_{ob}} \right) = \frac{L + \hat{\Delta}}{N_{ob}} \quad (234)$$

By substituting (234) into (230), one obtains the estimated WB RFI frequency as follow:

$$\hat{f}_i = F_{Samp} f_0^{\hat{fine_WB}} = F_{Samp} \left[\frac{L + \hat{\Delta}}{N_{ob}} \right] \quad (235)$$

The performance of the proposed WB RFI frequency estimator shown in Figure 46 is expected to be worse than the CW RFI frequency estimator due to the increase of the noise power caused by the squaring processing of the signal.

3.3.10.2.3 Estimating the WB RFI Signal Phase and Detecting the WB RFI Signal

This subsection modifies the Maximum Likelihood CW RFI phase estimator and CW RFI signal detector presented in the previous section for CW RFI case. Figure 47 presents the modified approach. From Figure 46, the signal objective of the CW RFI phase estimator is to estimate the phase of the following CW RFI signal by incorporating the power and frequency estimates:

$$R_{WBB}(t) \approx \sqrt{2 \hat{P}_I} \cdot \hat{d}_I(t) d_I(t) \cos(2\pi \hat{\Delta f}_I t + \theta_I) + N_{WB}(t), \quad (236)$$

where the phase, θ_I , of the CW RFI are unknown and the noise term $N_{WB}(t)$ is defined as:

$$N_{WB}(t) = \hat{d}_I(t) N_{IBBN}(t). \quad (237)$$

The noise term expressed in (236) can be characterized as AWGN with zero-mean and variance is defined as in (197). If one assumes that the estimated wideband data $\hat{d}_I(t)$ is synchronized with $d_I(t)$, then one can approximate the product $\hat{d}_I(t)d_I(t)$ as:

$$\hat{d}_I(t) d_I(t) \approx d_I^2(t) = 1. \quad (238)$$

Using the above approximation, one can write (235) as:

$$R_{WBB}(t) \approx \sqrt{2 \hat{P}_I} \cdot \cos(2\pi \hat{\Delta f}_I t + \theta_I) + N_{WB}(t). \quad (239)$$

Using (238), one can show that the signal $R_B(t)$ is identical to CW RFI case. The performance of the proposed WB RFI phase estimator and WB RFI detector shown in Figure 47 is expected to be worse than the CW RFI frequency estimator due to the increase of the noise power caused by the timing synchronization error between the incoming WB RFI and the estimated WB RFI of the signal. When the timing synchronization error is negligible, one can characterize the performance of the phase estimator and signal detector using the CW RFI analytical models presented above.

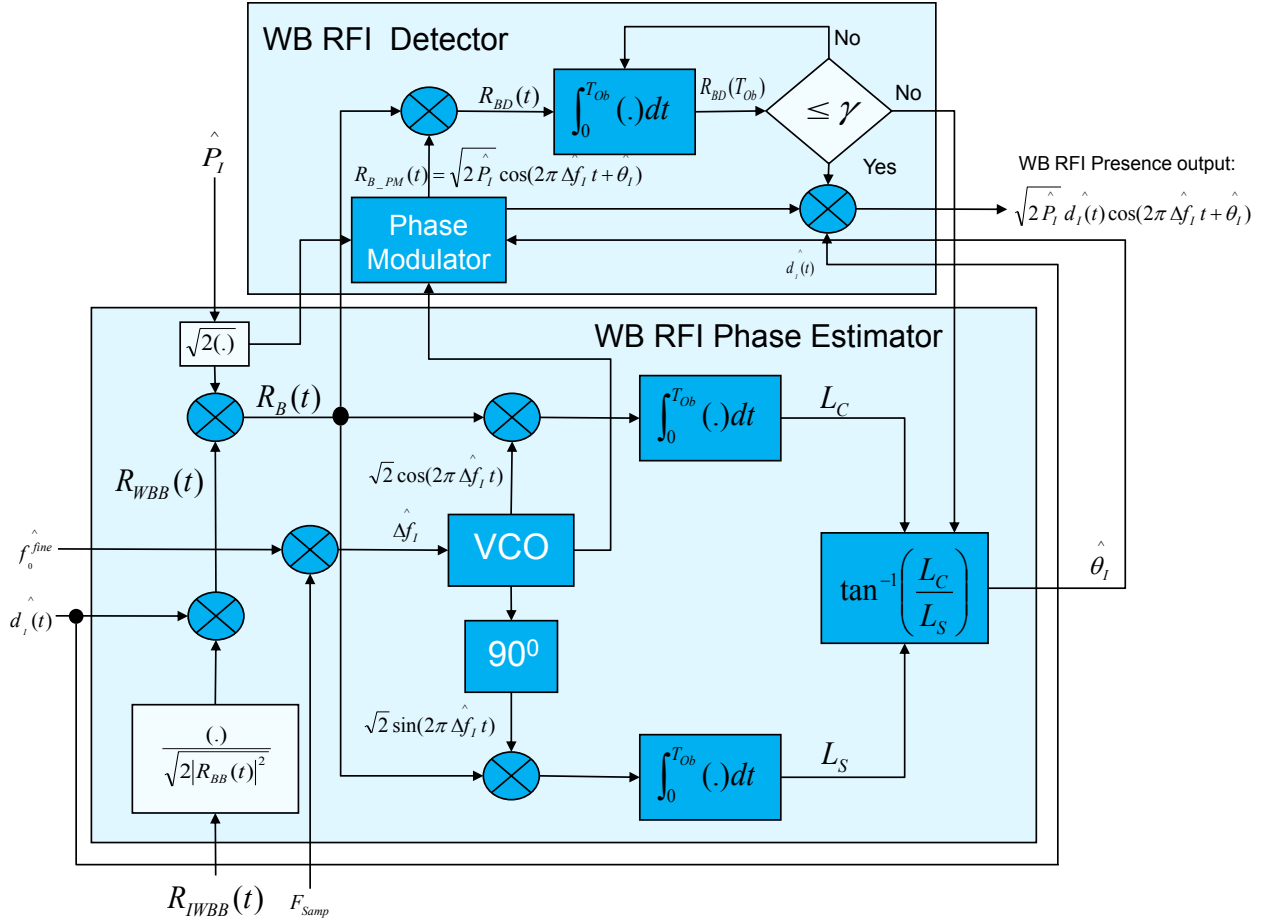


Figure 47. Block Diagram for WB RFI Phase Estimation and RFI Detection

3.3.10.2.4 Estimating the WB RFI $d_i(t)$ and Data Rate

Figure 48 describes the proposed estimator for estimating the WB RFI data stream $d_i(t)$ and data rate R_I . From the figure, the signal $R_{d_i}(t)$ is found to be:

$$R_{d_i}(t) = R_{B_PM}(t) \cdot R_{IWB}(t)$$

$$R_{d_i}(t) = 2\hat{P}_I \hat{d}_I(t) \cos(2\pi \hat{\Delta f}_I t + \hat{\theta}_I) \cos(2\pi \hat{\Delta f}_I t + \hat{\theta}_I) + \text{Noise Term} \quad (240)$$

Equation (240) has assumed that $P_I \approx \hat{P}_I$. If one assumes that $\Delta f_I \approx \hat{\Delta f}_I$ and $\theta_I \approx \hat{\theta}_I$ then (240) becomes:

$$R_{d_i}(t) = \hat{P}_I \hat{d}_I(t) + \hat{P}_I \hat{d}_I(t) \cos(4\pi \hat{\Delta f}_I t + 2\hat{\theta}_I) + \text{Noise Term} \quad (241)$$

From Figure 48, the output of the LPF is found to be:

$$R_{d_I}(t) = \hat{P}_I d_I(t) + \text{Noise Term} \quad (242)$$

The input to the hard-limiter shown in Figure 48 becomes:

$$R_{d_N}(t) = d_I(t) + \frac{\text{Noise Term}}{\hat{P}_I} \quad (243)$$

The noise-term in (143) is characterized by (225). It can be shown that:

$$\text{Var}\left(\frac{\text{Noise Term}}{\hat{P}_I}\right) = \frac{[N_o B_{RCX}]}{\hat{P}_I} \left[1 + \frac{\Delta_{WB}}{2} [\sin(\theta_c)]^2\right] \quad (244)$$

where B_{RCX} is the SATOPS' receiver bandwidth, and it is initially set at $16R_b$ for uncoded SATOPS systems. From Figure 48, the output of the integrator is $R_{d_{IN}}(\hat{T}_I)$ given by, assuming NRZ data format with estimated bit duration, \hat{T}_I , for the WB RFI data stream:

$$R_{d_{IN}}(\hat{T}_I) = \pm 1 + N_I(\hat{T}_I) \quad (245)$$

where one can show that $N_I(\hat{T}_I)$ is an AWGN with zero-mean and variance:

$$\sigma_{N_I}^2 = \frac{[N_o]}{\hat{P}_I \hat{T}_I} \left[1 + \frac{\Delta_{WB}}{2} [\sin(\theta_c)]^2\right] \quad (246)$$

Again, the factor Δ_{WB} is calculated using (82).

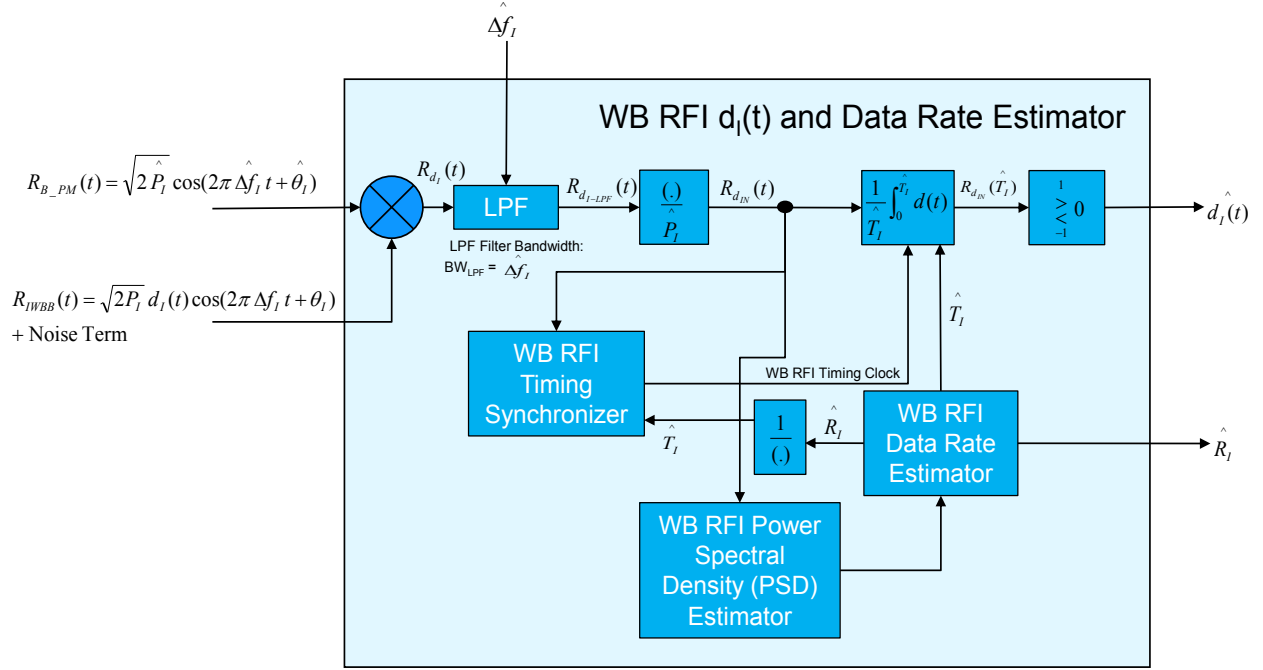


Figure 48. Block Diagram for WB RFI Data Stream and Rata Rate Estimation

From Figure 48, the estimate of the WB RFI data stream $\hat{d}_I(t)$ is derived from Eqn. (245), i.e.,

$$\hat{d}_I(t) = \begin{cases} R_{d_{IN}}(\hat{T}_I) > 0 \rightarrow +1 \\ R_{d_{IN}}(\hat{T}_I) < 0 \rightarrow -1 \end{cases} \quad (247)$$

The error of the estimate is characterized by the bit error rate (BER) of the estimated WB RFI data stream. From (245), $R_{d_{IN}}(\hat{T}_I)$ is a Gaussian random variable with zero-mean and variance is given by (246). One can show that the BER for the estimated WB RFI data stream, BER_{WB_RFI} , has the following form [11]:

$$BER_{WB_RFI} = Q\left(\sqrt{\frac{d_{\min}^2}{4\sigma_{N_I}^2}}\right) \quad (248)$$

where $\sigma_{N_I}^2$ is the variance of the noise $N_I(\hat{T}_I)$, and d_{\min} is the minimum Euclidian distance between the binary bits +1 and -1, which is 2. Substituting $d_{\min} = 2$ into (248), one gets:

$$BER_{WB_RFI} = Q\left(\frac{1}{\sigma_{N_I}}\right), \quad (249)$$

where $Q(x)$ is defined as:

$$Q(x) = \frac{1}{\sqrt{2\pi}} \int_x^\infty e^{-\frac{t^2}{2}} dt = \frac{1}{2} \text{erfc}(x) \quad (250)$$

As shown in Figure 48, the integration time of the integrator is controlled by the WB RFI timing synchronizer, and the timing synchronization error can cause potential degradation in the estimate of the WB RFI data stream. If one assumes that the digital transition tracking loop (DTTL), shown in Figure 49, is used to track the WB RFI timing clock, then the WB RFI timing clock error for a first-order loop (i.e., $F(s)=1$) is found to have the following form [12]:

$$\sigma_\lambda^2 = \frac{\xi \left[1 + \frac{\xi}{4} + \frac{1}{2E_I} \right]}{2\rho_I \left(1 - \frac{\xi}{4} \right)^2}, \quad (251)$$

where

$$\lambda = \frac{\left(\hat{\varepsilon} - \varepsilon \right)}{\hat{T}_I} = \text{Normalize timing error}; -\frac{1}{2} \leq \lambda \leq \frac{1}{2} \quad (252)$$

$$\xi = \text{DTTL window width}; 0 \leq \xi \leq 1 \quad (253)$$

$$E_I = \hat{P}_I \hat{T}_I = \text{WB RFI Bit Energy} \quad (254)$$

$$\rho_I = \frac{\hat{P}_I}{N_0 B_{DTTL}} = \text{DTTL Loop SNR}; B_{DTTL} = \text{DTTL loop bandwidth in Hz} \quad (255)$$

The timing clock jitter is given by:

$$\sigma_\varepsilon = \hat{T}_I \sqrt{\sigma_\lambda^2}, \quad (256)$$

where σ_λ^2 is given by (251) and \hat{T}_I is the estimate of the WB RFI bit duration that is generated by the WB RFI data rate estimator. As shown in Figure 48, the data rate estimator estimates the WB RFI data rate, and hence the WB RFI bit duration \hat{T}_I , from the power spectral density (PSD)

estimator. Following is the discussion on the WB RFI PSD and data rate estimators (and hence WB RFI bit duration \hat{T}_I).

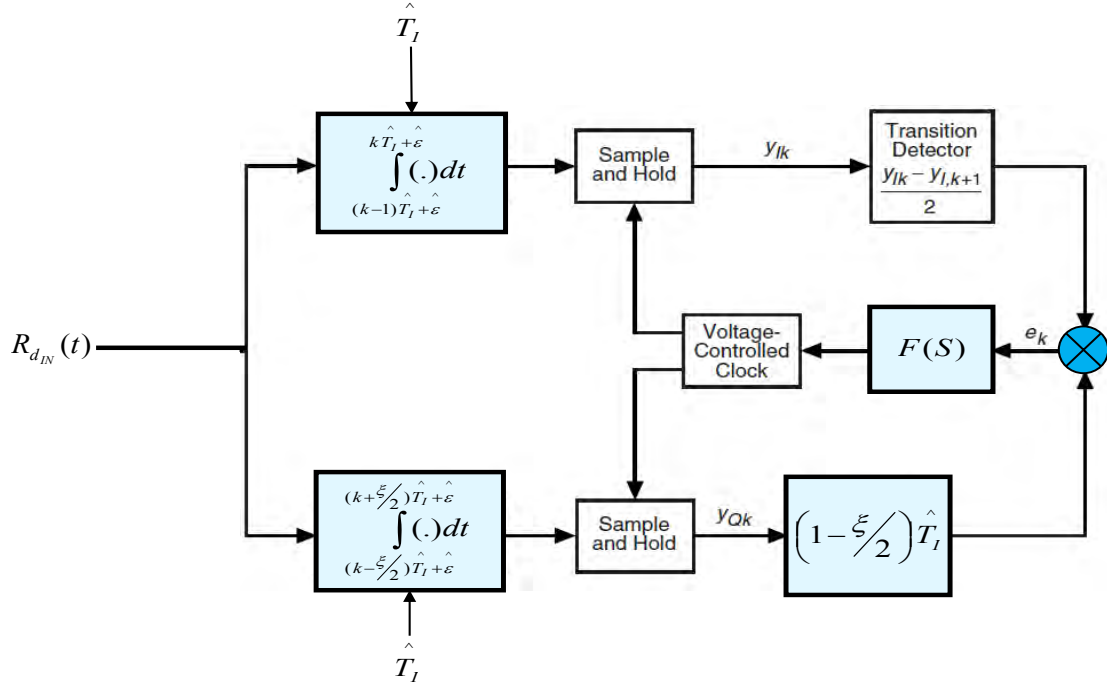


Figure 49. Block Diagram for WB RFI Synchronizer

Figure 50 illustrates the block diagram for the WB RFI PSD and data rate estimators. Similar to previous sections, the signal $R_{d_{IN}}(t)$ is sampled at sampling T_{samp} and the observation time T_{ob} is defined by (176). Auto-correlation function, $r_{d_I d_I}(k)$, is computed using the sampled signal $R_{d_{IN}}(n)$. The input signal to the DFT (Discrete Fourier Transform) block, shown in Figure 50, is calculated using the following relationship:

$$r_{d_I d_I}(k) = \sum_{n=-N_{Ob}/2+1}^{n=N_{Ob}/2} R_{d_{IN}}(n) R_{d_{IN}}(n-k); k=0, \pm 1, \pm 2, \pm 3, \dots, \pm \frac{N_{ob}}{2} \quad (257)$$

The PSD function of the signal, $R_{d_{IN}}(n)$, is computed by taking the DFT of the auto-correlation function given by (257), and it is given by:

$$\begin{aligned}
 PSD(f)|_{f=\frac{k}{T_{ob}}} &= PSD(k) = DFT\{r_{d_I d_I}(k)\} \\
 PSD(k) &= \sum_{n=0}^{N_{ob}-1} r_{d_I d_I}(n) e^{-j\left(\frac{2\pi}{T_{ob}}\right)kn}; k = 0, \pm 1, \pm 2, \dots, \pm \frac{N_{ob}}{2}
 \end{aligned} \tag{258}$$

For NRZ data format, the discrete PSD of a WB RFI is found to be:

$$PSD(k) = \frac{T_I^2}{T_{ob}} \left[\frac{\sin\left(\frac{\pi k T_I}{T_{ob}}\right)}{\left(\frac{\pi k T_I}{T_{ob}}\right)} \right]^2; k = 0, \pm 1, \pm 2, \dots, \pm \frac{N_{ob}}{2} \tag{259}$$

The plot of (259) is shown on the bottom left corner of Figure 50. As shown in Figure 50, the spectral spacing of $PSD(k)$ or frequency resolution is defined in terms of the observation time in sec, T_{ob} , as:

$$\text{Frequency Resolution} = \frac{1}{T_{ob}} \tag{260}$$

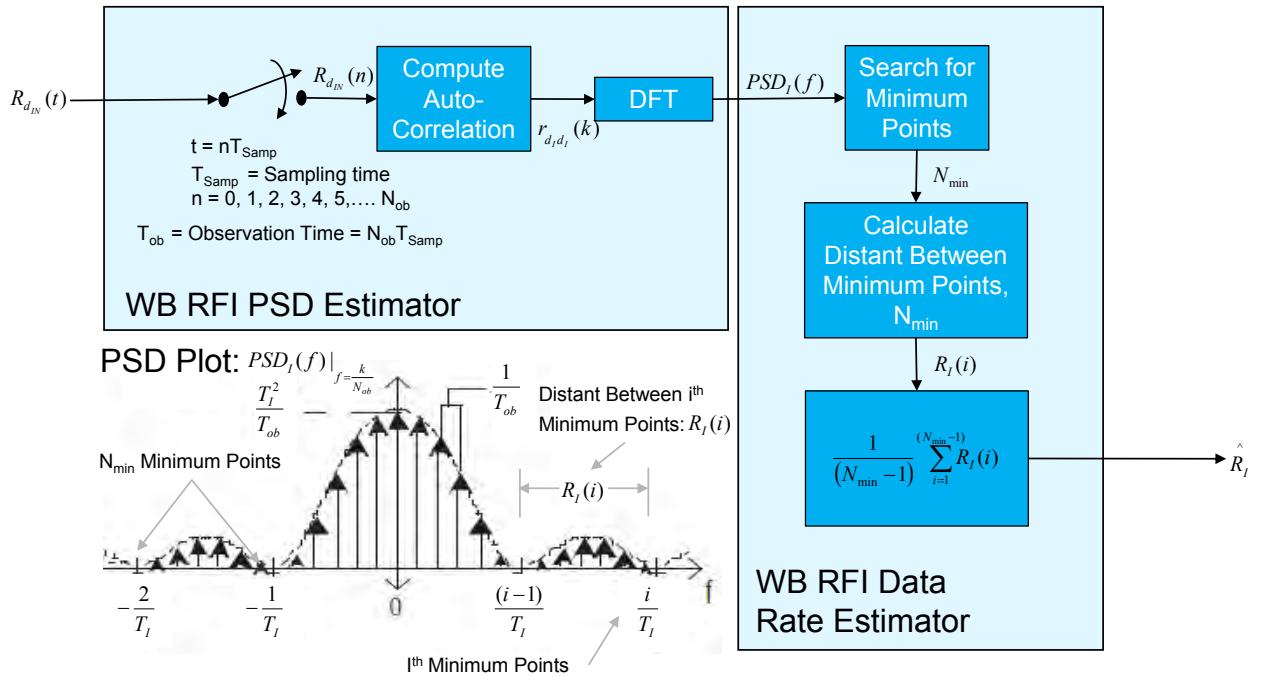


Figure 50. Block Diagram for WB RFI PSD and Data

It is important to note that the sampling time T_{samp} must be fast enough to accurately capture the WB RFI spectrum. For the case of interest, the CW RFI bandwidth is assumed to be less than $16R_b$. Thus, the minimum sampling frequency, F_s , must be at the Nyquist rate, i.e.,

$$F_{\text{Samp}} = 32R_{\text{ob}}. \quad (261)$$

From (261), the required number of samples of $PSD(k)$ or the observation data point, N_{ob} , within the observation time, T_{ob} , is found to be:

$$N_{\text{ob}} = F_{\text{Samp}} T_{\text{ob}} = \frac{T_{\text{ob}}}{T_{\text{Samp}}} = 32R_b T_{\text{ob}}. \quad (262)$$

The WB RFI data rate can be estimated using the nulls (zero-points) of the PSD curve. Since the WB RFI signal is corrupted by the additive noise, sampling noise and quantization noise, the zero-points might be shifted and raised above zero. The proposed algorithm to estimate the WB RFI data rate for this case is illustrated in Figure 50. The algorithm searches for the minimum points, say within the observation time T_{ob} . There would be N_{min} points. If one assumes that the i^{th} zero-point is shifted by ε_i and $(i-1)^{\text{th}}$ zero-point is shifted by ε_{i-1} , then the distance between the i^{th} minimum point and the $(i-1)^{\text{th}}$ minimum point is calculated using the following equation:

$$R_I(i) = \frac{i + \varepsilon_i}{T_i} - \frac{(i-1 + \varepsilon_{i-1})}{T_i}, i = 0, \pm 1, \pm 2, \dots, \frac{N_{\text{ob}}}{2}. \quad (263)$$

Note that in the absence of noise, i.e., $\varepsilon_i = \varepsilon_{i-1} = 0$, and (263) represents a true estimate of the WB RFI data rate. Due to the presence of noise, $\varepsilon_i \neq \varepsilon_{i-1} \neq 0$. The WB RFI data rate can be estimated using the following equation:

$$\hat{R}_I = \frac{1}{(N_{\text{min}} - 1)} \sum_{i=1}^{(N_{\text{min}}-1)} R_I(i). \quad (264)$$

The estimate of WB RFI data bit duration is given by:

$$\hat{T}_I = \frac{1}{\hat{R}_I} = \frac{(N_{\text{min}} - 1)}{\sum_{i=1}^{(N_{\text{min}}-1)} R_I(i)}. \quad (265)$$

As mentioned earlier, the timing synchronization error can cause potential degradation in the estimate of the WB RFI data stream. It is of interest to assess the impacts of the timing error on the estimate of WB RFI data stream. The effect of timing error on the BER performance of the estimate of WB RFI signal can be modeled by observing the following cases:

- Case 1: If two successive (rectangular) bits are identical, an incorrect bit reference will have no effect on the bit error probability; and
- Case 2: If two successive bits differ, the magnitude of the expected correlator output is reduced by a factor: $(1 - 2|\lambda|)$, where λ is the normalized timing error, i.e.,

$$\lambda = \frac{\text{Timing Error}}{\text{Data Bit Duration}} = \frac{\left(\hat{\varepsilon} - \varepsilon\right)}{T_I} = \frac{\tau}{T_I} \quad (266)$$

Based on the above observation, the conditional probability of WB RFI bit error in the presence of timing error can be shown to have the form:

$$P_{WB-\lambda}(E/\lambda) = \frac{1}{2} \mathcal{Q}\left\{\frac{1}{\sigma_{N_I}}\right\} + \frac{1}{2} \mathcal{Q}\left\{\frac{1}{\sigma_{N_I}}[1 - 2|\lambda|]\right\} \quad (267)$$

The Probability Density Function (PDF) of the WB RFI timing error λ in the presence of AWGN for the proposed DTTL synchronizer can be characterized by a Tikhonov distribution, namely,

$$P_{\lambda}(\lambda) = \frac{\exp\{\rho_{WB-RFI} \cos(2\pi\lambda)\}}{2\pi I_0(\rho_{WB-RFI})}, 2|\lambda| \leq 1 \quad (268)$$

where

$$\rho_{WB-RFI} = \frac{1}{\sigma_{\lambda}^2} \quad (269)$$

Here, σ_{λ}^2 is given by (251). The average BER for the estimate of the WB RFI data stream in the presence of imperfect timing recovery becomes:

$$BER_{WB-RFI_Timing} = \int_{-1/2}^{1/2} P_{WB-\lambda}(E/\lambda) P_{\lambda}(\lambda) d\lambda \quad (270)$$

where $P_{WB-\lambda}(E/\lambda)$ and $P_{\lambda}(\lambda)$ are given by (267) and (268), respectively.

3.3.11 USB Link Budget Models for Assessing SATOPS Performance

This section provides a detailed description for the USB link budget model, shown in Figure 9, for estimating the received signal power P_R at the satellite receiver and assessing impacts of RFI on the USB command system performance. The link budget model described

below is for the uplink command SATOPS models. These models consist of two key components:

- Link margin model for carrier tracking, and
- Link margin model for command demodulation.

3.3.11.1 *Link Margin Model for Carrier Tracking*

The link margin model, LM_{carrier} , for the carrier tracking is given by:

$$LM_{\text{carrier}}(\text{dB}) = EIRP(\text{dBm}) + G_r(\text{dBi}) - \left(\frac{C}{N} \right)_{\text{reqd}} (\text{dB}) - \kappa T_s W_c (\text{dBm}) - L_s(\text{dB}) - L_0(\text{dB}) - ML_c(\text{dB}), \quad (271)$$

where EIRP is the transmitted signal power expressed in Effective Isotropic Radiated Power (EIRP) expressed in decibel-milli-Watts (dBm); antenna gain, G_r , is in decibels referenced to isotropic gain (dBi); $(C/N)_{\text{reqd}}$ is the required carrier-to-noise power for a specified tracking loop bandwidth, B_L ; $\kappa T_s W_c$, the maximum thermal noise power, is in decibel-miliwatts (dBm) and is given in terms of the Boltzmann's constant, κ , the system temperature, T_s , and the carrier loop bandwidth, W_c ; $L_s(\text{dB})$ is the space loss in dB; L_0 is the circuit loss plus weather loss plus scintillation loss plus degradation due to RFI plus other losses; and $ML_c(\text{dB})$ is the carrier modulation loss expressed in decibels.

3.3.11.2 *Link Margin Model for Command Demodulation*

The link margin model, LM_{cmd} , for the command demodulation is given by:

$$LM_{\text{cmd}}(\text{dB}) = EIRP(\text{dBm}) + G_r(\text{dBi}) - \left(\frac{E_b}{N_0} \right)_{\text{reqd}} (\text{dB}) - R(\text{dB-bits/s}) - \kappa T_s (\text{dBm/Hz}) - L_s(\text{dB}) - L_0(\text{dB}) - ML_{\text{cmd}}(\text{dB}), \quad (272)$$

where all the parameters are defined as before except $(E_b/N_0)_{\text{reqd}}$ is the required bit SNR for a specified command BER (bit error rate); $ML_{\text{cm}}(\text{dB})$ is the command modulation loss expressed in decibels; and

$$R(\text{dB-bits / sec}) = 10 \log[R_b]. \quad (273)$$

Recall that R_b is the command bit rate in bits/second.

For both link budget models, the space loss, $L_s(\text{dB})$, can be calculated using (110), and the EIRP can be calculated using the following equation:

$$EIRP(\text{dB}) = P_T(\text{dB}) + G_T(\text{dB}) - \text{Feed_Loss}(\text{dB}), \quad (274)$$

where $P_T(\text{dB})$ is the transmitted power in dB, $\text{Feed_Loss}(\text{dB})$ is the antenna feeder loss in dB, and $G_T(\text{dB})$ is the transmitted antenna gain in dB, and it is given by:

$$G_T(\text{dB}) = 10\log(\eta_{TX}) + 20\log\left(\frac{\pi D_{TX} f_c}{c}\right), \quad (275)$$

where η_{TX} is the transmitted antenna efficiency, D_{TX} is the transmitted antenna diameter, and f_c is the transmitted carrier frequency, and c is the speed of light. In the following subsections, the weather loss, scintillation loss, degradation due to RFI, and the carrier modulation loss will be discussed in detail.

3.3.11.3 Weather Loss in USB SATOPS Systems

The weather effect at S-band is almost negligible. Specifically, the attenuation due to dry atmosphere and water vapor is almost 0 dB. In addition, Table 5 shows the rain attenuation computations for 2 GHz and 3 GHz at various values of annual probability. The values in the table were computed assuming that the polarization is circular, elevation angle is 15° , the satellite orbit is 180° W, the city is Tampa, Florida, which has the highest rain precipitation in the U.S., and the Crane rain region is E .

Table 5. Rain Attenuation Loss in dB Calculated for 2GHz and 3 GHz

Annual Percent Of Time	Rain Attenuation (dB) Frequency = 2 GHz	Rain Attenuation (dB) Frequency = 3 GHz
0.1	0.02	0.04
0.8	0.02	0.05
0.6	0.02	0.06
0.5	0.02	0.07
0.4	0.03	0.07

3.3.11.4 Scintillation Effects in USB SATOPS Systems

SATOPS communication links at S-band can be subject to the effects of ionospheric scintillations, which are principally related to the occurrence of *F*-layer irregularities. Scintillations cause both enhancements and fading of signal about the medium level as the signal transits the disturbed ionospheric region. When scintillations occur that exceed the fade margin, performance of the communications link will be degraded. This degradation is most serious for propagation paths that transit in the auroral and equatorial ionospheres. The degree of degradation will depend on how far the signal fades below the margin, the duration of the fade, the type of modulation, and the criteria for acceptability. Table 6 and Table 7 show the signal losses computed at 15° and 10° elevation angles for transmitted frequencies of 2.06 GHz and 1.8 GHz.

Table 6. Signal Losses Due to Scintillation for 15° and 10° Elevation Angle at 2.06 GHz

Annual Percent of Time, <i>p</i> (%)	Signal Loss Due to Ionospheric Scintillations (dB)	
	Elevation Angle $\theta_{\text{Elv}} = 15^\circ$	Elevation Angle $\theta_{\text{Elv}} = 10^\circ$
0.05	22.9	36.5
0.10	19.5	31.6
0.50	11.5	19.5

Table 7. Signal Losses Due to Scintillation for 15° and 10° Elevation Angle at 1.8 GHz

Annual Percent of Time, <i>p</i> (%)	Signal Loss Due to Ionospheric Scintillations (dB)	
	Elevation Angle $\theta_{\text{Elv}} = 15^\circ$	Elevation Angle $\theta_{\text{Elv}} = 10^\circ$
0.05	29.1	45.8
0.10	25.1	39.8
0.50	15.2	25.0

3.3.11.5 Degradation Due to RFI for USB SATOPS Systems

Sections 3.3.5, Section 3.3.6, Section 3.3.7, Section 3.3.8 and Section 3.3.9 above have devoted the modeling of impacts of RFI on the second-order PLL. The carrier SNR (C/N_0) and bit SNR (E_b/N_0) degradations can be calculated using the analytical models presented in those sections.

3.3.11.6 Modulation Losses for USB SATOPS Waveforms

From (1), the modulation losses for USB standard waveforms, which use PCM/PSK/PM commanding signals and PCM/PM-Biphase commanding signals modulated on the carrier, can be shown to have the following forms, respectively:

(1) PCM/PSK/PM USB SATOPS waveform:

$$ML_c = \frac{P_{Carrier}}{P_T} = J_0^2(m) \quad (276)$$

$$ML_{cmd} = \frac{P_{CMD}}{P_T} = 2J_1^2(m) \quad (277)$$

(2) PCM/PM-Biphase USB SATOPS waveform:

$$ML_c = \frac{P_{Carrier}}{P_T} = J_0^2(m) \quad (278)$$

$$ML_{cmd} = \frac{P_{CMD}}{P_T} = 2J_1^2(m) \quad (279)$$

where m is the modulation index, $P_{carrier}$ (or P_c) is the power in the carrier component, and P_{CMD} is the power in the command signal component.

As mentioned at the beginning of this section, the channel gain “ a ” also can be estimated from the link budget model described above. From (162), the channel gain “ a ” can be estimated from the received signal power, P_R , at the satellite transponder, and P_R can be estimated using the following relationship:

$$\hat{P}_R = EIRP(dBm) + G_r(dBi) - \kappa T_s W_c(dBm) - L_s(dB) - L_0(dB), \quad (280)$$

where

$$\begin{aligned}
L_0(dB) &= L_{Atm}(dB) + L_{CaR}(dB) + \Delta_{RFI}(dB) \\
L_{Atm}(dB) &= \text{Loss due to atmospheric (including scintillation) in dB} \\
L_{CaR}(dB) &= \text{Loss due to receiver's cable in dB} \\
\Delta_{RFI}(dB) &= \text{Degradation due to RFI in dB}
\end{aligned} \tag{281}$$

The degradation due to RFI, $\Delta_{RFI}(dB)$, can be calculated using the analytical models presented in Section 3.3.7.

3.3.11.7 Optimum Transmitted Signal Power for USB SATOPS Waveforms

The communications designer can use the framework described in Section 3.2 and the algorithms presented in this section and Section 3.3 to estimate the optimum transmitted signal power, P_{T_Opt} , to maintain a required USB SATOPS Quality-of-Service (QoS) in the presence of both friendly and unfriendly RFI sources. The optimum transmitted power can be calculated using the following relationship:

$$\begin{aligned}
P_{T_Opt}(dB) &= LM_{cmd}(dB) + \left(\frac{E_b}{N_0} \right)_{reqd} + R(dB - \text{bits/s}) + ML_{cmd}(dB) - G_r(dBi) \\
&+ \kappa T_s W_c(dBm) + L_s(dB) + L_0(dB) - G_T(dB) + Feed_Loss(dB)
\end{aligned} \tag{282}$$

where the USB SATOPS QoS is specified through the required bit SNR $(E_b/N_0)_{reqd}$ is through the parameter $L_0(dB)$ described in (281).

4 RESULTS AND DISCUSSION

4.1 RFI Detection and Prediction Model Integration

Our approach was to leverage existing RFI analysis tools that were available in public domain. The team developed a web-based graphical user interface (GUI) for the RFI modeling and prediction tool with the following capabilities:

- Predict USB SATOPS carrier acquisition time consisting of frequency and phase acquisition,
- Predict USB SATOPS carrier tracking performance, and
- Predict USB SATOP command BER performance in the presence of AWGN, continuous wave or wideband RFI, and imperfect carrier tracking caused by AWGN and continuous wave or wideband RFI.

To develop the web-based GUI, the team employed the following programming technologies:

- Java scripting for front-end data handling;
- C-programming to handle the common gateway interface (CGI) interactions (including data entry checking for increased security);
- Develop and implement Matlab codes for evaluating:
 - Carrier acquisition time consisting of frequency and phase acquisition,
 - Carrier tracking performance,
 - Command BER performance in the presence of AWGN, continuous wave or wideband RFI, and imperfect carrier tracking caused by AWGN and continuous wave or wideband RFI.

The web-based GUI for the RFI modeling and prediction tools include features such as double precision, data verification routines to catch user errors on input, and a default feature case that requires minimal user input. Figure 51 shows a screen-shot of the web-based GUI for the RFI modeling and prediction tool.

4.2 IFT SATCOM Tool Integration

This section describes the integration of the RFI prediction and detection models presented in the previous sections into the IFT SATCOMM tool. The IFT tool has been developed based on the open source *Jsattrak* with Java. The integration consists of the following steps:

- Design the menu items to call the display functions of various analysis and simulation results from various CW RFI and WB RFI models, including RFI prediction, SATOPS command carrier acquisition and tracking performances, and SATOPS command BER performance.
- Design a graphical user interface, which is user friendly and functional, including a display of SATOPS system setting, and corresponding analytical and simulation results.

The programming languages required to perform the integration task include Java for front-end data handling in Netbeans.

Command Link Margin Analysis

RFI Geometric Model Information		Victim Satellite Information	
Number of Victim Groundstations	8	Altitude (Km)	2000
Number of Interfering Groundstations	5	Inclination (Degree)	50
Number of Interfering Constellations	1	Equator Crossing (Ascending) Longitude of Orbit at t=0 (Degree)	20
Start Time (Sec)	200000	Victim Receive Thermal Noise Power Density (dBW/Hz)	-110
End Time (Sec)	212000	Minimum Victim Uplink Link Margin w/out Interference (dB)	6
Time Step Increment (Sec)	10		

Victim Satellite Command System Information	
Center Frequency (MHz)	2067.5
Bandwidth (MHz)	4.0
Interval of Integration (MHz)	1000

(submits a run with default parameters using only the time information entered above)

[Tool Description](#)
[Back to Title Page](#)







Figure 51. RFI Modeling and Prediction Tool Integration

Figure 52 shows the overview of IFT SatComm tool integrated with the RFI prediction and detection models. One can see that the menu item “IFT_SatComm” includes the “BER and Tracking error” and “Acquisition Time analysis”, which are the key components in the RFI detection and prediction models described earlier.

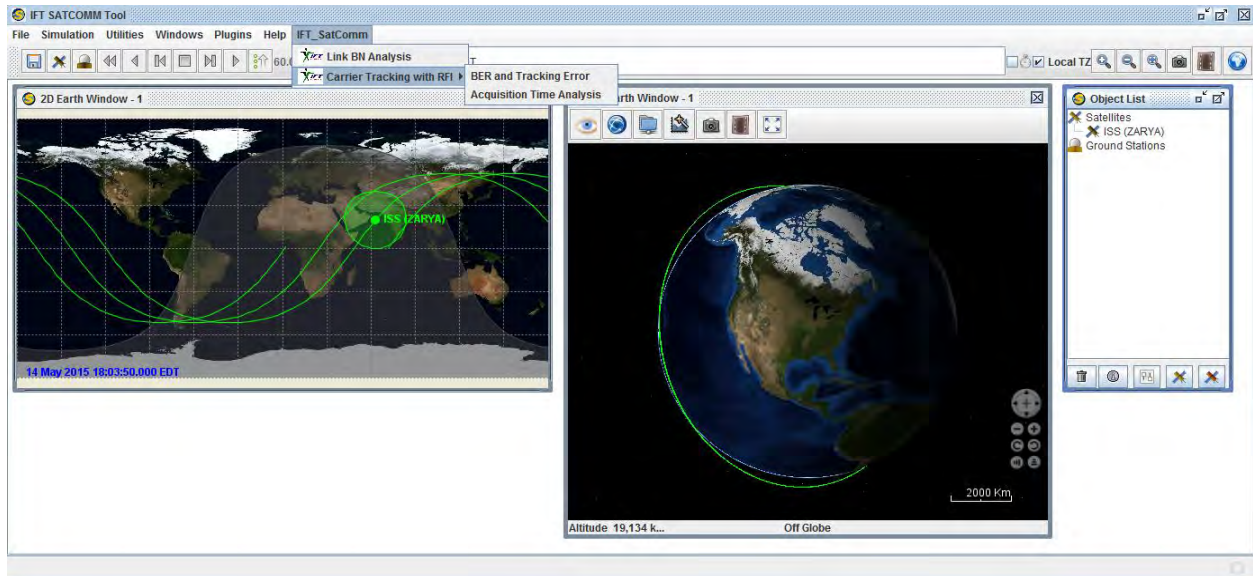


Figure 52. IFT SatComm Tool Integrated With RFI Prediction Results

Figure 53 demonstrates the SATOPS command BER performance in the presence of AWGN, RFI signal and imperfect carrier tracking loop. On the other hand, Figure 54 shows the PLL carrier tracking error performances under no RFI and RFI scenarios. The RFI scenarios include continuous wave RFI and wideband RFI. One can see that in the display window, it has a test area displaying the information of system setting. One will be able to switch between BER results and the carrier PLL tracking error by the buttons.

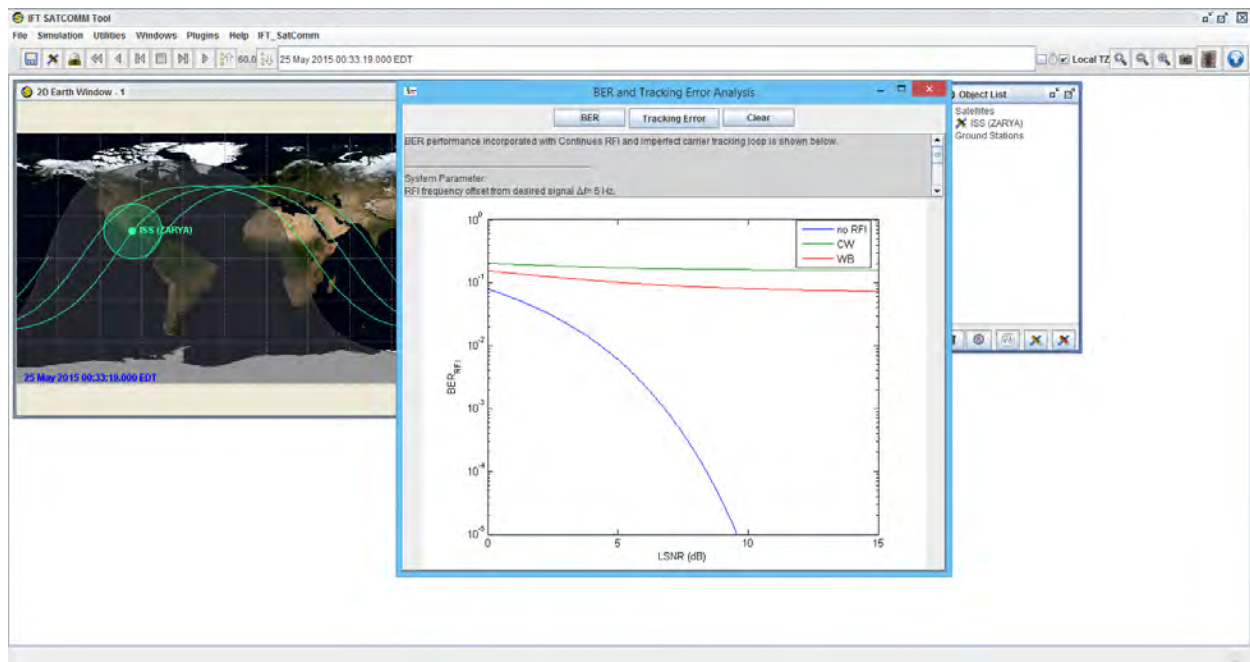


Figure 53. BER Performance With CW RFI or WB RFI and Imperfect Carrier Tracking Loop

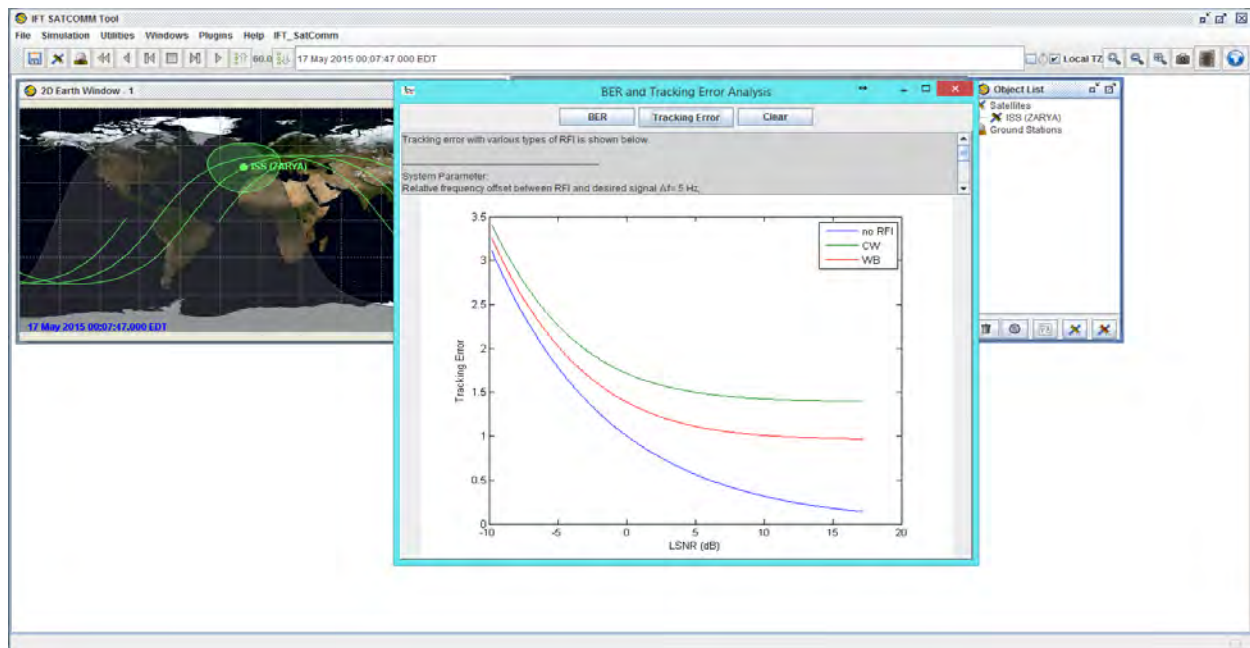


Figure 54. Tracking Error Results Under No RFI and CW RFI or WB RFI Scenario

Figure 55 and Figure 56 show the display for the acquisition time performances under CW RFI and WB RFI, respectively. The display window includes a test area displaying system setting information and the switch buttons. For the acquisition time performance analysis, there are four figures in the windows: (1) relationship between SNR and loop SNR, (2) frequency acquisition time as a function of loop SNR, (3) phase acquisition time as a function of loop SNR, and (4) the total acquisition time of the carrier tracking loop as a function of loop SNR.

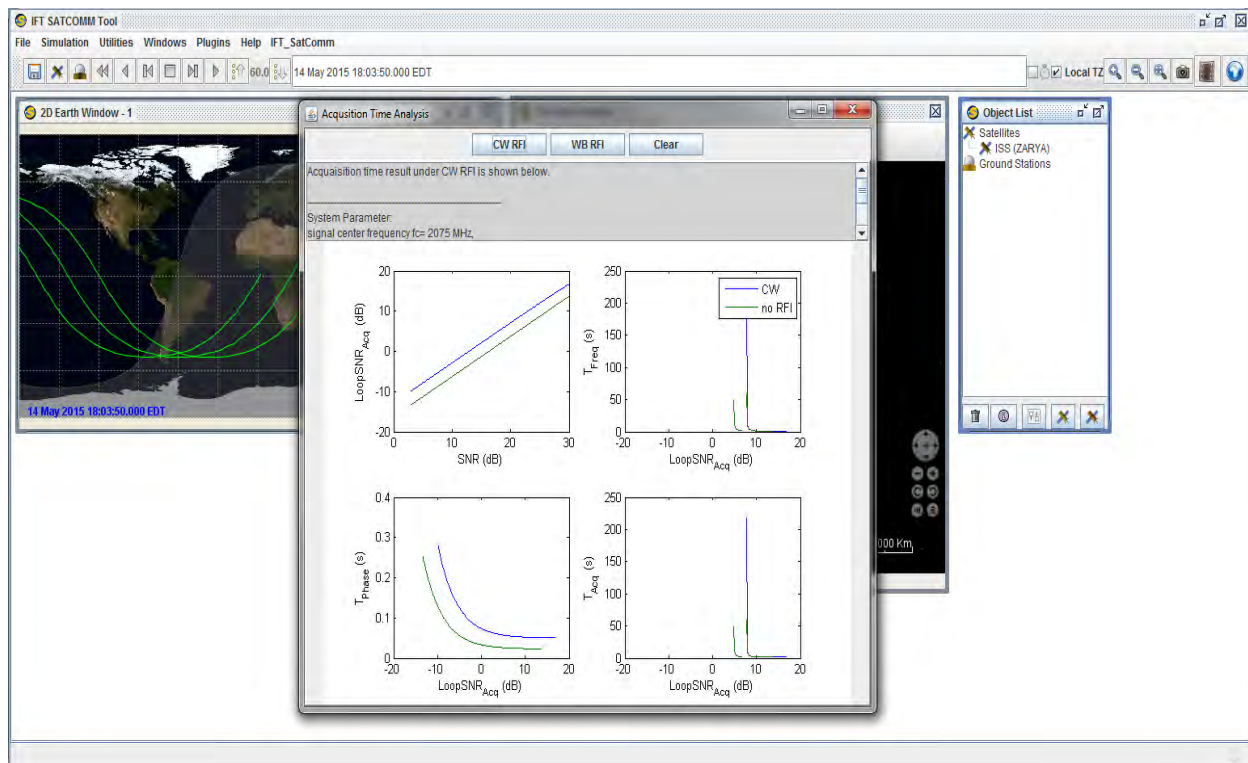


Figure 55. Acquisition Time Result Under CW RFI

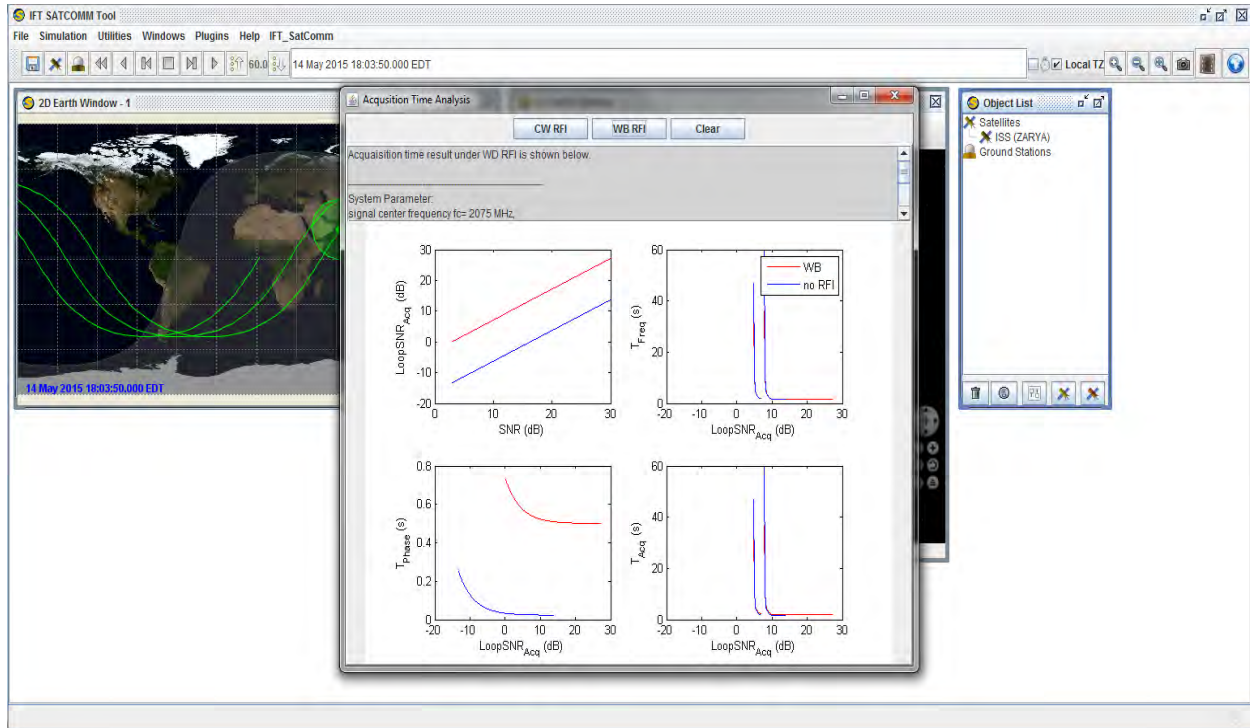


Figure 56. Acquisition Time Result Under WB RFI

4.3 Verification and Validation of RFI Detection and Prediction Tools

The analytical models for RFI detection and prediction, which were derived and discussed in Section 3.3, were implemented in MATLAB for verification and validation (V&V) purpose. These models were tested and verified for various operating scenarios to ensure the accuracy of the performance prediction of a typical USB SATOPS command system. Figure 57- Figure 60 depict the impacts of CW and wideband RFI signals on the second order PLL acquisition performance, respectively. In particular, they compare the carrier acquisition times without RFI and in the presence of RFI as functions of loop SNR for the following cases:

- Signal carrier frequency = $f_c = 2075$ MHz,
- m = command modulation index = 1.1 rad,
- The threshold carrier jitter $\sigma = \pi/2$ rad,
- Command bit rate = $R_b = 2$ kbps, and
- Interference-to-signal power ratio = $ISR = -10$ dB and -40 dB.

Figure 57 shows the assessment of PLL acquisition performance in the presence of CW RFI at $\text{ISR} = -10$ dB. The plots of loop SNR versus received SNR without RFI and with CW RFI are shown on the top left of Figure 57. The plots of carrier frequency acquisition times as functions of loop SNR without RFI and with CW RFI are shown on the top right of Figure 57. The plots of carrier phase acquisition times as functions of loop SNR without RFI and with CW RFI are shown on the bottom left of Figure 57. As expected, the acquisition time increases due to the presence of CW RFI.

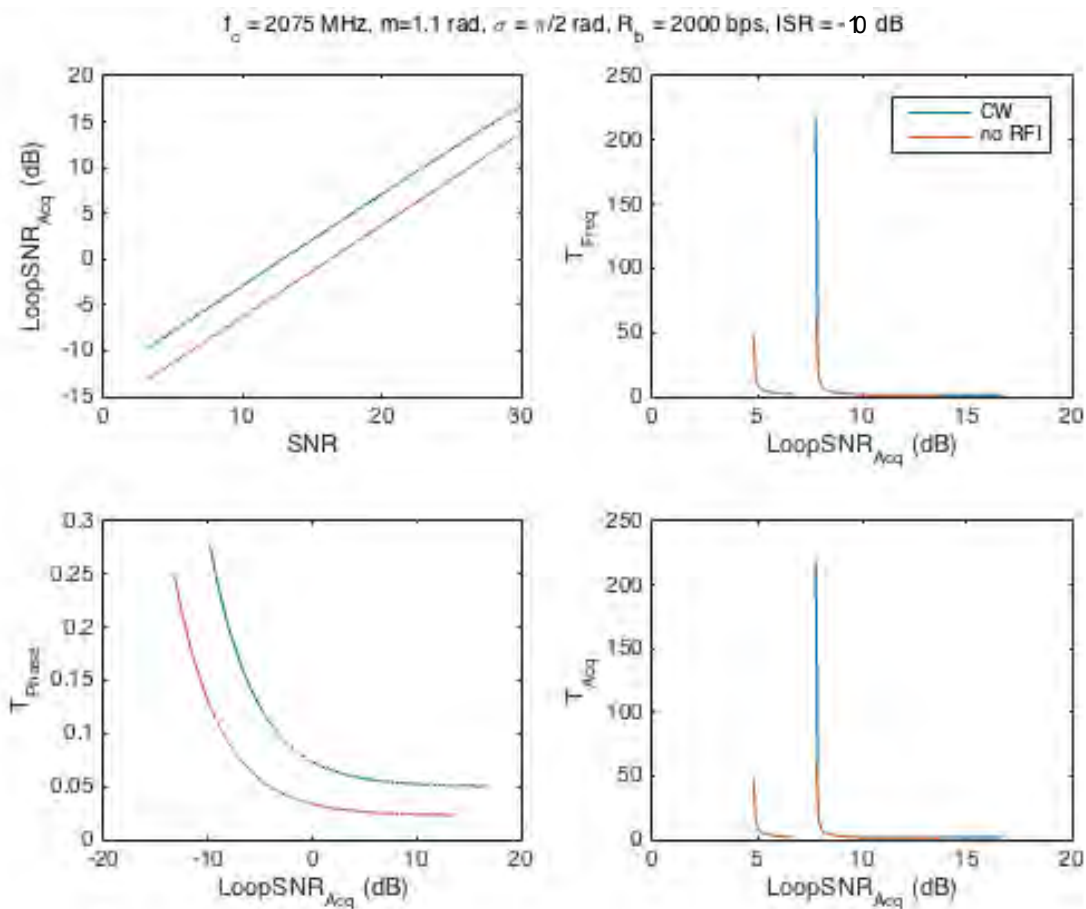


Figure 57. Plots of Total Carrier Acquisition Times Versus Loop SNR Without RFI and With CW RFI

Figure 58 provides results for the assessment of the PLL acquisition performance in the presence of WB RFI at $\text{ISR} = -10$ dB. The plots of loop SNR versus SNR without RFI and with WB RFI are shown on the top left of Figure 58. The plots of carrier frequency acquisition times as functions of loop SNR without RFI and with WB RFI are shown on the top right of Figure 58. The plots of carrier phase acquisition times as functions of loop SNR without RFI and with WB RFI are shown on the bottom left of Figure 58. The results show that the acquisition time increases due to the presence of WB RFI.

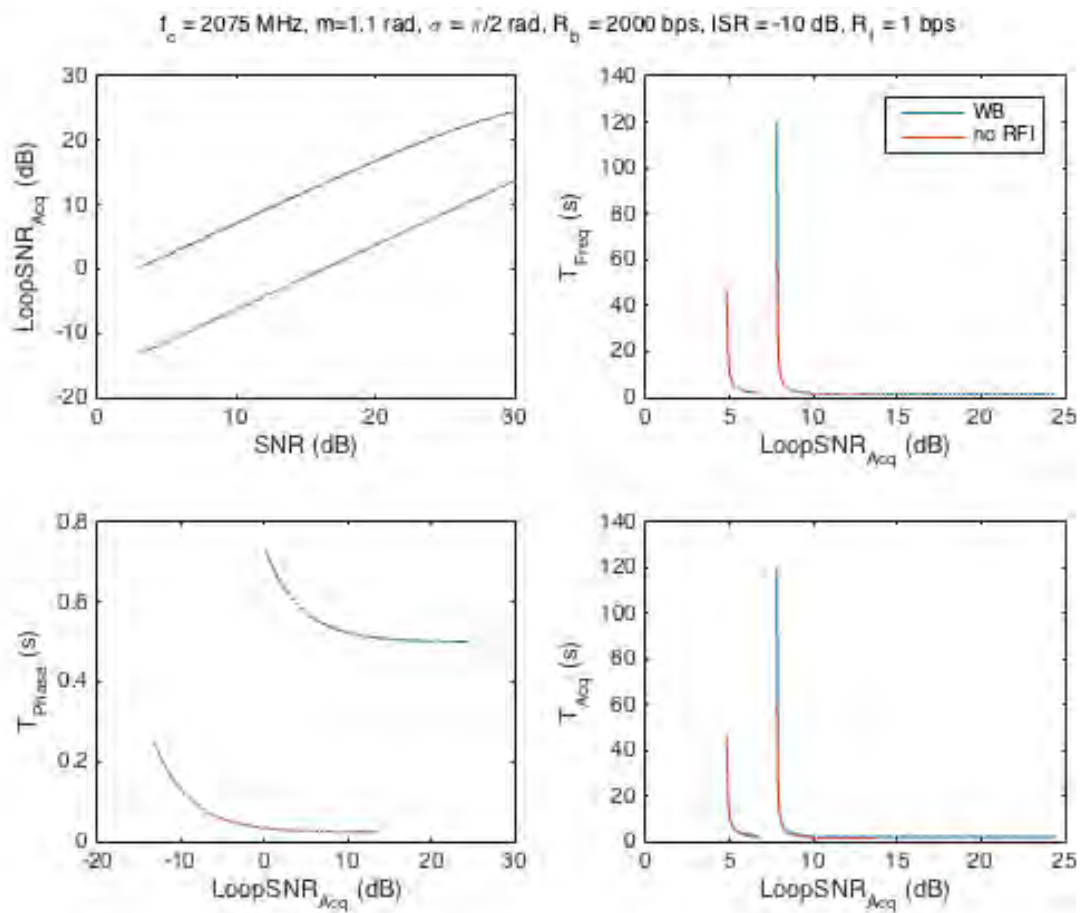


Figure 58. Plots of Total Carrier Acquisition Times as Functions of Loop SNR Without RFI and With WB RFI at $\text{ISR} = -10$ dB

Figure 59 provides the assessment of PLL acquisition performance in the presence of CW RFI at $\text{ISR} = -40$ dB. The plots of loop SNR versus SNR without RFI and with CW RFI are shown on the top left of Figure 59. The plots of carrier frequency acquisition times as functions of loop SNR without RFI and with CW RFI are shown on the top right of Figure 59. The plots of carrier phase acquisition times as functions of loop SNR without RFI and with CW RFI are shown on the bottom left of Figure 59. The results show that the total acquisition time degradation is negligible when the CW RFI interference -to-signal power ratio, ISR , is at -40 dB.

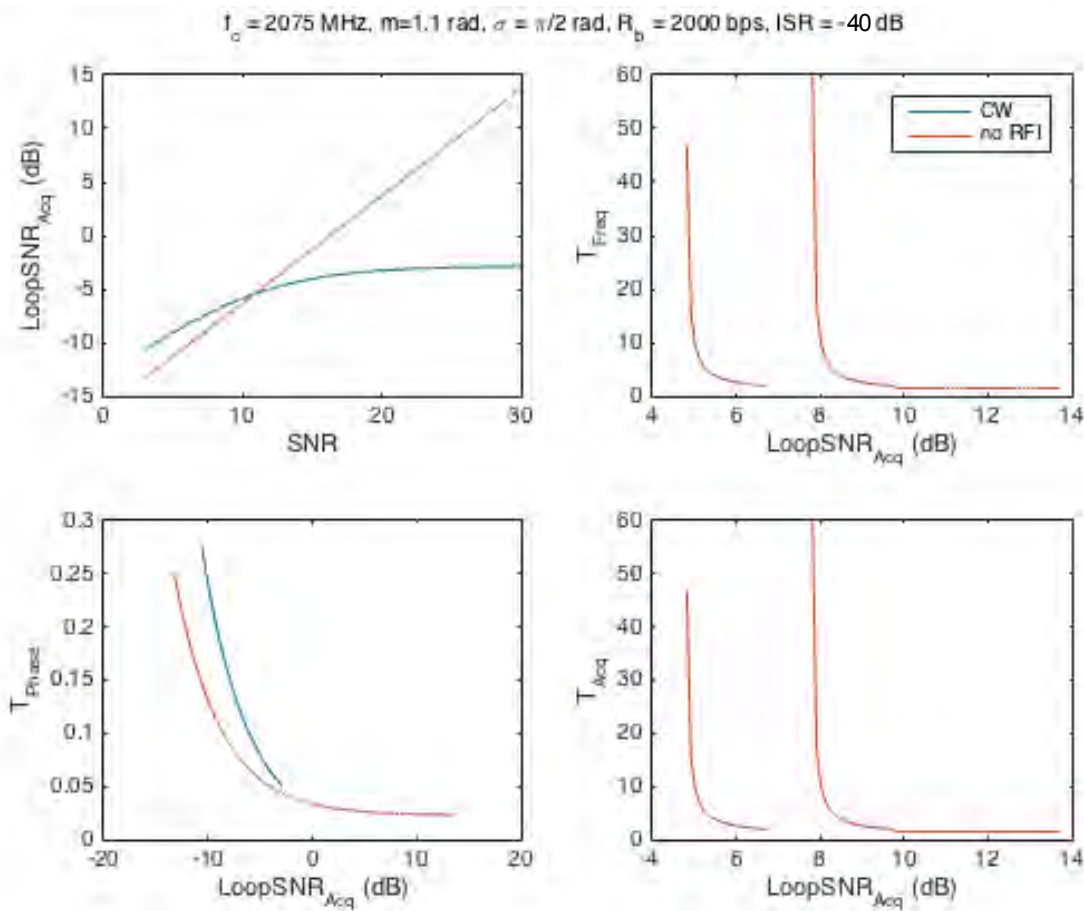


Figure 59. Plots of Total Carrier Acquisition Times as Functions of Loop SNR Without RFI and With CW RFI

Figure 60 presents the assessment of PLL acquisition performance in the presence of WB RFI at $\text{ISR} = -40$ dB. The plots of loop SNR versus SNR without RFI and with WB RFI are shown on the top left of Figure 60. The plots of carrier frequency acquisition times as functions of loop SNR without RFI and with WB RFI are shown on the top right of Figure 60. The plots of carrier phase acquisition times as functions of loop SNR without RFI and with WB RFI are shown on the bottom left of Figure 60. Similarly, for WB RFI, the numerical results show that the total acquisition time degradation is negligible when the ISR is at -40 dB.

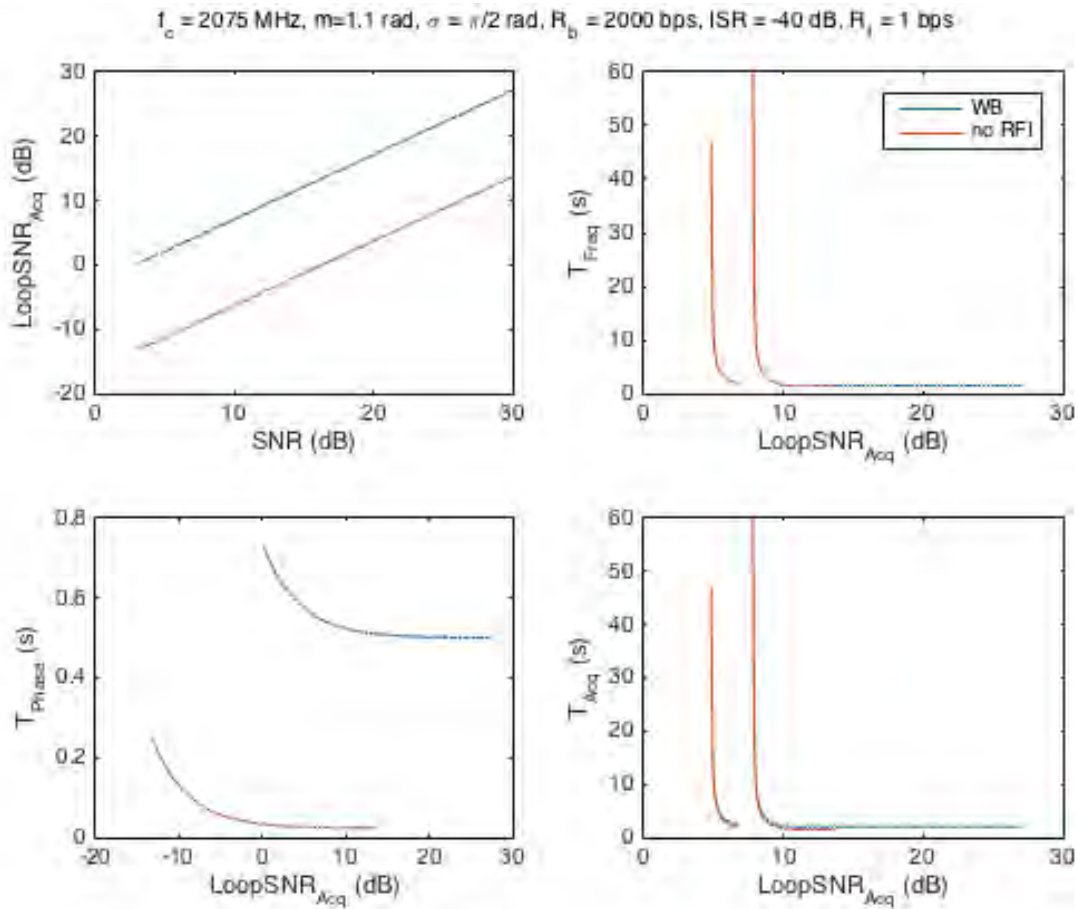


Figure 60. Plots of Total Carrier Acquisition Times as Functions of Loop SNR Without RFI and With WB RFI at $\text{ISR} = -40$ dB

Figure 61 shows plots of PLL tracking jitter in the absence of RFI and with both CW and WB RFI signals as functions of loop SNR with $\Delta f_{\text{RFI}} = 5$ Hz, $m = 1.1$ rads, $\sigma_{\text{margin}} = 2$ deg, $R_b = 2$ kbps, $\text{ISR} = -10\text{dB}$, $R_L = 10$ bps, $B_L = 10$ Hz. The plots show that the tracking performance of the PLL in the presence of CW RFI is worse than WB RFI under the specified operating conditions.

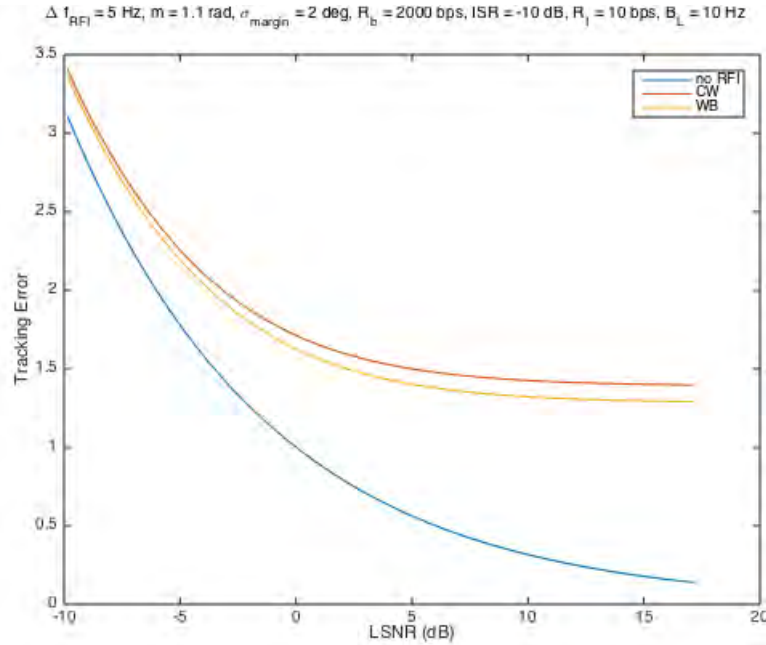


Figure 61. Plots of PLL Tracking Jitter in the Absence of RFI and Presence of CW and WB RFI Signals as Functions of Loop SNR With $\Delta f_{\text{RFI}} = 5$ Hz

Figure 62 shows plots of PLL tracking jitter in the absence of RFI and with both CW and WB RFI signals as functions of loop SNR with $\Delta f_{\text{RFI}} = 10$ Hz, $m = 1.1$ rads, $\sigma_{\text{margin}} = 2$ degs, $R_b = 2$ kbps, $\text{ISR} = -10$ dB, $R_L = 10$ bps, $B_L = 10$ Hz. The plots show that the tracking performance of the PLL in the presence of CW RFI is still worse than WB RFI under the same operating conditions. For this case, the plots show that the carrier tracking performance of the WB RFI is better than the previous case for $\Delta f_{\text{RFI}} = 5$ Hz. This is expected, since the RFI is moving away from the center carrier frequency.

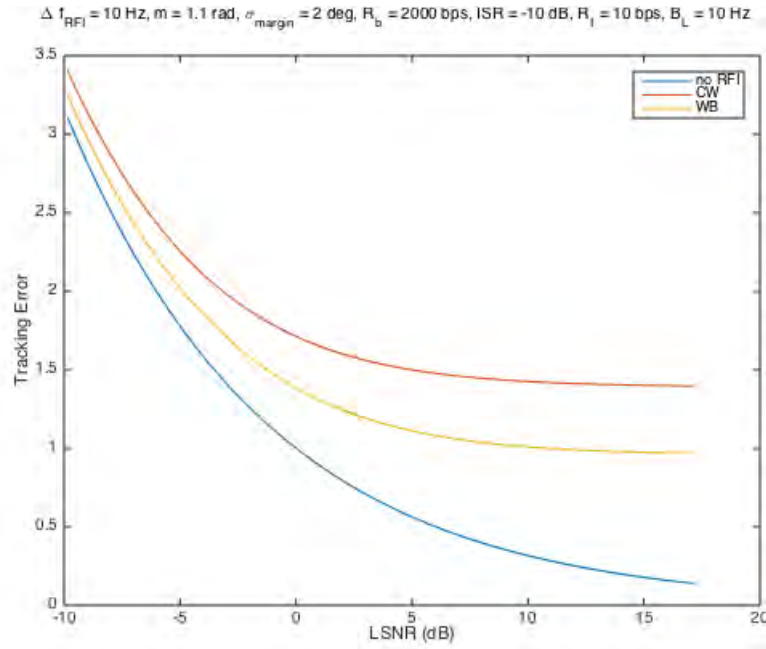


Figure 62. Plots of PLL Tracking Jitter in the Absence of RFI and Presence of CW and WB RFI Signals as Functions of Loop SNR With $\Delta f_{\text{RFI}} = 10$ Hz

Figure 63 and Figure 64 depict the BER performance due to AWGN and RFI signal as functions of loop SNR taking into account carrier synchronization loop. Figure 63 shows plots of BER performance in the absence of RFI and with both CW and WB RFI signals as functions of loop SNR with $\Delta f_{\text{RFI}} = 5$ Hz, $m = 1.1$ rads, $\sigma_{\text{margin}} = 2$ degs, $R_b = 2$ kbps, $\text{ISR} = -10$ dB, $R_l = 10$ bps, $B_L = 10$ Hz. The plots show that the BER performance of the PLL in the presence of CW RFI is worse than WB RFI under the same operating conditions.

Figure 64 shows plots of BER performance in the absence of RFI and with both CW and WB RFI signals as functions of loop SNR with the same operating conditions shown in Figure 63, except with $\Delta f_{\text{RFI}} = 10$ Hz. The plots show that the BER performance of the PLL in the presence of CW RFI is still worse than WB RFI under the same operating conditions. But when compared to this case with Figure 63, the plots show that the BER performance of the WB RFI is better than the previous case for $\Delta f_{\text{RFI}} = 5$ Hz. As pointed out earlier, this is as expected, since the RFI is moving away from the center carrier frequency.

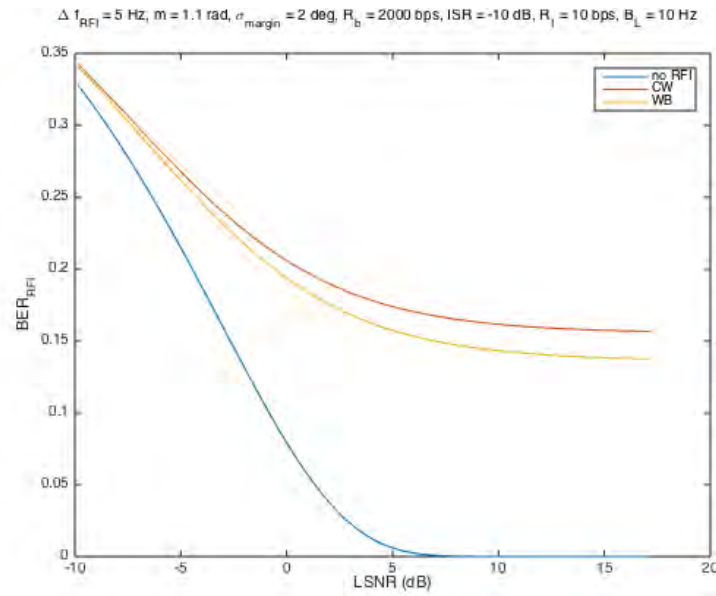


Figure 63. Plots of BER due to RFI for Both CW RFI and WB RFI Signals as Functions of Loop SNR With $f_{\text{RFI}} = 5 \text{ Hz}$

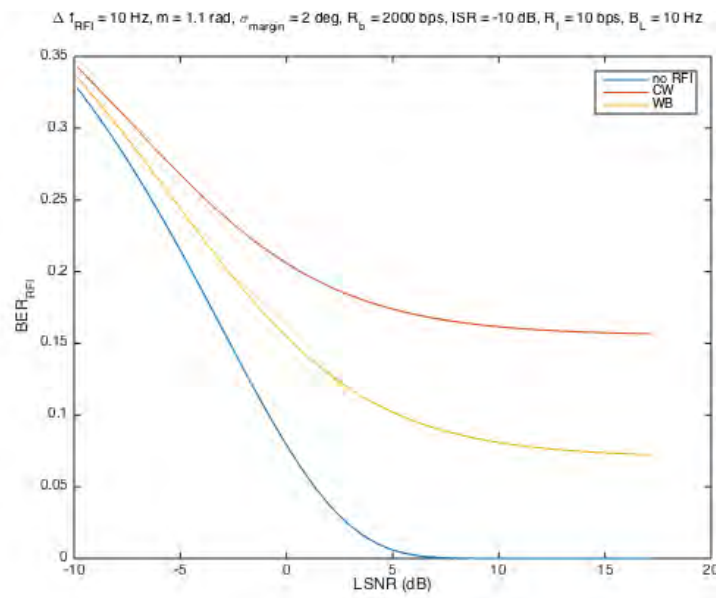


Figure 64. Plots of BER due to RFI for Both CW RFI and WB RFI Signals as Functions of Loop SNR With $f_{\text{RFI}} = 10 \text{ Hz}$

5 CONCLUSIONS

This report presented the work done by the Catholic University of America (CUA) research team, which included North Carolina State University (NCSU) and Intelligent Fusion Technology (IFT) on radio frequency interference (RFI) modeling and prediction. The team accomplished research objectives and completed the six tasks described in our proposal.

The survey results showed that the proposed RFI detection approach using a SATOPS receiver's carrier synchronizer presented in this report is original. The CUA team conducted research on more than 6 RFI tools. We leveraged existing tools for incorporating the RFI detection and prediction. We developed a framework and models to assess the impacts of RFI on SATOPS USB systems.

An innovative framework was developed by the CUA team with an intention to provide a unified approach to address the RFI challenges for USB SATOPS. We described the framework for the RFI tool development, RFI detection and assessment, and RFI prediction. The RFI tool development framework provided detailed description of the tools and models required for detecting, predicting and assessing RFI signals on USB SATOPS command systems. The RFI detection framework described how to incorporate the SATOPS receiver's carrier synchronizer in the detection of CW and WB RFI events. The RFI assessment framework presented a unified approach for evaluating the impacts of CW and WB RFI sources on USB SATOPS command systems. The RFI prediction framework addressed a unified approach for estimating and predicting the characteristics of CW and WB RFI sources. It is worth mentioning that the framework is applicable to both satellite communications and satellite operations.

The team developed analytical and simulation models to evaluate the carrier acquisition and tracking performances of practical USB SATOPS command systems in the presence of CW and WB RFI signals. The impacts of the RFI signals on the carrier synchronizer were used in the detection of the RFI events. We described an approach to accurately predict the RFI interfering time duration using the carrier synchronizer and assessed the impacts of the carrier performance degradation of the synchronizer on the command BER performance. Advanced signal processing algorithms to estimate, predict and characterize the CW and WB RFI signals were described in detail along with analytical models to describe the estimators' performance. The characteristics of the RFI signals estimated and predicted by our team's proposed algorithms included RFI

power, RFI carrier frequency, RFI phase, and RFI bandwidth. In summary, the key RFI analytical and simulation models that were developed under this task included:

- Models to predict USB SATOPS carrier acquisition time in the presence of CW/WB RFI. The acquisition time consists of frequency and phase acquisition.
- Models to predict USB SATOPS carrier tracking performance.
- Model to predict USB SATOP command BER performance in the presence of AWGN, CW/WB RFI, and imperfect carrier tracking caused by AWGN and CW/WB RFI.
- Models to predict RFI duration by monitoring carrier synchronizer.
- Model to detect RFI events by monitoring carrier synchronizer.
- Models to estimate, predict, and characterize CW RFI signals.
- Models to estimate, predict, and characterize WB RFI signals.
- Models to estimate the optimum transmitted USB SATOPS command signal power to maintain a required USB SATOPS quality-of-service (QoS) in the presence of CW and WB RFI signals.

This report described the team's approach to integrate the analytical and simulation models developed in Task #3 into existing RFI tool developed by The Aerospace Corporation. The newly integrated RFI tools have new capabilities including: (i) predict USB SATOPS carrier acquisition time consisting of frequency and phase acquisition, (ii) Predict USB SATOPS carrier tracking performance, (iii) predict USB SATOP command BER performance in the presence of AWGN, CW/WB RFI, and imperfect carrier tracking caused by AWGN and CW/WB RFI, (iv) predict RFI duration by monitoring carrier synchronizer, and (v) detect RFI events by monitoring carrier synchronizer. Currently, only capabilities (i), (ii) and (iii) were verified and validated.

We presented the key software integration results obtained by the team for Task #5. We discussed how the integrated RFI Tool developed in Task #4 were incorporated into existing Intelligent Fusion Technology SATCOM tools to display the RFI detection and prediction results. Screen-shots of how the tools display the RFI results for USB SATOPS command systems were provided. Currently, the team only incorporated three capabilities into the Intelligent Fusion Technology SATCOM tool, including prediction of USB SATOPS carrier acquisition time consisting of frequency and phase acquisition, prediction of USB SATOPS carrier tracking performance, and prediction USB SATOP command BER performance in the

presence of AWGN, CW/WB RFI, and imperfect carrier tracking caused by AWGN and CW/WB RFI.

We provided a summary of the team's approach for Task #6 on the verification and validation of the analytical and simulation models developed in Task #3. The following models were verified and validated by the team: (i) models to predict USB SATOPS carrier acquisition time consisting of frequency and phase acquisition, (ii) models to predict USB SATOPS carrier tracking performance, and (iii) models to predict USB SATOPS command BER performance in the presence of AWGN, CW/WB RFI, and imperfect carrier tracking caused by AWGN and CW/WB RFI.

In conclusion, the team successfully developed a unified framework to address the RFI modeling and prediction challenges by incorporating effects of RFI on the satellite receiver's carrier synchronizers, and sophisticated analytical and simulation models to thoroughly evaluate the impacts of CW and WB RFI signals on the USB SATOPS command system. The team also developed advanced signal processing algorithms to estimate/predict/characterize CW and WB RFI signals. Using RFI modeling and prediction models developed by this research effort, a communications designer can:

- Evaluate effectiveness of the existing USB SATOPS command waveforms employed by civil, commercial and military SATOPS ground stations;
- Predict the impacts of RFI on USB SATOPS command systems;
- Characterize both friendly and unfriendly RFI sources; and
- Estimate the optimum transmitted signal power to maintain a required USB SATOPS Quality-of-Service (QoS) in the presence of both friendly and unfriendly RFI signals.

6 RECOMMENDATIONS

Currently, we have not yet fully incorporated all of the analytical and simulation models that have been developed into the existing RFI tool and IFT SATCOM tool. We have only incorporated the models to estimate and predict:

- (i) USB SATOPS carrier acquisition time in the presence of CW/WB RFI,
- (ii) USB SATOPS carrier tracking performance, and

- (iii) USB SATOPS command BER performance in the presence of AWGN, CW/WB RFI, and imperfect carrier tracking caused by AWGN and CW/WB RFI.

To effectively address the RFI challenges on the USB SATOPS systems, we recommend incorporating the following models into the existing RFI tool and IFT SATCOM tool:

- Models to predict RFI duration by monitoring carrier synchronizer,
- Models to detect RFI events by monitoring carrier synchronizer,
- Models to estimate, predict and characterize CW RFI signal,
- Models to estimate, predict and characterize WB RFI signal, and
- Models to estimate the optimum transmitted USB SATOPS command signal power to maintain a required USB SATOPS Quality-of-Service (QoS) in the presence of CW and WB RFI signals.

The focus of this research project was on the USB SATOPS carrier synchronizer. It is anticipated that the influences of the RFI signals on the command subcarrier synchronizer and symbol timing synchronizer are non-trivial, and they should also be incorporated into the detection of the RFI events and prediction of the RFI signals. We recommend investigating the following research topics:

- USB SATOPS subcarrier and timing acquisition time in the presence of CW/WB RFI,
- USB SATOPS subcarrier and timing tracking performance,
- USB SATOPS command BER performance in the presence of imperfect subcarrier/timing tracking caused by AWGN and CW/WB RFI,
- Prediction of RFI duration by monitoring subcarrier/timing synchronizers, and
- Detection of RFI events by monitoring subcarrier/timing synchronizers.

REFERENCES

1. Shihabi, M. M., Nguyen, Ti. M., Hinedi, S. M., "A Comparison of Telemetry Signals in the Presence and Absence of a Subcarrier," *IEEE Transactions on Electromagnetic Compatibility*, Vol. 36, No. 1, February 1994.
2. Nguyen T. M., Martin, W. L., and Yeh, H. G., "Required Bandwidth, Unwanted Emission and Data Power Efficiency for Residual and Suppressed Carrier Systems-A Comparative Study," *IEEE Transactions on Electromagnetic Compatibility*, Vol. 37, No. 1, February 1995.
3. Nguyen, T. M., "Technique to Select the Modulation Indices for Suppression of Undesired Signals for Simultaneous Range and Data Operations," *IEEE Transactions on Electromagnetic Compatibility*, Vol. 32, No. 1, February 1990.
4. Nguyen, T. M., Yeh, H. G., "Preliminary Design and Implementation of the Baseline Digital Baseband Architecture for Advanced Deep Space Transponders," *TDA Progress Report 42-114*, Published by the Jet Propulsion Laboratory, Pasadena, CA, August 15, 1993.
5. Mengali, U., D'Andrea, A. N., *Synchronization Techniques for Digital Receivers*, 1997, Plenum Press, New York.
6. Satorious, E., Ye, Z., Elly, T., "Carrier Acquisition and Tracking Requirements for Doppler Navigation," *Proceedings of the IEEE*, Vol. 4, pp. 1631, Big Sky, MT, 2003.
7. Viterbi, A. J., *Principles of Coherent Communication*, McGraw-Hill, New York, 1966.
8. Nguyen, T. M., *Mathematical Modeling and Digital Signal Processing Techniques for Modern Digital Communications Systems*, Ph.D. Dissertation, Claremont Graduate University, Claremont, March 1995.
9. Umesh, S., Nelson, D., "Computationally Efficient Estimation of Sinusoidal Frequency at Low SNR," *Proceedings of the 1996 IEEE International Conference on Acoustics Speech and Signal Processing*, Atlanta (GA), Vol. 1, No. 1, 1996.
10. Simon, M. K., Shihabi, M. M., and Moon, T., "Optimum Detection of Tones Transmitted by a Spacecraft," *TDA Progress Report 42-123*, published by Jet Propulsion Laboratory, Pasadena, CA, November 15, 1995.
11. Goldsmith, A., *Wireless Communications*, Published by Stanford University, 2004.
12. Simon, M. K., "Tracking Performance Comparison of the Conventional Data Transition Tracking Loop (DTTL) with the Linear Data Transition Tracking Loop (LDTTL)," *IPN Progress Report 42-162*, published by Jet Propulsion Laboratory, Pasadena, CA, August 15, 1999.

LIST OF SYMBOLS, ABBREVIATIONS, AND ACRONYMS

3G	Third Generation Cellular
4G	Fourth Generation Cellular
8PSK	8-Phase Shift Keying
16QAM	16-Quadrature Amplitude Modulation
a	Channel Gain
ACI	Adjacent Channel Interference
AEHF	Advanced Extremely High Frequency
AFSCN	Air Force Satellite Control Network
AGI	Analytical Graphics, Incorporated
AWGN	Additive White Gaussian Noise
$B_{\text{Acq-DL}}$	Acquisition Mode Loop Bandwidth
B_{DL}	Loop Bandwidth
BER	Bit Error Rate
B_L	Loop Bandwidth
B_{LAcq}	Acquisition Loop Bandwidth
B_{LP}	Loop Bandwidth Perfect Loop Filter
BPF	Band Pass Filter
bps	Bits per Second
B_{RCX}	SATOPS Receiver Bandwidth
c	Speed of Light
CCI	Co-Channel Interference
CCSDS	Consultative Committee for Space Data System
CDMA	Code Division Multiple Access
CDU	Command Detector Unit
CGI	Common Gateway Interface
C/I	Carrier to Interference Ratio
CMM	Carrier Modulation Mode

Approved for public release; distribution is unlimited.

C/N_0	Carrier to Noise Ratio
\cos	Cosine
CSNR	Carrier Signal Power-to-Noise Power Spectral Density Ratio
$CSNR_{WB}$	Wideband Carrier Signal-to-Noise Power Spectral Density Ratio
CUA	Catholic University of America
CW	Continuous Wave
dB	Decibel
dBi	Decibel Relative to Isotropic Gain
dBm	Decibel relative to a milli Watt
DC	Direct Current, 0 Hz
DFT	Discrete Fourier Transform
DTTL	Digital Transition Tracking Loop
E_b	Energy per Bit
EIRP	Effective Isotropically Radiated Power
Eq., Eqn.	Equation
f_c	Carrier Frequency
FCC	Federal Communications Commission
f_d	Doppler Frequency Shift
FOV	Field of View
f_{RFI}	RFI Frequency
F_s	Sampling Frequency
F_{samp}	Sampling Frequency
f_{sc}	Sub-carrier Frequency
f_{Un}	Frequency Uncertainty
GBS	Global Broadcast Service
GCN	Ground Communications Network
GMSK	Gaussian Minimum Shift Keying
G_r	Antenna Gain

GTS	Ground Tracking Station
GUI	Graphical User Interface
Hz	Hertz
ICSR	Interference Signal Power-to-Carrier Signal Power Ratio
IF	Intermediate Frequency
IFT	Intelligent Fusion Technology
INR	Interference Power to Noise Ratio
IPC	Interference Protection Criteria
ISR	Interference to Signal Ratio
ITU	International Telecommunication Union
$I_{WB}(t)$	Wideband Interference Signal
iWPA	Iterative Weighted Phase Averaging
J_0, J_1	Bessel Function, First Kind
JPL	Jet Propulsion Laboratory
kbps	Kilo Bits per Second
kHz	Kilo Hertz
$LM_{carrier}$	Link Margin Model for Carrier
LNA	Low Noise Amplifier
LPF	Low Pass Filter
LSNR	Loop Signal to Noise Ratio
m	Modulation index
MHz	Mega Hertz
ML	Maximum Likelihood
n	Bit Rate Ratio
NASA	National Aeronautics and Space Administration
NCC	Network Control Center
NCSU	North Carolina State University
No	Noise Power

Approved for public release; distribution is unlimited.

N_{ob}	Observation Samples
NRZ	Non Return to Zero
NTIA	National Telecommunications and Information Administration
$P_{\text{c}}, P_{\text{carrier}}$	Power in Carrier
PCM	Pulse Code Modulation
P_{CMD}	Power in Command Signal
PCS	Pulse Coded Signals
PFD	Power Flux Density
P_{I}	Interference Power
PLL	Phased Locked Loop
PM	Phase Modulation
PRF	Pulse Repetition Frequency
PSD	Power Spectral Density
PSK	Phase Shift Keying
P_{t}	Transmit Power
P_{T}	Total Transmitted Power
$Q(a,b)$	Marcum Q-function
QoS	Quality of Service
QPSK	Quadrature Phase Shifted Keying
Rad, rad	radians
R_{b}	Bit rate in bits per second
RF	Radio Frequency
RFI	Radio Frequency Interference
$R_{\text{I}}(t)$	Received Signal
$R_{\text{IBB}}(t)$	Received Signal, Baseband
$R_{\text{IBBN}}(t)$	Received Signal, Baseband
$R_{\text{IWB}}(t)$	Received Wideband Interference Signal
$R_{\text{IWB}}(t)$	Received Baseband Wideband Interference Signal

RL	Radio Loss
ROC	Receiver Operating Characteristic
R_s	Bit rate in bits per second
s	Laplace Variable, $j\omega$
SATCOM	Satellite Communications
SATOPS	Satellite Operations
SCC	Satellite Control Center
SCN	Satellite Control Network
SGLS	Space-to-Ground Link Subsystem
\sin	Sine
SNR	Signal to Noise Ratio
SPW	Signal Processing Workstation
STK	Satellite Tool Kit
T_{acq}	Carrier Frequency Acquisition Time
T_b	Bit Duration in Seconds
TDRSS	Tracking and Data Relay Satellite System
TF	Time Factor
T_{ob}	Observation Time, in Seconds
T_{PAcq}	Carrier Phase Acquisition Time
T_s	Bit Duration in Seconds
T_s	Sample Period
TT&C	Tracking, Telemetry, and Command
USB	Unified S Band
VCO	Voltage Controlled Oscillator
WB	Wideband
W-CDMA	Wideband Code Division Multiple Access
WiFi	Local Area Wireless Computer Networking Technology
WiMAX	Worldwide Interoperability for Microwave Access

Approved for public release; distribution is unlimited.

Δf_c	RFI frequency offset from the desired carrier frequency
$\varepsilon(t)$	Error Signal
η	Antenna Efficiency
κ	Boltzmann's Constant

DISTRIBUTION LIST

DTIC/OCP 8725 John J. Kingman Rd, Suite 0944 Ft Belvoir, VA 22060-6218	1 cy
AFRL/RVIL Kirtland AFB, NM 87117-5776	2 cys
Official Record Copy AFRL/RVSV/Steven A. Lane	1 cy

(This page intentionally left blank)

Approved for public release; distribution is unlimited.